

Development of Smartphone-Based Flow Cytometry for Selective Cell Counting

by

Zhujun Xiao

B.A., Shanghai Jiao Tong University, 2018

A THESIS SUBMITTED IN PARTIAL FULFILLMENT OF
THE REQUIREMENTS FOR THE DEGREE OF

MASTER OF SCIENCE

in

THE FACULTY OF GRADUATE AND POSTDOCTORAL STUDIES

(Chemistry)

THE UNIVERSITY OF BRITISH COLUMBIA

(Vancouver)

June 2021

© Zhujun Xiao, 2021

The following individuals certify that they have read, and recommend to the Faculty of Graduate and Postdoctoral Studies for acceptance, the thesis entitled:

Development of Smartphone-Based Flow Cytometry for Selective Cell Counting

submitted by Zhujun Xiao in partial fulfillment of the requirements for

the degree of Master of Science

in Chemistry

Examining Committee:

W. Russ Algar, Professor, Chemistry, UBC

Supervisor

Dan Bizzotto, Professor, Chemistry, UBC

Supervisory Committee Member

Hongbin Li, Professor, Chemistry, UBC

Supervisory Committee Member

Abstract

Quantum dots (QDs) are promising bioanalytical tools because of their outstanding optical properties, especially their bright and narrow photoluminescence, which offers capacity for multiplexed imaging. Along with flow cytometry, QDs of various colours allow for the detection and enumeration of multiple cell types simultaneously, which is critical for early and efficient screening for diseases, including cancers. Flow cytometry is widely recognized as the “gold-standard” technique for cell classification; however, the cost, size, and sophistication of the method make it unsuitable for use outside of specialized laboratories. A flow cytometry format amenable to point-of-care (POC) application thus has the potential to greatly increase its utility for diagnostics and health care.

This thesis developed a smartphone-based flow cytometer by integrating a laser diode, a PDMS microfluidic chip, and a magnification system into a compact 3D-printed box that interfaced with a smartphone and its camera. Silica-quantum dot ($\text{SiO}_2@QD$) supra-nanoparticles were coated with either dextran or carboxymethyl dextran (CM-Dex), then conjugated to antibodies targeting different cell-surface antigens via tetrameric antibody complexes (TACs) or carbodiimide chemistry. Selective enumeration of multiple cancer cell lines was achieved by immunolabeling with a combination of red, orange, yellow, or green $\text{SiO}_2@QD$ -CM-Dex-antibody conjugates. Smartphone videos of labeled cells under flow were analyzed with an algorithm in MATLAB that extracted PL colour features, classified the cells with a support vector machine model, and counted the cells. Future work with this prototype smartphone-based flow cytometer will aim to improve sensitivity, expand the classification and enumeration capabilities, and test its application with clinical samples.

Lay Summary

This thesis presents the development of a smartphone-based flow cytometer. Nanoparticles made up of many “quantum dots” were used as high-brightness fluorescent materials for specific labeling of various cancer cell lines with different colours. Videos from the smartphone were analyzed to classify and count the types of cancer cells. This compact, low-cost, and portable smartphone-based flow cytometer has prospective applications towards point-of-care diagnostics and early disease detection, particularly in rural, remote, or other areas with limited health care resources and infrastructure.

Preface

The thesis is based on currently unpublished work. Zhujun Xiao co-designed and performed the experiments and completed data analysis. The research program was done under the supervision of Prof. Russ Algar, who co-designed the experiments and helped edit the thesis.

Table of Contents

Abstract.....	iii
Lay Summary	iv
Preface.....	v
Table of Contents	vi
List of Tables	x
List of Figures.....	xi
List of Abbreviations	xviii
Acknowledgements	xxi
Chapter 1: Introduction	1
1.1 Quantum dots	1
1.1.1 Introduction to quantum dots	1
1.1.2 Optical properties.....	3
1.1.3 Surface functionalization and bioconjugation of QDs.....	4
1.1.4 Quantum dots as biological imaging agents	8
1.2 Point-of-care (POC) diagnostics	10
1.2.1 POC diagnostics for biological analysis	10
1.2.2 Synopsis of POC diagnostics	11
1.2.3 Smartphone-based POC diagnostics	13
1.2.4 Smartphone camera technology	15
1.3 Flow cytometry	17
1.3.1 Conventional flow cytometry	17

1.3.2	Microfluidic systems.....	19
1.3.3	Single-cell analysis	20
1.4	Contribution of this thesis.....	22
Chapter 2: Experimental Methods.....		24
2.1	Materials	24
2.2	Microfluidic chip fabrication	24
2.3	Ligand exchange of QDs with glutathione and histidine.....	27
2.4	Preparation of SiO ₂ @QD self-assemblies	28
2.5	Preparation of dextran-coated QDs and SiO ₂ @QD-Dex and SiO ₂ @QD-CM-Dex.....	28
2.6	Immunolabeling of fixed SK-BR3, MDA-MB-231, MCF-7 and A549 cells.....	30
2.6.1	PBS buffer.....	30
2.6.2	Cell culture.....	30
2.6.3	Cell fixation	30
2.6.4	Pre-formation of Tetrameric Antibody Complexes (TACs).....	31
2.6.5	Labeling of fixed SK-BR3 cells with Dex-QDs and SiO ₂ @QD-Dex via TACs.....	31
2.6.6	Preparation of SiO ₂ @(QD-CM-Dex)-antibody conjugates via EDC coupling	32
2.6.7	Fixed SK-BR3, MDA-MB-231, A549, MCF-7 cells labeling with SiO ₂ @(QD-CM-Dex)-antibody conjugates	33
2.7	Fluorescence microscopy.....	33
2.8	Cell counting assays.....	34
2.8.1	Counting non-specifically labeled cells with the smartphone-based flow cytometer	34
2.8.2	Counting SK-BR3 cells labeled with SiO ₂ @(QD625-Dex) without background	
	MDA-MB-231 cells	36

2.8.3	Counting SK-BR3 cells labeled with SiO ₂ @(QD625-Dex) with background MDA-MB-231 cells.....	37
2.9	Selective cell labeling and counting with SiO ₂ @(QD-CM-Dex)-antibody conjugates	37
2.10	Classification of multiple breast cancer cell lines with SiO ₂ @QD-antibody conjugates	40
Chapter 3: Results and Discussion		41
3.1	Design of the smartphone-based flow cytometry setup.....	41
3.2	Validation with non-specifically labeled cells.....	43
3.3	TAC-mediated cell labeling with QDs and SiO ₂ @QD assemblies	45
3.4	Cell counting assays.....	48
3.4.1	Counting SK-BR3 cells immunolabeled with SiO ₂ @(QD625-Dex).....	48
3.4.2	Counting SK-BR3 cells immunolabeled with SiO ₂ @(QD625-Dex) against a constant background of MDA-MB-231 cells	50
3.5	Evaluating multiple colours of SiO ₂ @QD-Dex for immunolabeling.....	52
3.5.1	Characterization of various colours of SiO ₂ @QD.....	52
3.5.2	Immunolabeling of HER2 on SK-BR3 cells.....	53
3.5.3	Immunolabeling and imaging of multiple antigens across SK-BR3, MDA-MB-231, and MCF-7 cells.....	57
3.6	Multiplexed imaging SK-BR3, MDA-MB-231, and MCF-7 cells by EDC/NHS coupling of antibodies to multiple colours of SiO ₂ @QD	59
3.7	Selective cell counting with multiple colors of SiO ₂ @QD assemblies	63
3.8	Classification of different type of breast cancer cell lines with multiple colours of SiO ₂ @QD self-assemblies	72

Chapter 4: Conclusion and Future Work.....	77
4.1 Conclusions.....	77
4.2 Future work.....	78
Bibliography	81
Appendices.....	96
Appendix A MATLAB algorithms.....	97
A.1 Cell counting algorithm	97
A.2 Area-based correction for cell aggregates.....	100
A.3 Selective cell counting and classification with linear support vector machine (SVM) model	102
A.4 MATLAB source code.....	107
Appendix B NTA characterization	121

List of Tables

Table 2.1 Specific filters used for each experiment.....	34
Table 3.1 Mode hydrodynamic diameters (\pm standard deviation) of SiO ₂ @QD and SiO ₂ @(Dex-QD) using scattering mode and fluorescence mode.	52
Table 3.2 Targeted cell lines and corresponding antibodies conjugated to different colours of QDs	61

List of Figures

Figure 1.1 (A) High resolution TEM image of a CdSe/ZnS QDs. (B) Photograph of the size-tunable fluorescence of CdSe QDs under UV illumination. The nanocrystal diameter is indicated above each vial. Figures reprinted with permission from ref. ¹	2
Figure 1.2 (A) Absorption and (B) emission spectra of CdSe/ZnS core/shell QDs of different sizes (from left to right: QD525, QD545, QD565, QD585, QD605, QD625, QD655, QD705, QD800). Figures reprinted with permission from Ref. ¹⁹	4
Figure 1.3 Schematic illustration of some common bioconjugation strategies with QDs. (A) Covalent coupling: (a) QD-antibody coupling between amine groups and thiol groups with SMCC; (b) QD-antibody coupling between carboxy groups and amine groups using EDC; and (c) QD-antibody conjugation between hydrazide-modified QDs and oxidized carbohydrate groups on antibodies. Reproduced with permission from refs. ²⁹ (B) Noncovalent conjugation via (a) streptavidin-biotin interactions, (b) hydrophobic attraction, and (c) electrostatic attractions. Reproduced with permission from refs. ³⁰	7
Figure 1.4 Schematic illustration of (A) a QD conjugated with primary antibody and directly bound to a cell, and (B) a QD conjugated with secondary antibody and bound indirectly to a cell through binding primary antibody. The cell is shown in grey. Reproduced from ref. ⁴⁰	9
Figure 1.5 (A) Illustration of CMOS image sensor with Bayer filter. Reproduced from ref. ¹⁰⁵ (B) Normalized spectral response curves of different smartphone models, derived from monochromator data. Reproduced from ref. ¹¹⁰	16
Figure 1.6 Generic diagram of a multicolour flow cytometer with scatter and fluorescence detection channels. The single cells are illustrated as red spheres. Only one or multiple possible laser sources is shown. Reproduced from ref. ¹¹²	18

Figure 2.1 (A) 3D-rendering of the designed microfluidic chip mold. (B) Dimensions (mm) of the microfluidic chip mold. (C) Image of the final PDMS-on-glass microfluidic chip with inlet and outlet tubing attached..... 26

Figure 3.1 3D-printed smartphone-based flow cytometer (A) Illustration of the device with the laser diode optics. The laser light was collimated with an aspheric lens ($f = 3.3$ mm) and then focused to a line with a cylinder lens ($f = 12.5$ mm). An achromatic doublet ($f = 10$ mm) was used as a magnification lens for cell imaging. (B) Photographs of the device. The sample holder holding the microfluidics chip is attached to the black box lid with four screws. The laser diode can be adjusted with the dial for optimum illumination angle. The waste vial collects the wash solutions and can be replaced with a clean sample vial to re-collect test sample if needed. 42

Figure 3.2 (A) Representative image sequences from a smartphone video (the flow direction is from right to left). (B) Representative smartphone images of different concentrations of fixed SK-BR3 cells non-specifically labeled with QD625-GSH. (C) Comparison of fixed SK-BR3 cell counts from the smartphone setup with a commercial automated cell counter (Slope = 0.99, correlation coefficient $R^2 = 0.9938$, left: linear scale, right: log scale). 44

Figure 3.3 Schematic illustration of TAC-mediated immunolabeling to HER2 antigens on SK-BR3 cells with $\text{SiO}_2@(\text{QD-Dex})$ 46

Figure 3.4 Microscope imaging ($10\times$ magnification) of fixed cells labeled with $\text{SiO}_2@(\text{QD625-Dex})$ (left) and QD625-Dex (right). Scale Bar: 50um. Images were acquired under the same microscope settings. The middle row shows pseudo-coloured PL images with contrast and brightness optimized for $\text{SiO}_2@(\text{QD625-Dex})$. The bottom row shows the same pseudo-coloured PL images but with contrast and brightness optimized for QD625-Dex. 47

Figure 3.5 (A) Representative images taken from smartphone videos of TAC-labeled and DAPI-stained fixed SK-BR3 cells of different concentrations. The flow direction was from right to left. (B) Comparison of calibration curves (left: linear scales, right: log scales) for TAC-labeled (red) and DAPI stained (blue) fixed SK-BR3 cell counts from the smartphone setup, where the expected counts were from a commercial automated cell counter (TAC-labeled SK-BR3 cells: slope 0.86, correlation coefficient $R^2 > 0.99$; DAPI-stained SK-BR3 cells: slope 0.90, correlation coefficient $R^2 > 0.99$). 49

Figure 3.6 (A) Representative images taken from smartphone videos of an increasing number of TAC-labeled and DAPI-stained fixed SK-BR3 cells with background DAPI-stained MDA-MB-231 cells. The flow direction was from right to left. (B) Calibration curve (left: linear scales, right: log scales) of TAC-labeled SK-BR3 cells with a constant number of background MDA-MB-231 cells (represented by the dashed horizontal line). Inset image is the calibration curve of lower cell concentration from 0 to 8 000 cells/mL (slope 0.8749, correlation coefficient $R^2 \sim 0.99$). 51

Figure 3.7 PL characterization of $\text{SiO}_2@\text{QD625}$, $\text{SiO}_2@\text{QD605}$, $\text{SiO}_2@\text{QD575}$, $\text{SiO}_2@\text{QD540}$. Left: Normalized extinction spectra, showing both a scattering component from the SiO_2 nanoparticle and absorption peaks from the QDs. Middle: Normalized PL excitation spectra. Right: Normalized emission spectra. 53

Figure 3.8 (A) Microscope PL images of fixed SK-BR3 cells labeled with $\text{SiO}_2@(\text{QD-Dex})$ of various colors (10× objective, scale bar = 50 μm , in main images; and 60× objective, scale bar = 20 μm , in inset images). All images were acquired under same lamp intensity and exposure time. PL-images are false-colored from the measured monochrome intensity values. SNR and SBR were calculated from the 10× objective images. (B) Smartphone RAW images of fixed SK-BR3 cells

labeled with SiO₂@(QD-Dex) of various colors. All images were acquired under same smartphone settings (ISO200, exposure time 1/30s). The flow direction was from right to left. 54

Figure 3.9 (A) Representative smartphone images of labeled SK-BR3 cells with SiO₂@(QD-CM-Dex)-(anti-HER2) conjugates of various colours (QD650, QD605, QD575, and QD540, the notation of QD λ refers to the wavelength of peak PL emission for the starting QDs). The smartphone images were all captured at same settings (ISO 100, 1/30s, 4000K). (B) Image colour features of SK-BR3 cells labeled with SiO₂@(QD-CM-Dex)-(anti-HER2) conjugates of various QD colours. Each frame of the smartphone videos is a JPEG image in RGB color format. 56

Figure 3.10 (A) Microscope PL images of labeled cells with different antigen expression levels acquired under a 60 \times objective. Control were cells incubated with SiO₂@(QD625-Dex) without TAC. Unlabeled cells are outlined with dashed circles. Scale bar = 20 μ m. All images were acquired under same lamp intensity and exposure time. PL images are false-coloured from the measured monochrome intensity values. (B) Average PL intensity of labeled cells (SK-BR3, MDA-MB-231, MCF-7) with error bars of one standard deviation. A minimum of 20 cells were analyzed from the microscope images acquired under a 60x objective. The dashed line represents the PL intensity level of control sample. 58

Figure 3.11 Schematic illustration of immunolabeling of HER2 antigens on SK-BR3 cells with SiO₂@(QD-CM-Dex)-(anti-HER2) conjugates. The SiO₂@(QD-CM-Dex)-(anti-HER2) conjugates were prepared via EDC/NHS-based covalent coupling first before cell labeling. 59

Figure 3.12 Immunolabeling of fixed SK-BR3 (HER2+) and MCF-7 (HER2-) cells with SiO₂@QD625-antibody bioconjugates via EDC coupling. DIC images are shown in the top row and PL images (10 \times objective, scale bar = 50 μ m, main images and 60 \times objective, scale bar = 20 μ m, inset images) are shown in the bottom row. All images were acquired under the same

microscope settings. SBR and SNR values for the PL images were calculated from the 10× objective images..... 60

Figure 3.13 Microscope images (20× objective, scale bar = 50 μm , main images and 60× objective, scale bar = 20 μm , inset images) with calibration bars of fixed MDA-MB-231, A549, and SK-BR3 cells labeled with $\text{SiO}_2\text{@QD 605-anti-MUC1}$, $\text{SiO}_2\text{@QD650-anti-CD44}$ and $\text{SiO}_2\text{@QD540-anti-HER2}$ respectively..... 61

Figure 3.14 (A) Microscope PL images of fixed MDA-MB-231 cells, A549 cells, and SK-BR3 cells labeled with $\text{SiO}_2\text{@QD-antibody}$ conjugates targeting multiple antigens (HER2, MUC1, CD44) under 60x magnification. Scale bar = 20 μm . (B) Average PL intensity from the labeled cells and background for each antigen. A minimum of 20 cells were imaged with a research-grade microscope under 60x magnification..... 62

Figure 3.15 (A) Classification results of labeled SK-BR3 cells(green) and MDA-MB-231 cells(red) using a Linear SVM(RG) model (left) and labeled SK-BR3 cells(green), MDA-MB-231 cells(red), non-categorized groups(magenta) using Linear SVM(RGN) model (right). (B) Comparison of red objects and green objects ratio detected by MATLAB with Linear SVM(RGN) model and Linear SVM(RG) model with expected red objects to green objects ratio. 65

Figure 3.16 (A) Representative smartphone images of labeled SK-BR3 cells ($\text{SiO}_2\text{@QD540-anti-HER2}$) and labeled MDA-MB-231 cells ($\text{SiO}_2\text{@QD650-anti-MUC1}$). (B) Calibration curve of labeled MDA-MB-231 cells (left, slope 1.00, correlation coefficient $R^2 > 0.99$ using Linear SVM(RG) model; slope 0.96, correlation coefficient $R^2 > 0.99$ using Linear SVM(RGN) model) with a constant number of SK-BR3 cells (right). Error bars: expected cell counts are $\text{mean} \pm$ standard deviation of 5 test samples; SK-BR3 cell counts using the Linear SVM(RG) and Linear SVM(RGN) models are $\text{Mean} \pm$ standard deviation of 3 trials for each test sample. 67

Figure 3.17 (A) Classification results of labeled SK-BR3 cells(green) and MDA-MB-231 cells(red) using Linear SVM(RG) model (left) and labeled SK-BR3 cells(green), MDA-MB-231 cells(red), non-categorized groups(magenta) using Linear SVM(RGN) model (right). (B) Comparison of red objects and green objects ratio detected by MATLAB with Linear SVM(RGN) model and Linear SVM(RG) model. The expected red objects-to-green objects ratio is also shown.

..... 70

Figure 3.18 (A) Representative smartphone images of labeled SK-BR3 cells ($\text{SiO}_2@QD540\text{-anti-HER2}$) and labeled MDA-MB-231 cells ($\text{SiO}_2@QD650\text{-anti-MUC1}$). (B) Calibration curve of labeled MDA-MB-231 cells (left, slope 0.89, correlation coefficient $R^2 > 0.99$ using Linear SVM(RG) model; slope 0.82, correlation coefficient $R^2 > 0.99$ using Linear SVM(RGN) model) with a constant number of SK-BR3 cells (right). Error bars: expected cell counts are mean \pm standard deviation of 5 test samples; SK-BR3 cell counts using the Linear SVM(RG) and Linear SVM(RGN) models are Mean \pm standard deviation of 3 trials for each test sample. 71

Figure 3.19 Microscope DIC and PL images (10x objective, scale bar = 50 μm , main images and 60x objective, scale bar = 20 μm , inset images) with calibration bars of fixed MCF-7, SK-BR3 and MDA-MB-231 cells labeled with $\text{SiO}_2@QD 650\text{-anti-ER}$ conjugate respectively. 73

Figure 3.20 Microscope DIC and PL images (60x objective, scale bar = 20 μm) with calibration bars and corresponding PL spectra of fixed SK-BR3, MDA-MB-231, and MCF-7 cells labeled with a combination of $\text{SiO}_2@QD650\text{-CM-Dex-(anti-ER)}$, $\text{SiO}_2@QD575\text{-CM-Dex-(anti-MUC1)}$, and $\text{SiO}_2@QD540\text{-CM-Dex-(anti-HER2)}$ conjugates. The Excitation filter used for all PL images was 405/20 BP. The Dichroic mirrors used for the green QD, yellow QD, and red QD channel were T425, T510, T590, respectively. The emission filters used for the green QD, yellow QD, and red QD channel were 540/50 BP, 565/30 BP, and 600 LP, respectively..... 74

Figure 3.21 Colour feature of control sample, labeled SK-BR3 cells, MDA-MB-231 cells and MCF-7 cells extracted from the MATLAB algorithm. A Cutoff value of MeanG/MeanB ratio and MeanR/MeanB ratio were set as a mean value $+3 \times SD$ of control sample. 76

Figure 4.1 Representative smartphone image of fixed SK-BR3 cells non-specifically labeled with QD625-GSH (red), QD540-GSH (green), QD472-GSH (blue) and MATLAB result of the corresponding video different concentrations,..... 79

List of Abbreviations

ADU	Analog-to-digital conversion units
APC	Allophycocyanin
API	1-(3-aminopropyl)imidazole
BSA	Bovine serum albumin
CCD	Charge-coupled device
CM-Dex	Carboxymethyl-dextran
CMOS	Complementary metal–oxide–semiconductor
CTC	Circulating tumor cells
DAPI	4',6-diamidino-2-phenylindole
DHLA	Dihydrolipoic acid
DMEM	Dulbecco's Modified Eagle's Medium
EB	Ethidium bromide
EDC	1-ethyl-3-(3-dimethylaminopropyl)carbodiimide
EDTA	Ethylenediaminetetraacetic acid
EGFR	Epidermal growth factor receptor
ER	Estrogen receptor
FACS	Fluorescence-activated cell sorting
FC	Flow cytometry
FITC	Fluorescein isothiocyanate
FPS	Frame per second
FWHW	Full-width-at-half-maximum
GFP	Green fluorescent protein

GSH	L-Glutathione
HCG	Human chorionic gonadotropin
HEPES	4-(2-hydroxyethyl)piperazine-1-ethanesulfonic acid
HER2	Human epidermal growth factor receptor 2
His	L-Histidine
HPA	Hexylphosphonic acid
HPG	Hyperbranched polyglycerol
ID	Inner diameter
IPA	Isopropanol
IPS	Triethoxy-3-(2-imidazolin-1-yl)propylsilane
LAMP	Loop-mediated isothermal amplification
LED	Light-emitting diode
LFA	Lateral flow assay
MAA	Mercaptoacetic acid
μPADs	Microfluidic paper-based analytical devices
MWCO	Molecular weight cut-off
NHS	N-hydroxysuccinimide
NIR	Near-infrared
OD	Outside diameter
PBS	Phosphate-buffered saline
PCR	Polymerase chain reaction
PDMS	Polydimethylsiloxane
PE	Phycoerythrin

PFOTS	Trichloro(1H,1H,2H,2H-perfluorooctyl)silane
PL	Photoluminescence
PLA	Polylactic acid
PMMA	Polymethyl methacrylate
POC	Point-of-care
PR	Progesterone receptor
QD	Quantum dot
QY	Quantum yield
RAA	Recombinase-aided amplification
RCF	Relative centrifugal force
SBR	Signal-to-background ratio
SMCC	Succinimidyl 4-(N-maleimidomethyl)cyclohexane-1-carboxylate
SNR	Signal-to-noise ratio
SVM	Support vector machine
TMAH	Tetramethyl ammonium hydroxide
TOPO	Trioctylphosphine oxide

Acknowledgements

First of all, I would like to show my sincere gratitude to my supervisor, Prof. Russ Algar, for always encouraging me throughout my project with patience and inspiring me with many brilliant ideas when I meet challenges. I have learnt so much from you in the past few years, not only knowledge on nanomaterials, but also the attitude towards research, the communication and presentation skills to efficiently convey science. I feel I am really fortunate to be a part in the Algar group.

I would extend my gratitude to all the supporting staff in Chemistry department, to Pritesh Padhiar for all the guidance and advices on 3D printing, Elena Polishchuk and Jessie Chen for help in Bioservices, Francis Manalastas from Electronic Engineering shop and Ben Herring from the Shared Instrument Facility.

I would also like to thank the NSERC CREATE Training Program and the University of British Columbia for grant supports and awards, Prof. Michael Wolf and Prof. Mark MacLachlan for the two great courses on nanomaterials and all the encouragement you gave to me in my first year.

Many of the thanks and love will be given to every member in the Algar family, who never hesitate to help me with all the new techniques, discuss research ideas with me during break and give me suggestions on many aspects outside the lab. Special thanks to Dr. Michael Tran, who gave me lots of help when I started my project and answered many of my questions. I am also really grateful to Hsin-Yun Tsai, Rupsa Gupta, Ghinwa Darwish and Rehan Higgins for all the mental support in the past few years. There are many difficult times when I started my new life in UBC away from my home country, but you can always let me feel I'm not alone and make me smile again.

I would also like to acknowledge Guizhao Luo, who has been my support through my undergraduate and master studies. Thank you for learning MATLAB with me and helping me out when I struggled with coding. Thank you for always being there to let me feel I can tackle every challenge in my life. Everything you did means a lot to me and I deeply appreciate it.

Finally, words cannot describe my gratitude to my parents, who believe in every decision I made and give me their unwavering supports. My mom, who is the greatest woman in the world, made every effort to offer me opportunities to pursue my dream and give me freedom to create my own life. I cannot imagine all the difficulties you have ever met but I wish I can be as strong as you in my future journey.

Chapter 1: Introduction

Over the past two decades, quantum dots (QDs) have become promising bioanalytical tools because of their unique photophysical properties. As fluorescent labels in bioanalysis, QDs can enhance the readout of biological assays, particularly in the context of point-of-care (POC) diagnostics, which may lack the sensitive imaging sensors commonly found in sophisticated laboratory-based research instruments. This chapter gives a brief introduction on the use of QDs as fluorescent labels, including their structure, optical properties, surface chemistry, and bioconjugation strategies. An overview of flow cytometry and POC diagnostics is also provided, as this thesis will address the convergence of QDs with these concepts.

1.1 Quantum dots

1.1.1 Introduction to quantum dots

QDs are semiconductor nanocrystals with particle diameters ranging from 2-10 nm. These tiny nanocrystals contain hundreds to thousands of atoms depending on their size, with atomic arrangements similar to those of bulk semiconductor materials (see **Figure 1.1 (A)**). When the size of these semiconductor materials is shrunk down to the nanometer scale, they show extraordinary physical and optical properties due to the quantum confinement. These properties are not seen in bulk materials. Specifically, when a semiconductor absorbs light, an electron will be excited to the conduction band, leaving behind a hole in the valance band. When the distance between the electron and hole is forced smaller than the exciton Bohr radius (*i.e.* preferred separation distance between the electron and hole) as the nanocrystal size decreases, the exciton will be squeezed and the quantum confinement effect will occur. Energy states shift to higher levels and the material becomes brightly photoluminescent. The wavelength and colour of emission can be tuned by the QD size based on different extents of quantum confinement (see **Figure 1.1 (B)**)

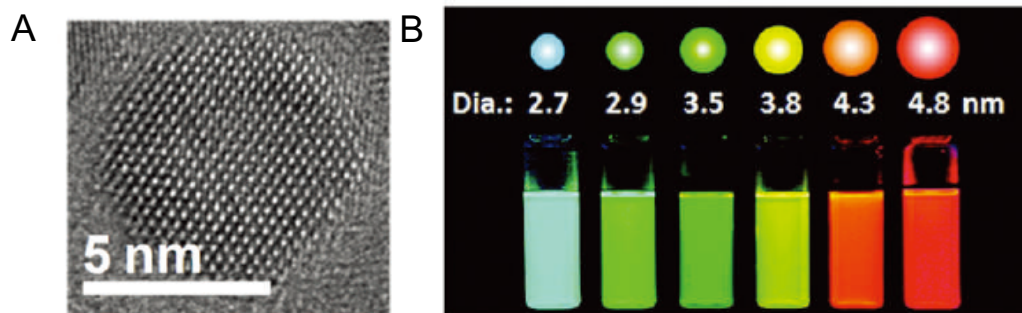


Figure 1.1 (A) High resolution TEM image of a CdSe/ZnS QDs. (B) Photograph of the size-tunable fluorescence of CdSe QDs under UV illumination. The nanocrystal diameter is indicated above each vial. Figures reprinted with permission from ref.¹

The most commonly used semiconductor materials for QDs are cadmium chalcogenides (CdX), where, for example, CdSe nanocrystals have bright emission across the visible region of the spectrum.¹ Other materials include lead chalcogenide QDs, which have larger exciton Bohr radii than CdX QDs and emission that shifts into the near-infrared (NIR) region.² One concern for these traditional nanocrystals are the use of heavy metal materials, which are potentially toxic to biological systems if leached as ions.³ Therefore, heavy metal-free materials, such as InP and GaP nanocrystals have developed, albeit with the less favourable optical properties. In addition, silicon QDs have been studied for biological applications since they have lower risk of toxicity and are potentially biocompatible. However, significant challenges remain with the smaller absorption coefficients and quantum yields of Si QDs as indirect bandgap semiconductors, and with the efficient preparation of high quality Si nanocrystals and surface modifications for enhanced stability and optical properties.⁴ Core/shell CdX/ZnS materials thus remain the leading QD materials, particularly as studies have shown that high quality shells and coatings (*vide infra*) render CdX QDs acutely non-toxic.⁵⁻⁷

CdSe quantum dots are usually synthesized by injecting Cd and Se precursors (*e.g.* $\text{Cd}(\text{CH}_3)_2$,⁸⁹ CdO ,¹⁰ $\text{Cd}(\text{Ac})_2$,¹¹ $(\text{TMS})_2\text{Se}$ ⁸) into a hot organic solvent (*e.g.* trioctylphosphine oxide (TOPO)⁸ and hexylphosphonic acid(HPA)⁹), which will nucleate small nanocrystals. When temperature is decreased, small nanocrystals grow without further nucleation until a certain size is reached and the reaction is stopped.¹² Hydrophobic ligands (*e.g.* TOPO, alkyl amine and oleate ligands) cap

the surface of these nanocrystals and provide colloidal stability in hydrophobic solvent.¹³ For many photoluminescence (PL)-related applications, a thin shell (*e.g.* ZnS) is coated around the core nanocrystals to passivate surface dangling bonds and reduce non-radiative recombination of electron-hole pairs, substantially increasing the quantum yield (QY) of the QDs.¹⁴ For a more uniform and efficient shell to further enhance the QD QY, the lattice match between core and shell materials are very important. Different methods are developed to reduce the lattice strain, such as using alloyed materials as a shell.¹⁵

1.1.2 Optical properties

QDs have become attractive probes for biological imaging and analysis, in large part, because of their unique combination of optical properties compared to other luminescent materials. First, the relatively high QY ($\approx 0.2\text{--}0.9$) and large molar absorption coefficients ($\epsilon \approx 10^4\text{--}10^6 \text{ M}^{-1}\text{cm}^{-1}$) yield high brightness¹, which improves the detection sensitivity. Second, QDs have very narrow and symmetric emission spectra with a full-width-at-half-maximum (FWHM) around 25-35 nm, and the wavelength peak can be tuned across a range of *ca.* 200-300nm based on the nanocrystal size, enabling multiplexed imaging with little or no overlap between PL emission signals. (see **Figure 1.2 (B)**) Third, the absorption spectra of QDs are broad, which allows different colours of QD to be excited simultaneously at a single excitation wavelength. (see **Figure 1.2 (A)**) Compared to conventional organic dyes, QDs have a better resistance to chemical degradation and photobleaching, which is extremely useful in biological imaging.

One potential drawback of the PL properties of QDs is that they ‘blink,’ where the PL fluctuates between “on” and “off” states through complex physical pathways. Two mechanisms occur in the same QDs: (i) Auger recombination, which occurs when energy from non-radiative recombination transfers to a third charge carrier; and (ii) band-edge carrier trapping, which is followed by nonradiative recombination.^{16,17} Efforts have recently been made to develop nonblinking QDs.¹⁸

In addition to their PL, other advantages of QDs for biological applications include their large surface area for interfacial chemistry and small size (relative to other nanoparticles) for entry into biological systems.

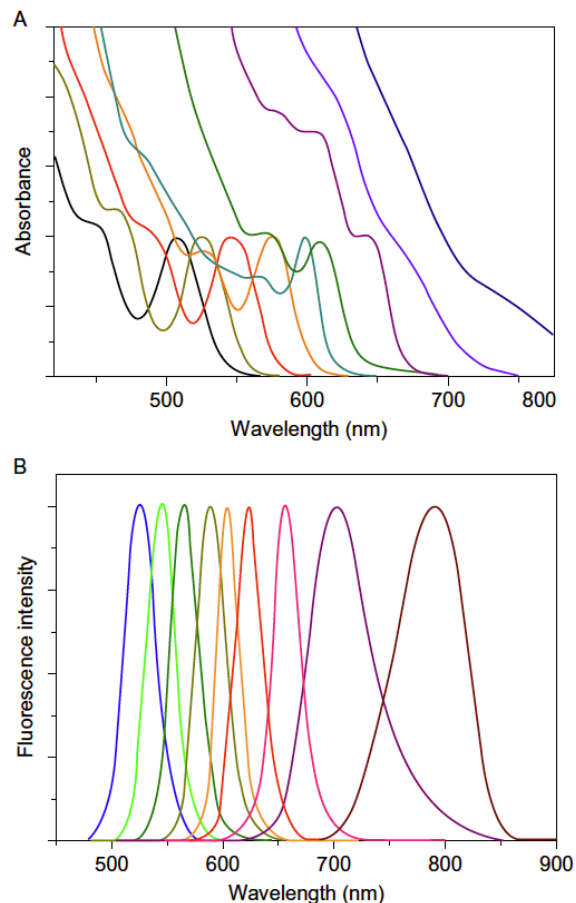


Figure 1.2 (A) Absorption and **(B)** emission spectra of CdSe/ZnS core/shell QDs of different sizes (from left to right: QD525, QD545, QD565, QD585, QD605, QD625, QD655, QD705, QD800). Figures reprinted with permission from Ref.¹⁹

1.1.3 Surface functionalization and bioconjugation of QDs

Most methods for the synthesis of high-quality QDs involve hydrophobic surfactants, so there are always hydrophobic ligands on the surface of native QDs, leading to their aggregation in aqueous solutions. To increase the colloidal stability and dispersion of QDs in aqueous solutions, a hydrophilization process follows QD synthesis. The requirement for the appropriate chemistry is

to colloiddally stabilize QDs in aqueous solutions over sufficiently broad ranges of pH and ionic strength, while not compromising their optical properties. The surface chemistry should also add functional groups to the QD surface for downstream bioconjugation. A hydrodynamic diameter after hydrophilization that is small (*i.e.* similar to the hard QD diameter) is preferred for some biological applications.

One of the most commonly used strategies for hydrophilization is to exchange the organic ligands with hydrophilic ligands. These ligands are usually bifunctional molecules that have one end anchored to the QD surface with high affinity (*e.g.* by a thiol group) and the other end a hydrophilic group to disperse the QDs in aqueous solution and provide available sites for bioconjugation. Examples of such linker molecules are mercaptoacetic acid (MAA), dihydrolipoic acid (DHLA), polyethylene glycol (PEG)-terminated DHLA, and L-glutathione (GSH).^{20,21} Ligand exchange yields hydrophilic QDs with a relatively small hydrodynamic size, but sometimes decreases the QY of PL.

Another hydrophilization strategy is to encapsulate QDs within amphiphilic polymers, such as PEGylated gallate amphiphiles.^{22,23} These polymers have multiple hydrophobic and hydrophilic units that can form a stable long-term coating around the native QD through strong hydrophobic interactions. Since the polymer coating does not risk creating more surface traps by removing the original non-polar ligands, this method can better maintain the brightness of QDs compared to the ligand exchange method. However, it will lead to a greater hydrodynamic diameter after the hydrophilization.

Lastly, silanization of the QD surface has been used to grow a silica coating.^{24,25} Silica coatings help prevent nanocrystals from chemical degradation (*e.g.* oxidation) in different outer environments and maintain their colloidal stability. Additionally, the silica makes QD more biocompatible and also can be utilized for further functionalization.

In order to use QDs as biological probes, it is important to develop bioconjugation methods for different applications. QDs can be conjugated to a variety of biomolecules, including antibodies,

oligonucleotides, proteins, peptides, and enzymes to target and detect analytes of interest for biosensing and to enable specific cellular imaging.²⁶ QD-antibody conjugates are commonly used in cellular imaging and flow cytometry, which will be discussed in the following section.

Two of the main bioconjugation strategies with QDs are (i) covalent coupling of biomolecules to a ligand or amphiphilic coating on QD surfaces, and (ii) non-covalent binding of biomolecules. For covalent linking, biomolecules will be directly reacted with the ligand or amphiphile functional groups on the QD surface. (see **Figure 1.3 (A)**) One of the most popular strategies is *N*-(3-dimethylaminopropyl)-*N*'-ethylcarbodiimide (EDC)-mediated condensation to form amide bonds between carboxyl (*e.g.* QD coating) and amine groups (*e.g.* biomolecule). Another common covalent chemistry is maleimide coupling;²⁰ for example, a heterobifunctional crosslinker (*e.g.* sulfo-SMCC) can be used to conjugate amines to thiols.²⁷

Non-covalent binding can be achieved through electrostatic attractions, and by affinity interactions between biomolecules and QD surfaces (*e.g.* coordination bonding). (see **Figure 1.3 (B)**) In general, a QD's large surface area enables the non-specific adsorption of a broad range of biomolecules and macromolecules, including proteins, peptides, nucleic acids, and polymers. Electrostatic attraction between QDs with anionic functional groups (*e.g.* carboxyl group) and net positively-charged proteins are commonly used as a simple and fast method. However, electrostatic interactions offer little or no control over the species (if a mixture), orientation, and number of biomolecules adsorbed on the QDs. This approach is also prone to variation from environmental changes such as pH, ionic strength, and addition of other competitive molecules. High-affinity interactions provide better control of bioconjugation on the QD surface. Biotin-avidin conjugation is one of the most ubiquitous protocols since streptavidin-functionalized QDs are commercially available (prepared by covalent conjugation) and the biotinylation of biomolecules is straightforward. The biotin-avidin interaction is very stable due to its high association constant ($K_A \sim 10^{15} \text{ M}^{-1}$) but the size of QD bioconjugates is relatively large. Another high-affinity approach is bioconjugation through coordination chemistry, which can offer control the orientation of biomolecules and also the quantities bound through available sites on the QD surface. For example, the imidazole groups in polyhistidine tags can be coordinate to the transition

metal sites (e.g. zinc) on the outer shell of QDs.²⁸ Thiol-functionalized biomolecules (e.g. oligonucleotides) are also used to coordinate the zinc moieties on the QD surface.

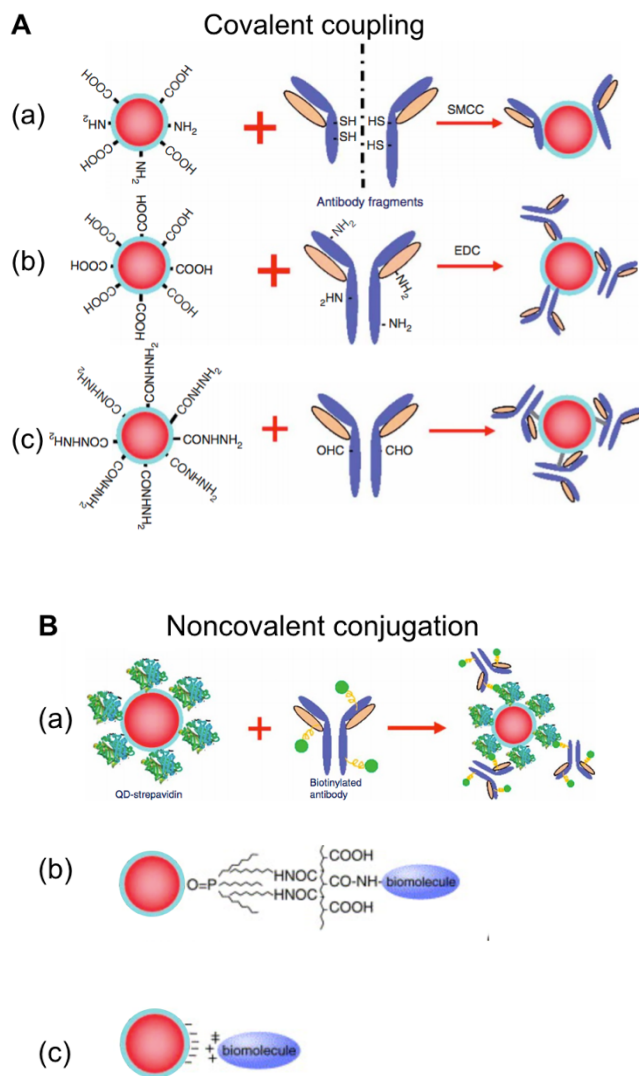


Figure 1.3 Schematic illustration of some common bioconjugation strategies with QDs. **(A)** Covalent coupling: **(a)** QD-antibody coupling between amine groups and thiol groups with SMCC; **(b)** QD-antibody coupling between carboxy groups and amine groups using EDC; and **(c)** QD-antibody conjugation between hydrazide-modified QDs and oxidized carbohydrate groups on antibodies. Reproduced with permission from refs.²⁹ **(B)** Noncovalent conjugation via **(a)** streptavidin-biotin interactions, **(b)** hydrophobic attraction, and **(c)** electrostatic attractions. Reproduced with permission from refs.³⁰

1.1.4 Quantum dots as biological imaging agents

Many studies have used QDs or QD-based nanocomposites as fluorescent probes for cellular imaging due to their extraordinary photophysical properties.³¹⁻³⁴ A good cellular imaging probe should be specific to the cell of interest, resistant to photobleaching for long-term measurements, water-stable, and bright enough to achieve a high signal-to-background ratio in biological environments.³⁵ QDs meet these criteria when used in combination with suitable surface chemistry and bioconjugation strategies. QD-based composite materials have also been developed for making multifunctional bioimaging tools. For example, QD-based nanocomposites containing magnetic nanoparticles allow rapid and easy isolation of specific cell types for imaging.³⁶ Alternatively, for optical barcoding, multiple copies of single or different colors of QDs are incorporated within a single silica or polymer nanoparticles. The detection of up to 10^6 target biomolecules such as proteins and nucleic acid sequences can (theoretically) be encoded by the specific spectroscopic signatures of these beads using, for example, six colors and 10 intensity levels.³⁰

Compared to conventional organic dyes, the greater brightness and resistance to photobleaching of QDs provide higher sensitivity and stability during short-term, long-term, and repeated measurements, which is particularly beneficial for biological imaging due to the autofluorescence background of some samples. The narrow emission spectra of different QDs at a single excitation wavelength also simplifies multicolor imaging. QDs of multiple colors can be conjugated with biomolecules that bind to specific cells or antigens of interest; for example, (i) antibodies, (ii) peptides, (iii) small molecules, and (iv) high-affinity fusion tags.³⁷ Antibody-based targeting is the most common strategy for many assays and for cellular and tissue imaging applications.

Preparation strategies of QD-antibody bioconjugates have included avidin-biotin interactions,³⁸ EDC chemistry,³⁹ and conjugation with short-chain cross-linkers³⁹. Many antibody conjugation kits are commercially available for highly-specific cell targeting. Similar to commercial fluorescent dyes, QDs-antibody conjugates can specifically label cells through either indirect or direct approaches. (see **Figure 1.4**) QDs conjugated with a primary antibody bind directly to target antigens on cells. Alternatively, QDs conjugated with a secondary antibody bind to a specific

region of the primary antibody, where the primary antibody is unconjugated and binds directly to cells. The indirect pathway is usually more sensitive than the direct pathway since more than one secondary antibody can bind to a single primary antibody, and is more flexible for antibody selection. For nanoparticles, the indirect approach may also reduce steric hindrance toward cell binding. However, there might be cross-reactivity when there are multiple secondary antibodies incubated simultaneously.⁴⁰

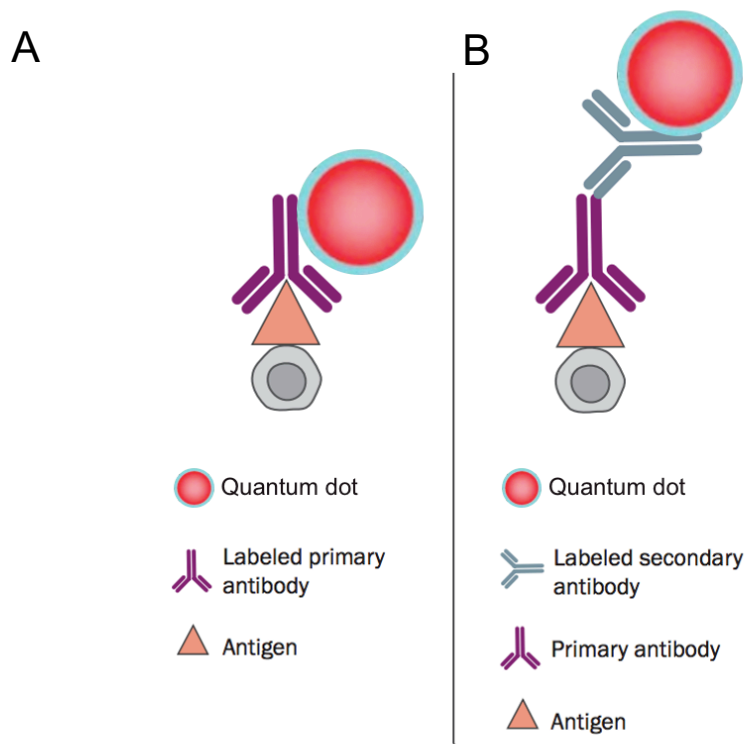


Figure 1.4 Schematic illustration of (A) a QD conjugated with primary antibody and directly bound to a cell, and (B) a QD conjugated with secondary antibody and bound indirectly to a cell through binding primary antibody. The cell is shown in grey. Reproduced from ref.⁴⁰

Applications of QD-antibody conjugates as fluorescent reagents include immunohistochemistry and flow cytometry. Immunohistochemistry is used to analyze labeled cells or tissues for different antigen expression levels. Several groups have shown single or multicolor quantitative immunohistochemistry with QDs for cancer cells,^{41,42} tissue specimens,^{29,43,44} and clinical

biopsies.⁴⁵ Overall, QDs have shown better sensitivity and multiplexing capabilities for profiling genetic and protein biomarkers in biological samples.

Flow cytometry (FC) provides information about cellular antigens based on the fluorescent immunolabeling of cell populations. Fluorescence-activated cell sorting (FACS) physically sorts cells of interest based on that labeling. Multicolor FC requires consideration about the excitation and emission characteristics of the fluorescent probes and usually requires more than one laser source. In this respect, one of the most beneficial properties of QDs is their broad excitation spectra, which allow multiple QDs to be excited by a single laser and therefore reduces the complexity of multicolor flow cytometer dramatically. Also, the narrower emission spectra of QDs versus organic fluorochromes reduces emission overlap between labels and colour channels. With QDs, the capability of polychromatic flow cytometry was extended to resolve 17 fluorescence signals, exceeding the (at the time) limit of 12 colours with organic fluorophores.⁴⁶ When developing staining panels with QDs, a typical process includes (i) identifying proteins of interest and finding corresponding antibodies; (ii) assigning the marker to one of the three categories (primary, secondary, and tertiary) based on its expression levels; and (iii) choosing fluorochromes or QDs based on these categories. The brightest fluorochromes will be used for tertiary marker, which has lowest expression.⁴⁷

1.2 Point-of-care (POC) diagnostics

1.2.1 POC diagnostics for biological analysis

Among other factors, increasing globalization, an aging population, and substantial regional and social inequality in health care are driving interest in POC diagnostics. That is, shifting biological analytical platforms away from sophisticated laboratory instruments and toward simpler, lower cost, and more portable devices. POC technologies will enable people to get diagnostic results without the restrictions of place, time, or highly-qualified personnel, which will have significant impact in developing countries and other regions or communities with limited health care resources and infrastructure. At the end of 2019, the fast-spreading coronavirus (COVID-19) has affected over 100 countries globally, causing more than 125 million people infected and 2,753, 398 deaths

by March 25th, 2021. When facing such pandemics, the conventional clinical testing process cannot satisfy the high demand and short times that are essential to management. A main limitation is the reliance on specialized laboratory equipment and highly-trained personnel, which is often time-consuming. POC devices have the potential to quickly screen people, track confirmed cases, and stop the spread of infection.⁴⁸⁻⁵⁰ The requirements for POC devices are cost-effectiveness, user-friendliness, rapid analysis times, portability, and sensitivity and detection limits that align with clinical diagnoses.

Different biomarkers are targeted as analytes for POC diagnostics, including nucleic acids, proteins, genes, metabolites, and other biochemical substances from human tissues or body fluids (*e.g.* blood, sweat, urea, saliva, *etc.*). The frequent challenge in detection is the low level of biomarkers in a complicated biological sample. In well-equipped laboratories, multiple steps for sample preparation are often utilized before analysis, and/or signal allowed to develop over many hours, leading to long processing times. For example, the well-established polymerase chain reaction (PCR) method usually takes 3-5 h per test. Therefore, the development accurate and rapid POC diagnostics methods that meet both clinical and cost requirements is a substantial challenge.

1.2.2 Synopsis of POC diagnostics

In the studies of POC diagnostics, some technologies have already been widely used in clinics (*e.g.* Lateral flow test strips and handheld meters), some are tested in laboratory-scales with clinical samples (*e.g.* smartphone-based assays, lab-on-a-chip platforms), while others are more fundamental science and under development in research communities for next-generation POC diagnostics (*e.g.* molecular assays). Paper-based assays have become a trend for POC diagnostics due to its low cost and simple operation. Two of the well-known formats include lateral flow assays (LFAs) and microfluidic paper-based analytical devices (μ PADs).

Over the last half century, one-step LFAs have been developed and used in many applications, especially for on-site detection relevant to environment monitoring^{51,52}, medical tests^{53,54,63,55-62}

and toxin residue detection in food^{64–71} and water samples.^{72–74} The most popular LFA is the pregnancy test strip for detection of human chorionic gonadotropin (HCG) level.

A typical LFA test strip includes several components: sample pad, conjugate pad, polymer membrane, and adsorbent pad. A sample is applied to the sample pad and transported through the test strip by fluid wicking. Specific detection agents (*e.g.* antibodies) linked with colorimetric or fluorescent labels on the conjugate pad will bind the analyte of interest to form an analyte-detection agent complex. Analyte-detection agent complexes and free detection agents will flow through the polymer membrane through capillary action and accumulate in the test and control zones, respectively, which have immobilized antibodies to capture the foregoing. Excess sample solution is absorbed by the adsorbent pad to prevent the backflow of reagents. A visible signal at the control line shows the validity of the test strip and a signal at the test line shows the existence of the analyte. Most of the LFAs on the market currently only give qualitative results and semi-quantitative results with a limited choice of analytes. Another obstacle to the widespread clinical use of LFAs is lack of sensitivity when the concentration of analytes is low, which may generate false-negative results. In order to increase the sensitivity and specificity toward multiple analytes, different types of LFA test strips have been developed, including fluorescent LFAs^{58,66,67,75,76} with a test strip reader and multiplexed LFAs with multiple test zones.^{77–79} Isothermal amplification methods for nucleic acids have also been combined with LFAs for more sensitive and accurate results, including loop-mediated isothermal amplification (LAMP)⁸⁰ and recombinase-aided amplification (RAA)⁸¹.

μ PADs include an inlet to introduce sample, one or microfluidic channels to guide liquid flow, a barrier to prevent potential leakage and an outlet for chemical or biological reactions.⁸² These features on the paper can be designed and printed out via wax printing, inkjet printing, photolithography, and other fabrication techniques. Applications of these paper-based assays have been demonstrated for clinical assays^{83,84} and also water quality and environmental waste control.^{85,86}

In addition to low-cost paper, other lab-on-a-chip platforms are developed using substrates such as glass, silicon, and polymers (*e.g.* polydimethylsiloxane (PDMS), polymethyl methacrylate (PMMA)).

The development of smartphone-based POC devices is an increasingly popular strategy. Development often falls into one or both of the following categories: (i) the smartphone is used as a readout platform for a biochemical assay (*e.g.* paper-based assays,^{87–90} microarray-based^{91–94} or cuvette-based immunoassays⁹⁵); (ii) integrated with peripheral optical components to be alternative of bulky and expensive lab equipment (*e.g.* microscopes,^{96–100} spectrometers^{101–104}). When utilized as readout platforms of biological assays for quantitative analysis, the image captured by a smartphone camera is the raw data. These concentration levels of biomarkers in the sample are obtained based on the fluorescence intensity of the test samples. A smartphone camera may also be converted to a lightweight, cost-effective, and compact microscope or spectrometer with additional optics, which will be mentioned in **Section 1.2.3**.

1.2.3 Smartphone-based POC diagnostics

Over the past two decades, portable consumer electronic devices have developed rapidly and utilized for POC diagnostics as a quantitative readout platform. Commercialized optical strip readers (*e.g.* AlereTM reader, manufactured by Abbott) were developed for analyzing completed LFAs and provide quantitative results in a few seconds. CD/DVD drives, scanners, digital cameras and smartphones—all of which are commonly found in our homes—have been used as an optical readout devices for POC diagnostics.¹⁰⁵ In 2020, there were nearly 3.8 billion smartphone users in the world, equal to ~45% of the global population. Smartphones have been penetrated everyday life so much that it is predicted that the number of smartphone users will double in the next three years.

Smartphones have many potential benefits as POC diagnostic devices. First, their portable size and wide range of functions and computational power make them easily carried, user friendly, and versatile. Second, most smartphones support multiple modes of wireless connectivity to the Cloud,

such that data such as diagnostic test results can be processed, tagged with date, time, location and biometric information, and transferred to the health professionals anywhere in the world to get feedback in a short time. Third, the advanced and still fast-developing camera hardware (*e.g.* CMOS image sensor) allows for increasingly sensitive detection of optical signals. The flashlight embedded in a smartphone can also be utilized as a potential light source for fluorescence-based assays and the battery can provide power to peripheral electronic or mechanical components.

In order to adapt smartphones to optical bioimaging applications, a 3D-printed or machined opto-mechanical attachment is usually built to integrate all the necessary optical components together for a satisfactory signal-to-noise ratio (SNR). Light sources commonly used for the excitation of fluorescent probes include single-color light-emitting diodes (LEDs) made from specific semiconductor materials, broadband phosphor-based LEDs (*e.g.* smartphone flashlight), and laser diodes. LEDs are beneficial for POC diagnostic devices since they do not require much power (< 5 V, milliamp currents) and are low cost ($< \$1$ per LED). They are often used when a relatively broad excitation is required or adequate, whereas laser diodes are more suitable for applications that require more intense and monochromatic ($\text{FWHM} < 1\text{ nm}$) excitation. In order to minimize the scattering light from the excitation source and collect only the fluorescence signals from the sample, a bandpass filter or longpass filter is utilized in front of the smartphone camera. An external lens may be put in front of a smartphone camera lens in order to magnify the object being imaged or to increase the field-of-view. With a short-focal-length external lens ($f = 4\text{ mm}$), a smartphone setup built by the Ozcan group was able to see single fluorescent nanoparticles and viruses.¹⁰⁶ Today, with an increasing market demand, more smartphone companies have put focus on the camera system. Samsung smartphones (*e.g.* Galaxy S8) allow people to manually adjust camera settings (*e.g.* f-number, ISO speed, exposure time), which is extremely useful for fluorescent measurements. Recent studies have demonstrated improvement of image resolution through machine learning^{107,108} and many useful smartphone apps are available for advanced video recording or image capture (*e.g.* camera FV-5, ProCamera, Filmic Pro, etc.).

1.2.4 Smartphone camera technology

Smartphone camera technology has seen dramatic improvements over the past decade, providing technical capacity for both social and even scientific uses. Scientific applications include biomedical imaging (*e.g.* brightfield and fluorescent imaging), color analysis of images (*e.g.* evaluation of corrosion,¹⁰⁹ colorimetric measurements for paper-based assays), fluorescence measurements, and spectrophotometry. In terms of quantitative measurements, it is critical to obtain accurate color and spectral information. Two common smartphone image formats include RAW image and JPEG image. In both formats, data will be stored as intensity values for single pixels in analog-to-digital conversion units (ADU). JPEG is a commonly used format for digital images and is based on lossy spatial compression, which minimizes the file size but compromises image quality. RAW files contain the unprocessed data for people who want to conduct manual post-processing, which is preferable for quantitative analysis in scientific applications. The most advanced smartphones in the market today also allow users to adjust camera settings manually to best suit the imaging environment or objective (*e.g.* exposure time, ISO speed, camera aperture, etc.). *Exposure time* determines how long the sensor is exposed to the light prior to electronic readout. When the exposure time is increased, more light is captured to form a brighter image, which is useful in low-light scenes. *ISO speed* is analogous to the detector gain in microscopy, being a measure of the sensitivity of the image sensor to light. Increasing the ISO speed will amplify the electrical signals converted from the light falling on the image sensor, and thus boost the intensity of both signal from the sample and noise from the background. *Aperture* is often displayed as f-numbers in smartphones and controls the amount of light that enters the camera to reach the image sensor. These optical parameters should remain constant while conducting quantitative analysis and comparing between different samples.

CMOS-based image sensors are most commonly used in modern smartphone camera systems. Bayer filters are added in front of the CMOS sensors for selective color transmission. A Bayer filter is a colour filter array with a repeating square pattern with two green pixels for every one red and blue pixel (see **Figure 1.5**). This color pattern was developed to mimic the color sensitivity of human eyes. The spectral responses of various smartphone cameras were characterized over a range of 390-700 nm using either a monochromator or a spectrometer add-on component and all

of the tested image sensors are most sensitive to green light. For smartphone-based spectrometers, the spectral responses of the image sensors must be considered and calibrated before data processing.¹¹⁰

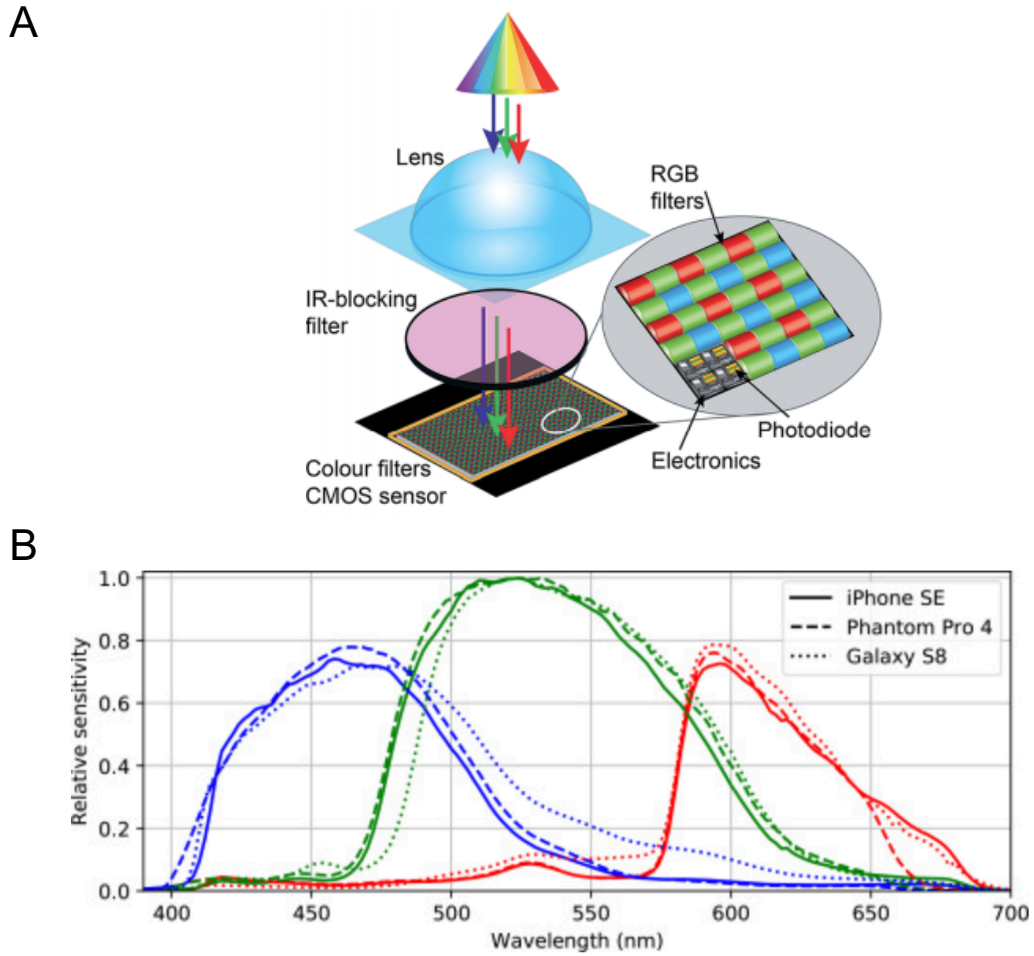


Figure 1.5 (A) Illustration of CMOS image sensor with Bayer filter. Reproduced from ref.¹⁰⁵ **(B)** Normalized spectral response curves of different smartphone models, derived from monochromator data. Reproduced from ref.¹¹⁰

1.3 Flow cytometry

1.3.1 Conventional flow cytometry

Flow cytometry (FC) is a widely-used technology in fundamental research and clinical practice that provides physical and biochemical information about single cells or particles. Fluorescence activated cell sorting (FACS) also separates cells based on their measured characteristics. It is able to analyze millions of cells with a high rate (>10,000 cells per second), offering scientists and clinicians the large-scale data sets and statistics necessary for drawing significant conclusions from heterogeneous cell populations. As shown in **Figure 1.6**, a typical flow cytometer consists of a fluidics system, one or more lasers, excitation and collection optics, fluorescence filters, sensitive photodetectors, and supporting electronics. Liquid suspensions of single cells or particles of interest are directed one-by-one, using a sheath flow of fluid, to the focus of the excitation light source. Optics and wavelength-selective filters transmit the scattered or fluorescent light from the single cells/particles to the photodetectors, where the optical signals are ultimately converted to digital data. The two most common types of photodetectors are photomultiplier tubes and photodiodes.¹¹¹

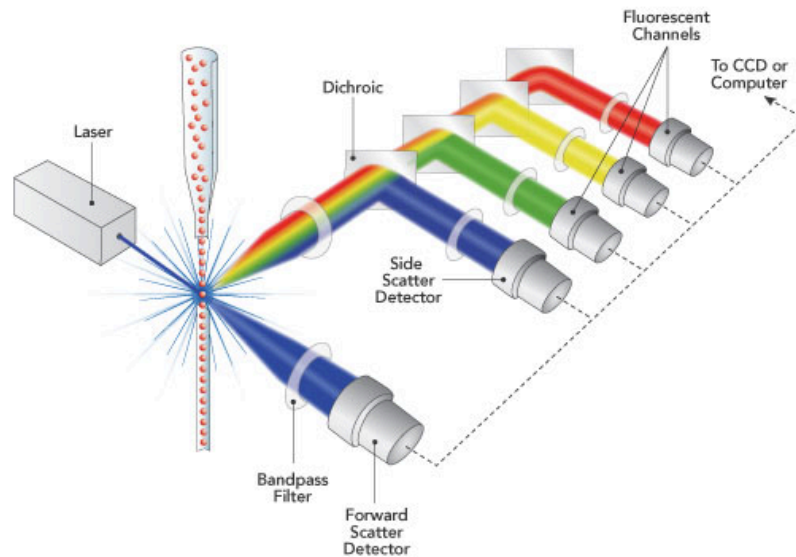


Figure 1.6 Generic diagram of a multicolour flow cytometer with scatter and fluorescence detection channels. The single cells are illustrated as red spheres. Only one or multiple possible laser sources is shown. Reproduced from ref.¹¹²

Flow cytometry has a variety of applications in cell counting and sorting, immunology (*e.g.* immunophenotyping, antigen specific responses, cell proliferation, apoptosis analysis), molecular biology (*e.g.* protein expression, RNA expression, cell cycle analysis), and disease monitoring.¹¹³

Important features of the fluorescent probes that are used to stain the cells or label specific biomolecules are their absorption spectrum (relevant to laser excitation), their emission spectrum (relevant to the detection channel, and their brightness (the product of molar absorption coefficient and fluorescence quantum yield; relevant to sensitivity). The difference between the band maxima of the absorption and emission spectra, known as Stokes shift, determines how efficiently the excitation light and emitted fluorescence can be separated. Common fluorochromes include fluorescein isothiocyanate (FITC) and other derivatives, various rhodamine and cyanine dyes, phycoerythrin (PE) and allophycocyanin (APC) for labeling antibodies; ethidium bromide (EB) and propidium iodide (PI) for staining nucleic acids; and green fluorescent protein (GFP)-family fluorescent proteins as reporter molecules.¹¹¹ Multiple colors of fluorescent probes are distinguished by their combination of absorption and emission spectra. Pairs of fluorescent probes need only differ significantly in one of these spectra to be distinguished. Since organic dyes and

fluorescent proteins tend to have broad emission spectra, overlapping fluorescence emission spectra are common, nominally dye-specific fluorescence signals often need to be corrected for crosstalk after detection, which is called *compensation*. Fluorescent nanoparticles have also been developed as flow cytometry probes, including QDs⁴⁶ and semiconducting polymer dots.¹¹⁴

Data analysis is a critical component in flow cytometry for biological research. The gating strategy, which separates multiple regions based on selected parameters, is used to define the characteristics of a set of cells or particles. A *gate* is a subset extraction with a set of points displayed on a histogram, 2-D or 3-D plot. When facing large datasets and more complicated gating with multiple parameters, computational flow cytometry is used to provide more efficient and reproducible analysis. The quality and analysis time of automated gating process is closely related to the algorithms used. A series of techniques was recently reviewed and the run times for each technique were provided, ranging from a few seconds to several hours depending on the cell populations.¹¹⁵

1.3.2 Microfluidic systems

Microfluidic systems allow analyses in small sample volumes and have been combined with flow cytometry in recent years. *Microfluidics* is defined as a technology that uses channels or other features with micrometer-scale dimensions to control the flow of small amount of fluids (typically 10^{-9} - 10^{-5} L within a channel).¹¹⁶ Microfluidic technology is well-suited to POC diagnostics because the microfluidics chips are compact and able to rapidly separate and analyze very small quantities of samples with high sensitivity. Microfluidic systems typically consist of four parts: an inlet for delivery of sample, a pressure-based pumping system or other mechanism (*e.g.* electroosmotic flow) for driving fluid flow, channels with designed patterns to mix or separate fluids, and an outlet for collecting samples or waste.

The most widely used microfluidic channel material for biological applications is polydimethylsiloxane (PDMS, a silicon-based polymer), usually prepared on a glass substrate using soft lithography methods. PDMS has many advantageous properties as a material; it is (i) low cost (~\$80/kg) and commercially available, (ii) non-toxic and biocompatible, (iii) optically

transparent, (iv) viscoelastic, (iv) curable at a relatively low temperature, (v) able to adhere to a variety of surfaces reversibly, and (vi) amenable to surface functionalization after oxygen plasma treatment. 2D and 3D PDMS-based microfluidic devices have, for example, been developed for cell culture^{117–119} and cell analysis.^{120,121}

One obstacle of PDMS-based devices is the hydrophobicity of native PDMS, which may cause significant non-specific absorption of proteins, other biomolecules, and hydrophobic molecules. Much research has been done over the past decade to modify the surface of PDMS and increase the wettability of microfluidics channels. Methods have included plasma treatment,¹²² surface oxidation,¹²³ hydrosilanization,¹²⁴ chemical vapor deposition,¹²⁵ layer-by-layer deposition,¹²⁶ and polymer coating.¹²⁷ While plasma treatment is the most efficient and simple method to obtain a hydrophilic surface, a recovery of hydrophobicity was found after a short time due to the migration of uncured PDMS oligomers to the PDMS surface to minimize surface energy, as well as the elastomeric properties of PDMS to recover mechanically.¹²⁸ Extraction of the uncured oligomers and covalent bonding with other chemical reagents can help reduce this hydrophobic recovery process, maintaining the hydrophilic nature of PDMS surface for up to one week under dry storage.¹²⁹ A reduction of non-specific adsorption of protein was observed on an hyperbranched polyglycerol (HPG)-modified PDMS microfluidic channel.¹³⁰

Laminar flow, predicted by the Reynolds number, will occur in most microfluidics systems given the channel dimensions and flow rates.¹³¹ With laminar flow, cells or particles can be directed with predictable trajectories through microchannels.

1.3.3 Single-cell analysis

Ensemble cell-based assays have the drawback that the average results from a population of cells may be misleading and obscure heterogeneity and information from individual cells and sub-populations. Single-cell analysis can be used to measure the expression level of specific biomarkers on individual cells, allowing heterogeneity and sub-populations to be revealed. Indeed, one of the main benefits of flow cytometry is single-cell analysis.

Single-cell analysis has a critical role in early-state disease monitoring. For example, understanding the different biomarkers expressed on tumor cells can provide important information on cancer progression, and guide the proper treatment of cancers and direct antitumor drug development. Tumors are complex biological systems with heterogenous cell populations. To reduce the complexity in research, different cell lines cultivated *in vitro* are often used to represent cell populations in tissues and organs of the human body.¹³² To help understand the occurrence and progression of cancer better, genome, transcriptome and proteome profiling have been done for different disease states. Proteome profiling gives more information on the development of cancer since the expression levels of protein molecules are closely related to the metastatic process of tumors.¹³³ Different expression levels of the biomarkers can be used to distinguish different cell types and sort cancer-related cells from normal cells. For example, the overexpression of epidermal growth factor receptor (EGFR, ErbB1) and human epidermal growth factor receptor 2 (HER2, ErbB2) protein is found with many tumor cell lines, and the expression levels have been quantified for 61 tumor cells lines derived from 12 tumor types.¹³⁴ Mucin 1 (MUC1) was found overexpressed in triple-negative breast cancer cell lines (*e.g.* MDA-MB-231 cells), which lacks HER2, estrogen receptors (ER) and progesterone receptors (PR), and has been linked to tumor aggressiveness in human breast carcinoma.^{135,136} Epithelial cell adhesion molecule (EpCAM) has high expression levels on circulating tumor cells (CTCs) but no expression on normal blood cells, enabling efficient separation of CTCs from blood samples. In late-stage cancer, high levels of CTCs and other cancer biomarkers are often found in the blood stream of the patients. Studies have also found that low levels of CTCs can also be detected at a relatively early stages of tumor growth, which is useful for cancer diagnostics.¹³⁷ The development of high-throughput microfluidic systems allows for cell selection, isolation and single-cell analysis on a small chip.^{138,139} Isolation of CTCs with 100% purity from a mixed population of cells has been demonstrated with a microfluidic device, where variations of EGFR mutations were tracked during anticancer therapy.¹⁴⁰

1.4 Contribution of this thesis

The detection and enumeration of specific cell types can provide critical information for early and efficient disease screening, including cancers. For example, identifying a specific cancer type from analysis of the cells of a cancerous tissue sample is important for prescribing the treatment that is most appropriate for the patient. To this end, doctors categorize breast cancers into four different groups based on the genetic information of the cancer cells, which include luminal A group, luminal B group, HER2 positive group, and basal-like group. Based on the group identified, specific treatments like chemotherapy, hormone therapy, or targeted treatment to HER2 genes are selected for patients. As noted earlier, flow cytometry (FC) is commonly used to measure the physical and biochemical characteristics of cancer cells for classification and sorting. However, the cost, size, and sophistication of the method makes it unsuitable for use outside of specialized laboratories. Capability similar to FC, but in a format suitable for POC application, would enable new opportunities and possibilities for medical diagnostics and health care.

Here, a smartphone-based FC system was developed by integrating a laser diode, a polydimethylsiloxane(PDMS)-on-glass microfluidic chip, and an optical magnification system into a compact 3D-printed box that interfaced with a smartphone and its camera. Photoluminescent silica-QD supra-nanoparticle assemblies ($\text{SiO}_2\text{@QD}$) were coated with dextran and used as high-brightness materials for immunolabeling of cells through tetrameric antibody complexes (TACs). The high brightness enabled the smartphone FC to image and count the target cells. For multiplexed analysis of multiple antigens and multiple cell types, different colours of $\text{SiO}_2\text{@QD}$ were coated with carboxymethyl-dextran (CM-Dex) and conjugated to antibodies targeting different cell-surface antigens. Selective enumeration of multiple cancer cell lines was achieved using a combination of red, orange, yellow, and/or green $\text{SiO}_2\text{@QD}$ -antibody conjugates. Smartphone videos of labeled cells under flow were analyzed with an algorithm in MATLAB that extracted PL colour features, classified the cells with a support vector machine model, and counted the cells. The research in this thesis is an important advancement toward cell-based POC diagnostic assays and toward the use of smartphones as bioanalytical tools.

This thesis is organized into four chapters, including the current introductory chapter. Chapter 2 summarizes the experimental methods used in the research. Chapter 3 presents and discusses the main results of the research. Chapter 4 summarizes the conclusions of the research and suggests avenues for future work. The appendices provide additional details about data analysis.

Chapter 2: Experimental Methods

2.1 Materials

Anti-HER2 antibody (Catalog No. NBP2-32863, Clone HRB2/282, IgG1 Kappa) was from Novus Biologicals (Centennial, CO). Anti-EpCAM (Catalog No.60147, Clone 5E11.3.1, IgG1 Kappa), anti-CD44 (Catalog No. 60068, Clone IM7, IgG2b Kappa), anti-MUC1(Cat No. 60155, Clone 16A, IgG1 Lambda) and Do-It-Yourself Positive Selection Kit II (Catalog No. 17698) were from STEMCELL Technologies (Vancouver, BC, Canada). Anti-ER antibody (Catalog No. ab66102, C-542, IgG1) was purchased from Abcam (Toronto, ON, Canada). Dextran (*Leuconostoc mesenteroides*, 9000–11000 Da MW or *Leuconostoc* spp. ~6000 Da MW) and carboxymethyl-dextran (CM-Dex, *Leuconostoc mesenteroides*, 9000–11000 Da MW), sodium (meta)periodate, 1-(3-aminopropyl)imidazole (API), sodium cyanoborohydride, tetramethyl ammonium hydroxide (TMAH), and reduced L-Glutathione (GSH) were from Sigma-Aldrich (Oakville, ON, Canada). Ammonia solution (28-30%) was from VWR (Mississauga, ON, Canada). McCoy's 5A modified medium, Dulbecco's Modified Eagle's Medium (DMEM), boric acid and ethylenediaminetetraacetic acid (EDTA) were from Fisher Scientific (Toronto, ON, Canada). 1X PBS buffer (–) was from Gibco Life Technologies. Easy sep buffer was PBS buffer supplemented with 2% v/v fetal bovine serum (Sigma Aldrich) and 1 mM EDTA (Fisher Scientific). Sodium tetraborate decahydrate was from Amresco (Solon, OH, USA). Dialysis membrane (3.5 kDa MWCO) was from Spectrum Laboratories (Rancho Dominguez, CA, USA). Deionized water was purified from a Milli-Q Synthesis water purification system (Millipore, Burlington, MA, USA). CdSeS/ZnS QDs (QD540) were from CytoDiagnostics (Burlington, ON, Canada) and CdSe/CdS/ZnS QDs (QD650, QD625, QD605, QD575) were synthesized by the decomposition of inorganic precursors in organic solvents during hot injection.^{141,142}

2.2 Microfluidic chip fabrication

A microfluidic chip mold was designed on AutoCAD 2018 (AutoDesk, San Rafael, CA, USA) with a channel dimension of 28.8 mm × 3 mm × 0.1 mm (length × width × height). (see **Figure**

2.1) First-generation molds were printed out with a Miicraft⁺ 3D printer (MiiCraft & Creative CADworks, Toronto, Ontario, CA) and clear microfluidics BV007A resin (Young Optics Inc., Taiwan). The channel width was set as the maximum dimension to get a full view of the channel under the smartphone camera with the magnification lens, which allows for a higher flux of cells in the channel. The height was set based on the minimum z-resolution of the 3D printer. With a lower channel height, cells tended to flow within the focal plane, which was beneficial for video analysis. After the mold was printed, it was rinsed with isopropanol (IPA) to remove excess resin, dried with compressed air, and exposed to UV light for 4 h for curing and further strengthening. The mold was then washed with a series of alcohols (ethanol, methanol, and IPA in order), followed by a heating process at 70 °C in oven for 4 h to remove any residual resin on the mold surface that might cause incomplete curing of the PDMS.

Second generation molds for microfluidics chips were printed with a Miicraft 50 3D printer (MiiCraft & Creative CADworks, Toronto, Ontario, CA) and resin specifically designed for use with PDMS soft lithography (Master mold resin, MiiCraft, Toronto, Ontario, CA) . This resin does not require post-printing heating of the mold.

For both generations of mold, the surface was activated using an air plasma cleaner at its high RF level (18W, Harrick Plasma PDC-32G; Ithaca, NY, USA) for 2 min. The mold surface was reacted with trichloro(1H,1H,2H,2H-perfluorooctyl)silane (PFOTS) under vacuum in a desiccator for 30 min to create a hydrophobic surface. This post-treatment of the mold was important for satisfactory PDMS casting results.

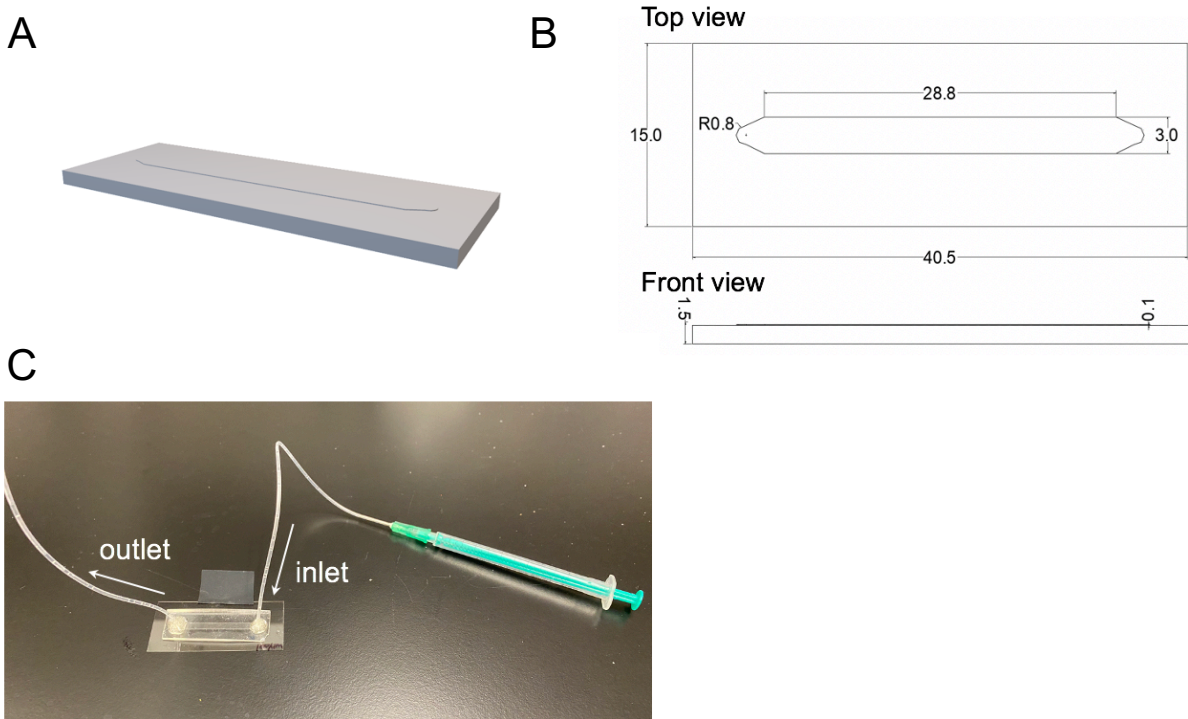


Figure 2.1 (A) 3D-rendering of the designed microfluidic chip mold. (B) Dimensions (mm) of the microfluidic chip mold. (C) Image of the final PDMS-on-glass microfluidic chip with inlet and outlet tubing attached.

Polydimethylsiloxane (PDMS) microfluidic chips were prepared by mixing the monomer and the curing agent together at a 10:1 ratio by mass, followed by degassing under vacuum until there were no bubbles. After the mixture turned from milky to clear, it was poured on the mold and cured overnight in an oven at 70 °C. The PDMS chip was then peeled from the mold and cut to the desired size. Two holes with a radius of ~0.8 mm were created with a steel punch to opposite ends of the channel to be the inlet and outlet. Glass coverslips and PDMS chips were put in the air plasma cleaner for 2 min at the high RF level and then adhered to each other immediately after the plasma oxidization. Polyethylene tubing (30 cm long, 0.86mm ID/1.27mm OD) was attached to the inlet and outlet holes of the PDMS chip and sealed with epoxy (Devcon 5 minute epoxy, Danvers, MA, USA). The other end of the inlet tubing was attached to a 1 mL syringe with a blunt needle (21G, 0.80 mm OD) for sample injection. (see **Figure 2.1 (C)**)

Before the first measurement with a cell suspension, the microfluidic chip was treated in the air plasma cleaner for 1 min. Next, 0.08% v/v pluronic F127 (aq) was then flowed through the channel at a speed of 10 $\mu\text{L}/\text{min}$ for 30 min followed by a 0.5% w/v BSA solution in 1X PBS(– –) buffer at the same flow rate for 30 min to make the surface hydrophilic and block cell adhesion during measurement. The PDMS treatment process was repeated for measurements longer than 24 h. The PDMS microfluidics chip can be reused until a large number of cells stick to the PDMS channel.

2.3 Ligand exchange of QDs with glutathione and histidine

Glutathione-coated QDs (GSH-QDs) were prepared by dissolving 80–100 mg glutathione (GSH) in 300 μL of methanolic tetramethylammonium hydroxide (TMAH; 25% w/w in methanol). Hydrophobic QDs ($\sim 81 \mu\text{M}$, 20 μL) from synthesis were diluted with 900 μL of chloroform in a 1.7 mL microcentrifuge tube. The GSH solution was then added to the hydrophobic QDs and mixed by vortex. The mixture was kept at room temperature in the dark for 8–12 h. Borate buffer (200 μL , 50 mM, pH 9.2) was then added to extract the GSH-QDs. After the organic and aqueous phases separated, the GSH-QDs were collected with the aqueous phase and the organic phase was discarded. Ethanol ($\sim 800 \mu\text{L}$) was then added to precipitate the aqueous GSH-QDs, which were pelleted by centrifugation at 4800 RCF for 10 min. The supernatant was discarded to remove free ligands and excess TMAH. The GSH-QDs were then redispersed in borate buffer (100 μL , 50 mM, pH 9.2). This ethanol precipitation process was repeated for another two times before the GSH-QDs were finally redispersed in borate buffer (200 μL , 50 mM, pH 9.2). The solution of GSH-QDs was stored at 4 °C until needed.

L-Histidine-coated QDs (His-QDs) were prepared through a similar procedure. Hydrophobic QDs ($\sim 81 \mu\text{M}$, 10 μL) from synthesis were diluted in chloroform (900 μL). L-histidine (0.645 mmol, 100 mg) was dissolved in TMAH (300 μL , 25% w/w in methanol) and added to the QD solution. The mixed sample was kept in the dark at room temperature for 1 h. Borate buffer (200 μL , 50 mM, pH 9.2) was then added to extract the His-QDs. After the organic and aqueous phases separated, the His-QDs were collected with the aqueous phase and the organic phase was discarded. His-QDs were collected via centrifugation at 4800 RCF for 10 min and redispersed in

borate buffer (100 μL , 50 mM, pH 9.2) and precipitated with ethanol ($\sim 800 \mu\text{L}$) to remove free ligands. After three wash cycles, the final pellet was redispersed in borate buffer (100 μL , 50 mM, pH 9.2) and stored at 4 $^{\circ}\text{C}$ until needed. QDs were modified with weak-binding histidine ligands in order to transfer hydrophobic QDs to water for subsequent coating with dextran ligands (see **Section 2.5**).

2.4 Preparation of $\text{SiO}_2@QD$ self-assemblies

$\text{SiO}_2@QD$ self-assemblies were prepared using a previously published method.¹⁴³ In brief, SiO_2 nanoparticles (SiO_2 NPs) were synthesized with a modified Stöber method and then functionalized with triethoxy-3-(2-imidazolin-1-yl)propylsilane (IPS). SiO_2 NPs in ethanol (100 μL) were mixed with IPS (10 μL , 50% v/v IPS in ethanol) and NH_3OH (10 μL , aq, 28-30 w/w %) at room temperature on a shaker for 2.5 h. $\text{SiO}_2@IPS$ were collected via centrifugation at 8400 RCF for 10 min and redispersed in borate buffer (100 μL , 50 mM, pH 8.5) after three cycles of precipitation and redispersion.

$\text{SiO}_2@IPS$ (50 μL) were then mixed with GSH-QDs (12 μL , $\sim 3 \mu\text{M}$) for 1 h at room temperature in the dark. GSH-QDs bind to the IPS-modified SiO_2 NPs through a combination of electrostatic interactions between imidazolium groups and the anionic GSH ligands on QDs, and coordinate binding between imidazoline groups and Zn on the ZnS shell of QDs. GSH-QDs, instead of His-QDs, were used because of the greater stability. $\text{SiO}_2@QD$ self-assemblies were then collected via centrifugation at 10 000 RCF for 10 min, followed by three cycles of centrifugation and redispersion in borate buffer (100 μL , 50 mM, pH 8.5).

2.5 Preparation of dextran-coated QDs and $\text{SiO}_2@QD\text{-Dex}$ and $\text{SiO}_2@QD\text{-CM-Dex}$

(3-Aminopropyl)-imidazole (API)-modified dextran was used to coat both single QD625 and $\text{SiO}_2@QD625$ for cell labeling.

Dextran (0.50 g, 9–11 kDa, *Leuconostoc mesenteroides*) was dissolved in 20 mL of deionized water in a 40 mL glass vial. NaIO₄ (3.1 mL, 0.1 M in deionized water) was added to the dextran solution. The mixture was covered with aluminum foil and stirred overnight at 4 °C in the dark. The samples were then purified by dialysis against 1.0 L of deionized water using 3.5 kDa-MWCO dialysis tubing for two days with three water changes. The purified sample was freeze-dried, and the final product was a fluffy-white solid (Ox-Dex). The Ox-Dex (0.1 g) was dissolved in 2 mL of deionized water in a 20 mL glass vial. API (0.25 mL, 51 mg/mL in deionized water) was added and the reaction was mixed overnight at room temperature. An aliquot of NaCNBH₃ (0.25 mL, 51 mg/mL) was added to the solution and left to mix overnight at room temperature. The sample was then pipetted into ethanol/hexane (95/5% v/v) solution to induce precipitation and pelleted via centrifugation at 13 000 RCF for 5 min. The supernatant was discarded, and the pellet was re-dissolved in 2 mL deionized water. The precipitation process in ethanol/hexane (95/5% v/v) was repeated and the final product (API-Dex) was dried under reduced pressure.

An analogous procedure was used for preparing API-modified carboxymethyl dextran (CM-Dex, 9–11 kDa). Substitution of dextran with CM-Dex was to enable downstream conjugation with antibodies via carbodiimide chemistry.

For API-Dex-coated single QDs, 15 mg of API-Dex was dissolved in carbonate buffer (250 μL, 100 mM, pH 9.3). His-QD625 (20 μL) was added to the solution and mixed via vortex. This solution was incubated at 60 °C for 3 h in the dark. Dextran-coated QD625 (Dex-QD625) were purified via three rounds of centrifugation with a 30 kDa-cutoff spin filter at 12 000 RCF for 7 min, washing with 200 μL carbonate buffer and with redispersion in carbonate buffer (300 μL, 100 mM, pH 9.3).

For SiO₂@(QD-Dex) assemblies, the initial SiO₂@QD assemblies (50 μL, ~0.35 nM) were mixed with API-Dex (12.5 μL, 28.5 mg/mL) for 1 h at 60 °C in the dark. SiO₂@(QD-Dex) were collected via centrifugation at 14 000 RCF for 10 min, washed with 50 μL of borate buffer three times, and finally dispersed in borate buffer (50 μL, pH 8.5, 50 mM).

SiO₂@(QD-CM-Dex) were prepared using same procedure except substitution API-Dex with API-CM-Dex.

2.6 Immunolabeling of fixed SK-BR3, MDA-MB-231, MCF-7 and A549 cells

2.6.1 PBS buffer

1X PBS buffer (– –) was from Gibco Life Technologies. The composition of this buffer was pH 7.4, 1.05 mM KH₂PO₄, 155 mM NaCl, 2.97 mM Na₂HPO₄·7H₂O without calcium and magnesium ions. Easy Sep buffer was the above PBS buffer supplemented with 2% v/v fetal bovine serum (Sigma Aldrich) and 1 mM EDTA (Fisher Scientific).

2.6.2 Cell culture

Human breast cancer SK-BR-3 cells and human lung cancer A549 cells were incubated in culture medium in a humidified incubator at 37 °C with 95% air/5% CO₂. The culture media was prepared by adding 10% v/v fetal bovine serum and 1X penicillin/streptomycin antibiotic and antimycotic (ThermoFisher) into McCoy's 5A medium (GE Healthcare, Chicago, IL). Cells were cultured in T25-flask first and the culture media was changed with fresh media every 2–3 days to grow cells to confluency. Cells were then passaged to T75 flasks to a desired amount.

Human breast cancer MCF-7 and MDA-MB-231 cells were incubated in culture medium in a humidified incubator at 37 °C with 95% air/5% CO₂. The culture media was prepared by adding 10% v/v fetal bovine serum and 1X penicillin/streptomycin antibiotic and antimycotic into Dulbecco's Modified Eagle Medium (DMEM).

2.6.3 Cell fixation

Paraformaldehyde-fixed cells were prepared by first trypsinizing the cells to detach them from the culture flask, collecting the culture media, and centrifuging it in a 15 mL centrifuge tube at 55 RCF

for 5 min to obtain a pellet of cells. The cells were redispersed in 2 mL PBS buffer (– –, 1X, pH 7.4) and then 2 mL of 4% w/v paraformaldehyde in PBS were added to the solution and incubated for 10 min. Fixed cells were pelleted via centrifugation at 55 RCF for 5 min. The cells were redispersed in 1X PBS buffer and the final cell concentration was obtained using a Countess II automated cell counter (Invitrogen).

Ethanol-fixed cells were prepared with a similar protocol. Ethanol in a 15 mL centrifuge tube was first put in dry ice for 30 min. Cultured SK-BR3 cells were trypsinized and collected as a pellet as described above. The pellet was then resuspended in 2 mL of 1X PBS buffer (– –). Cell solution (2 mL) was then added to 8 mL of dry-ice-cold ethanol and incubated at –20°C for 10 min. Fixed cells were centrifuged at 55 RCF for 5 min. The supernatant was discarded and the pellet was resuspended in 2 mL of 1X PBS buffer (– –). The cell concentration of the final solution was obtained using the automated cell counter (Invitrogen).

2.6.4 Pre-formation of Tetrameric Antibody Complexes (TACs)

Pre-formed TACs were prepared based on the manufacturer's protocol for the Do-It-Yourself Positive Selection Kit II (STEMCELL Technologies). The desired antibody (15 µg) was mixed with 100 µL of Component A and then 100 µL of Component B in order. The mixed sample was then incubated overnight at 37 °C and topped up to 1 mL with 1X PBS buffer and stored at 4 °C for near-future use.

2.6.5 Labeling of fixed SK-BR3 cells with Dex-QDs and SiO₂@QD-Dex via TACs

Fixed SK-BR3 cells (50 µL) were pipetted into two separate 1.7 mL microcentrifuge tubes, followed by 5 µL of pre-formed TAC complexes with anti-HER2 antibody (81 nM). The solution was mixed and incubated in the dark for 15 min. QD625-Dex (15 µL) and SiO₂@(QD625-Dex) (10 µL) were added separately to one of the two tubes and incubated in the dark for another 15 min. The labeled cells were collected and washed three times with PBS buffer (50 µL, 1X, – –, pH 7.4)

via centrifugation at 55 RCF for 5 min. The final cell pellet was redispersed in PBS buffer (50 μ L, 1X, --, pH 7.4).

An analogous procedure was used for immunolabelling of other cancer cell lines and for multi-color cellular immunolabeling, but with different pre-formed TACs or SiO₂@(QD-Dex) assemblies.

2.6.6 Preparation of SiO₂@(QD-CM-Dex)-antibody conjugates via EDC coupling

Antibodies were covalently linked to SiO₂@(QD-CM-Dex) through activation of the carboxy groups of CM-dex with 1-ethyl-3-(3-dimethylaminopropyl) carbodiimide (EDC) and *N*-hydroxysuccinimide (NHS). The buffer for this reaction was 4-(2-hydroxyethyl)piperazine-1-ethanesulfonic acid (HEPES, pH 7.05). Since EDC crosslinking is most efficient in acidic conditions, excess EDC and NHS were used to compensate for the lower efficiency in neutral pH conditions.

Synthesized SiO₂@(QD-CM-Dex) (5 μ L, ~3 nM) was mixed with 155 μ L of HEPES buffer. Freshly prepared EDC and NHS solution (each 10 mg/mL, 10 μ L and 12 μ L, respectively) was added to the solution simultaneously, followed by 10 μ L of anti-HER2 antibody (1.08 μ M). The solution was placed on a shaker for 1 h at room temperature in the dark. SiO₂@(QD-CM-Dex)-(anti-HER2) conjugates were then collected by centrifugation at 10 000 RCF for 5 min, followed by three washes with 200 μ L of 0.5% w/v BSA in 1X PBS buffer. The conjugates were then redispersed in 20 μ L of 0.05% w/v BSA in 1X PBS buffer and stored at 4 °C for further use.

A procedure similar to the above was used for preparation of SiO₂@(QD-CM-Dex)-antibody conjugates with anti-MUC1 antibody (0.5 mg/mL), anti-CD44 antibody (0.5 mg/mL), and anti-ER antibody (1mg/mL). Synthesized SiO₂@(QD-CM-Dex) (5 μ L, ~3 nM) was mixed with 155 μ L of HEPES buffer, and then 20 μ L of 0.01% v/v Tween 20 was added to the 1.7 mL microcentrifuge tube to minimize non-specific binding of the conjugates to the tube and loss of conjugates. The desired antibody (6 μ L for anti-MUC1 and anti-CD44 and 3 μ L for anti-ER) was added in this step

to form SiO₂@(QD-CM-Dex)-antibody conjugates targeting different antigens. The solution was placed on a shaker for 1 h at room temperature in the dark. SiO₂@(QD-CM-Dex)-antibody conjugates were then collected by centrifugation at 10 000 RCF for 5 min, followed by three washes with 200 μL 0.5% BSA (w/v) in 1X PBS buffer. The conjugates were eventually redispersed in 20 μL 0.05% BSA (w/v) in 1X PBS buffer and stored under 4 °C for further use.

2.6.7 Fixed SK-BR3, MDA-MB-231, A549, MCF-7 cells labeling with SiO₂@(QD-CM-Dex)-antibody conjugates

An aliquot of fixed SK-BR3 cells (50 μL, $\sim 1.1 \times 10^6$ cells/mL) was pelleted down via centrifugation at 55 RCF for 5 min and redispersed in 50 μL of Easy Sep buffer. SiO₂@(QD-CM-Dex)-(anti-HER2) bioconjugates (3 μL, prepared as per Section 2.6.6) were added to the cell solutions and incubated in the dark on a shaker at room temperature for 1 h. Labeled cells were pelleted down via centrifugation at 55 RCF for 5 min, followed by three washes with 200 μL of Easy Sep buffer, and finally redispersed in 50 μL of Easy Sep buffer. For MDA-MB-231, A549 and MCF-7 cells, an analogous procedure was used, but with SiO₂@(QD-CM-Dex)-(anti-MUC1), SiO₂@(QD-CM-Dex)-(anti-CD44), and SiO₂@(QD-CM-Dex)-(anti-ER), respectively.

2.7 Fluorescence microscopy

Cell images were acquired with an IX83 inverted epifluorescence microscope. This microscope was equipped with an X-Cite 120XL metal-halide light source (Excelitas Technologies, Mississauga, ON, Canada), a white-LED transmitted light source, an Orca-Flash 4.0 V2 sCMOS camera (C11440; Hamamatsu Photonics, Hamamatsu, SZK, Japan), motorized filter wheels (Sutter Instruments, Novato, CA, USA), and MetaMorph/MetaFluor software (Molecular Devices, Sunnyvale, CA, USA). Images were analyzed with Image J software.

Table 2.1 Specific filters used for each experiment.

Labels	Ex. Filter ¹ (nm)	Em. Filter ² (nm)	Dichroic mirror ³ (nm)
SiO₂@QD650	405/20 BP	600 LP	T 590
SiO₂@QD625	405/20 BP	620/40 BP	T 590
SiO₂@QD605	405/20 BP	570 LP	T 565
SiO₂@QD575	405/20 BP	550 LP	T 510
SiO₂@QD540	405/20 BP	540/50 BP	T 425

¹ Excitation filters, BP = Bandpass filter, center wavelength/bandwidth.

² Emission filters, LP = Longpass filter, cutoff wavelength

³ T = transmission cut-on wavelength.

The emission spectra of the cells labeled with SiO₂@(QD-Dex) were acquired with a CCD spectrometer (Greenwave 16 VIS-50; StellarNet, Tampa, FL, USA) that was coupled to the trinocular head of the microscope via a fiber-optic cable. The spectra were obtained with SpectraWiz software (StellarNet). A 530 nm longpass filter was used to block the excitation light.

2.8 Cell counting assays

2.8.1 Counting non-specifically labeled cells with the smartphone-based flow cytometer

QDs with a strong net charge often nonspecifically bind to cell membranes and proteins. Ethanol-fixed SK-BR3 cells (200 μ L) were pipetted into a 1.7 mL microcentrifuge tube and 1 μ L of GSH-coated QDs (\sim 3 μ M) was added to the tube. The sample was mixed via pipette and then incubated in the dark for 20 min. The cells were centrifuged at 55 RCF for 5 min and washed with 200 μ L

of 1X PBS buffer (– –) three times to remove unbound QDs. The cell pellet was resuspended in 200 μL of fresh PBS buffer.

Test samples with concentrations ranging from 9×10^2 to 2×10^5 cells/mL were prepared in 1.7 mL microcentrifuge tubes by dilution with 1X PBS buffer (– –). Each of the test samples with a minimum volume of $\sim 100 \mu\text{L}$ was injected into the microfluidics chip and pushed by deionized water with a 1 mL polypropylene syringe (VWR, Mississauga, ON, CA) and imaged through the smartphone camera. The minimum volume was set to ensure adequate sample volume ($\sim 30 \mu\text{L}$) without air bubbles flow through the microfluidics chip. A syringe pump (KD Scientific, Holliston, MA, USA) was used to let the cell suspension pass through the microfluidics channel at a constant flow rate ($10 \mu\text{L}/\text{min}$) in order to capture each cell via video recording. Cell counts and fluorescence intensity were obtained by video analysis with a MATLAB cell counting algorithm described in the **Appendix A.1**.

Cell counts of same test samples were also measured by pipetting an aliquot ($10 \mu\text{L}$) into a chamber slide and using an automated cell counter (Countess II Cell Counter, Invitrogen). Counts from the automated cell counter were used for validation of results with the smartphone flow cytometer. For expected cell counts below the lower limit of the cell counter ($\sim 10^4$ cells/mL), validation cell counts were instead obtained with a research-grade microscope. An aliquot ($10 \mu\text{L}$) of cell solution was pipetted into a cell counting chamber slide and the whole area was imaged under $4\times$ objective, followed by particle analysis with Image J. After the image was imported to Image J, a threshold value was set for pixel intensity and then a *watershed* function was applied if there were cell aggregates. The numbers of labeled cells and other information (*e.g.* mean intensity) were obtained with *analyze particles* function, stipulating a minimum size of $125 \mu\text{m}^2$.

2.8.2 Counting SK-BR3 cells labeled with SiO₂@(QD625-Dex) without background

MDA-MB-231 cells

SK-BR3 cells, which overexpress the HER2 protein, were labeled with SiO₂@(QD625-Dex) using a bifunctional TAC with an anti-HER2 antibody.

Paraformaldehyde-fixed SK-BR3 cells (300 μ L, $\sim 10^6$ cells/mL) were pipetted into a 1.7 mL microcentrifuge tube and then mixed with 30 μ L of DAPI solution (~ 2.86 μ M in PBS buffer) and 30 μ L of pre-formed TAC complex (81 nM). The mixture was incubated in the dark for 15 min. SiO₂@(QD625-Dex) (30 μ L, ~ 0.3 nM) was then added to the solution and incubated in the dark for another 15 min. The cells were pelleted down via centrifugation at 55 RCF for 5 min, washed with Easy Sep buffer (300 μ L) and redispersed in 1X PBS buffer (300 μ L, --). An increasing number of SK-BR3 cells labeled with SiO₂@(QD625-Dex) was then pipetted from the stock solution to nine separate 1.7 mL microcentrifuge tubes and diluted up to 300 μ L with 1X PBS buffer (--). For cell solutions with a lower concentration (more than 300-fold dilution), 1 μ L of stock solution was diluted with desired amount of 1x PBS buffer (--). The test samples (~ 100 μ L for each run) were injected into the microfluidics chip and imaged with the smartphone-based flow cytometer. Smartphone videos (~ 3 min, ~ 30 μ L of cell suspension) were analyzed with the MATLAB algorithm (see **Appendix A.1**).

Cell counts of each test sample were also obtained with an automated cell counter (Countess II Cell Counter, Invitrogen) for validation. For expected cell counts below the lower limit of the cell counter ($\sim 10^4$ cells/mL), validation cell counts were instead obtained with a research-grade microscope. An aliquot (10 μ L) of cell solution was pipetted into a cell counting chamber slide and the whole area was imaged under 4 \times objective, followed by particle analysis with Image J.

2.8.3 Counting SK-BR3 cells labeled with SiO₂@(QD625-Dex) with background

MDA-MB-231 cells

SK-BR3 cells (300 μL , $\sim 1.1 \times 10^6$ cells/mL) and MDA-MB-231 cells (300 μL , 1.14×10^6 cells/mL) were redispersed in 100 μL of DAPI solution (~ 2.86 μM in PBS buffer) in two separate minicentrifuge tubes and incubated in the dark for 20 min. DAPI-stained cells were pelleted down at 55 RCF for 5 min and redispersed in 300 μL of Easy Sep buffer. Before preparation of test samples, DAPI-stained cells were filtered through a 40 μm cell strainer (STEMCELL technologies). A constant volume (50 μL , $\sim 50\text{k}$ cells) of MDA-MB-231 were pipetted from a stock solution of $\sim 1\,000\,000$ cells/mL for each sample. An increasing number of SK-BR3 cells were pipetted into separate tubes. ~ 555 , ~ 700 , ~ 1320 , ~ 1530 , ~ 3750 , ~ 6320 fixed SK-BR3 cells were pipetted from a stock solution of $\sim 234\,500$ cells/mL. ~ 8560 , $\sim 17\,125$, $\sim 25\,690$, $\sim 34\,250$, $\sim 51\,375$, $\sim 60\,000$ fixed SK-BR3 were pipetted from a stock solution of $\sim 342\,500$ cells/mL. Each of the test samples was diluted up to 300 μL with Easy Sep buffer.

Next, a spike of 0.5 μL pre-formed TAC complex (81 nM) was added to each tube of fixed cells and left in the dark for 15 min, followed by 1 μL of SiO₂@(QD625-Dex) composites (~ 3.3 nM). The solution was left in the dark for another 15 min and then washed three times with 300 μL Easy Sep buffer with centrifugation at 55 RCF for 5 mins to remove excess SiO₂@(QD625-Dex). Cell pellets were redispersed to 600 μL 1X PBS buffer (–). Different test samples (~ 200 μL for each run) were imaged with the smartphone-based flow cytometer and validated with Countess II cell counter (Invitrogen). For expected cell counts lower than the limit of the cell counter ($\sim 10^4$ cells/mL), cell counts obtained from the smartphone-based flow cytometer were validated with a research-grade microscope. Smartphone videos (~ 3 min, ~ 30 μL of cell suspension) were recorded and cell counts based on the two colors (red and blue) were obtained through the MATLAB algorithm described in detail in **Appendix A.2**.

2.9 Selective cell labeling and counting with SiO₂@(QD-CM-Dex)-antibody conjugates

To test for specific immunolabeling with covalent conjugation of anti-target antibody, an aliquot (50 μL , $\sim 1.1 \times 10^6$ cells/mL) of paraformaldehyde-fixed SK-BR3 cells (HER2+) and an aliquot

(50 μL , $\sim 1.14 \times 10^6$ cells/mL) of paraformaldehyde-fixed MCF-7 cells (HER2 $-$) were separately pelleted down and resuspended in 50 μL of buffer for immunolabeling with 3 μL of SiO₂@(QD-(anti-HER2) conjugate (~ 0.6 nM), followed by three washes with 50 μL Easy Sep buffer at 55 RCF for 5 min, and redispersed in 50 μL of Easy Sep buffer. An aliquot (7.5 μL) of immunolabeled cell suspension was dropped on a microscope glass slide and imaged under a microscope.

Next, aliquots (20 μL) of paraformaldehyde fixed A549 cells (CD44 $+$), paraformaldehyde fixed MDA-MB-231 cells (MUC1 $+$), and paraformaldehyde fixed SK-BR3 cells (HER2 $+$) were labeled separately with 1 μL of SiO₂@QD-antibody conjugate (SiO₂@(QD 605-CM-Dex)-(anti-MUC1), SiO₂@(QD650-CM-Dex)-(anti-CD44), and SiO₂@(QD540-CM-Dex)-(anti-HER2), respectively) in Easy Sep buffer for 1 h, followed by three washes with 50 μL Easy Sep buffer at 55 RCF for 5 min, and redispersed in 20 μL of Easy Sep buffer. An aliquot (7.5 μL) of labeled cell solution was dropped on a microscope glass slide and imaged under a microscope.

For selective cell counting via the smartphone video data, a linear support vector machine (SVM) model was trained for cell classification based on the red (R) and green (G) colour features. A linear SVM model is a supervised learning method and thus requires a training dataset. Single types of cells labeled with single colours were used for training the model, after which the trained model can classify what cells belong to which group when the labeling colour is not pre-determined (See **Appendix A.3**). Paraformaldehyde fixed SK-BR3 cells (50 μL , $\sim 1.1 \times 10^6$ cells/mL) and MDA-MB-231 cells (50 μL , 1.14×10^6 cells/mL) were incubated with aliquots of SiO₂@(QD540-CM-Dex)-(anti-HER2) (3 μL , ~ 0.6 nM) and SiO₂@(QD650-CM-Dex)-(anti-MUC1) (3 μL , ~ 1 nM) bioconjugates respectively in two separate 1.7 mL microcentrifuge tubes for 1 h in dark on a shaker at room temperature. Labeled cells were pelleted down via centrifugation at 55 RCF for 5 min, washed with 200 μL of Easy Sep buffer three times and redispersed in 200 μL PBS buffer. Paraformaldehyde-fixed SK-BR3 and MDA-MB-231 cell solutions, which were not labeled with SiO₂@QD, were prepared as a training sample for unlabeled cells. Final cell solutions were injected into the microfluidic chip and imaged on the smartphone-based flow cytometer.

Colour features extracted from the two samples of labeled cells above were used as the training dataset for the Linear SVM (RG) model, and colour features extracted from all three samples above were used as the training dataset for the Linear SVM (RGN) model. Next, a mixture of fixed SK-BR3 cells ($50 \mu\text{L}$, $\sim 1.1 \times 10^6$ cells/mL) and MDA-MB-231 cells ($50 \mu\text{L}$, 1.14×10^6 cells/mL) was prepared and incubated with aliquots of $\text{SiO}_2@(\text{QD540-CM-Dex})-(\text{anti-HER2})$ ($3 \mu\text{L}$, ~ 0.6 nM) and $\text{SiO}_2@(\text{QD650-CM-Dex})-(\text{anti-MUC1})$ ($3 \mu\text{L}$, ~ 1 nM) bioconjugates for 1 h in dark on a shaker at room temperature. Labeled cells were pelleted down via centrifugation at 55 RCF for 5 min, washed with $200 \mu\text{L}$ of Easy Sep buffer three times and redispersed in $200 \mu\text{L}$ PBS buffer. Cell suspensions was injected into the microfluidic chip, imaged on the smartphone-based flow cytometer, and colour features of the sample were extracted from the smartphone videos. Cell counts of different classified groups were obtained with two Linear SVM models (see **Appendix A.3**).

Next, paraformaldehyde-fixed SK-BR3 ($90 \mu\text{L}$, $\sim 132\ 000$ cells) were pipetted from a stock solution of $\sim 1\ 475\ 000$ cells/mL for each sample. An increasing number of MDA-MB-231 cells were pipetted into separate tubes. ~ 5100 , $\sim 25\ 500$, $\sim 51\ 000$, $\sim 102\ 000$, $\sim 153\ 000$ fixed MDA-MB-231 cells were pipetted from a stock solution of $\sim 1\ 020\ 000$ cells/mL. Test samples of mixed cells were prepared, labeled with aliquots of $\text{SiO}_2@(\text{QD540-CM-Dex})-(\text{anti-HER2})$ ($3 \mu\text{L}$ ~ 0.6 nM) and $\text{SiO}_2@(\text{QD650-CM-Dex})-(\text{anti-MUC1})$ ($3 \mu\text{L}$ ~ 1 nM), washed with $200 \mu\text{L}$ of Easy Sep buffer three times, and resuspended in $600 \mu\text{L}$ of PBS buffer.

The above samples were injected into the microfluidic chip in sequence from low cell concentration to high cell concentration and imaged on the smartphone-based flow cytometer. The microfluidic chip was flushed with deionized water (~ 1 mL) three times between two different samples. Smartphone videos (~ 2 - 3 min, ~ 20 - $30 \mu\text{L}$ of cell suspension) were recorded and cell counts in each classified group were obtained through the MATLAB algorithm described in detail in **Appendix A.3**. Expected cell counts of each test sample (mixture of SK-BR3 and MDA-MB-231 cells) were obtained with an automated cell counter (Countess II Cell Counter, Invitrogen). Since the cell counter cannot distinguish between the two cell lines in the mixed test samples, the total cell counts of each test sample obtained from the cell counter were multiplied with the ratio

of SK-BR3 and MDA-MB-231 cell stock solutions added. This calculation yielded the expected cell counts for the SK-BR3 and MDA-MB-231 cell lines in each test sample for validation of the results obtained with smartphone-based flow cytometer.

2.10 Classification of multiple breast cancer cell lines with SiO₂@QD-antibody conjugates

Aliquots (50 μ L) of paraformaldehyde fixed SKBR3 cells ($\sim 1.1 \times 10^6$ cells/mL), MDA-MB-231 cells ($\sim 1.14 \times 10^6$ cells/mL) and MCF-7 cells ($\sim 1.15 \times 10^6$ cells/mL) were pelleted down via centrifugation at 55 RCF for 5 min and resuspended in Easy Sep buffer (200 μ L) in three separate microcentrifuge tubes. The cell solutions were incubated in Easy Sep buffer for 1 h. A combination of SiO₂@(QD650-CM-Dex)-(anti-ER) (2 μ L), SiO₂@(QD575-CM-Dex)-(anti-MUC1) (3 μ L) and SiO₂@(QD540-CM-Dex)-(anti-HER2) (3 μ L) conjugates (as prepared in Section 2.6.6) was then added to the microcentrifuge tubes and incubated in dark on a shaker for another 1 h. The cell solutions were again pelleted down at 55 RCF for 5 min, washed with 200 μ L of Easy Sep buffer three times, and resuspended in 50 μ L of 1X PBS buffer for each sample. A control sample with only the three types of SiO₂@(QD-CM-Dex)-antibody conjugates (no cells) was also prepared, washed and pelleted down analogously as the test samples. The cell suspensions and control sample were imaged with the smartphone-based flow cytometer and the videos were analyzed with the MATLAB algorithm.

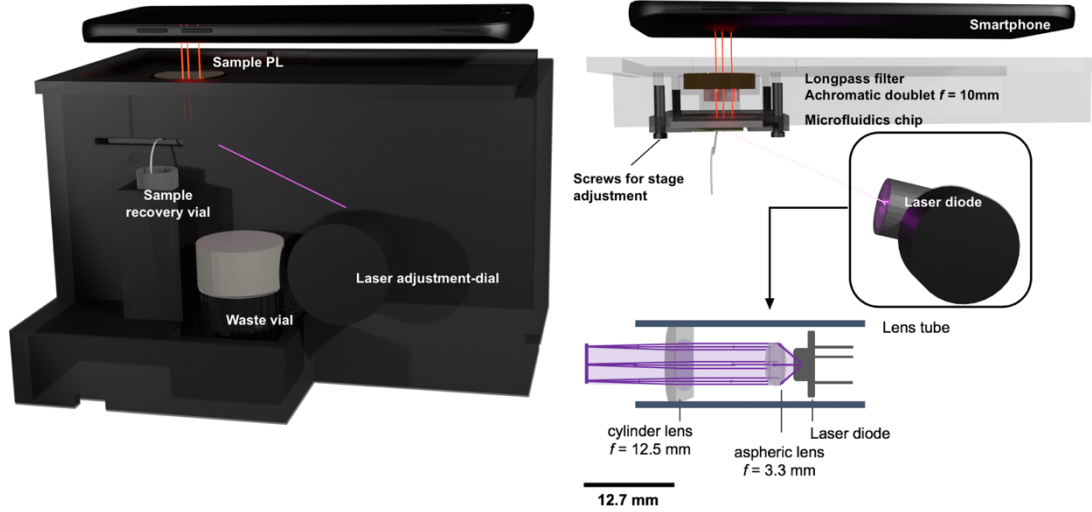
Chapter 3: Results and Discussion

3.1 Design of the smartphone-based flow cytometry setup

Figure 3.1 illustrates a 3D-printed imaging platform for flow cytometry, designed for a Samsung Galaxy S8 smartphone camera. The 3D-printed pieces (dark box, smartphone stage, sample holder, and laser diode mount) were designed with AutoCAD 2018 AutoDesk Student 3-D drafting software (AutoDesk, San Rafael, CA) and printed out using an Ender-3 Pro 3D printer (Creality, Shenzhen, China) with black polylactic acid (PLA) filament. The smartphone stage was a lid for the dark box and held the optical components: a 450 nm-longpass filter (Thorlabs, Newton, NJ, USA) to block excitation light and an achromatic doublet (10 mm focal length, 6 mm diameter; Thorlabs) to magnify the image. The sample holder aligned the channel of a PDMS-on-glass microfluidics chip with the magnified field of view of the smartphone camera. In order to focus on the objects passing through the microfluidic channel, the distance between the achromatic doublet and the microfluidics chip was adjustable via metal screws at all four corners of the sample holder. The lateral resolution of the smartphone-based imaging platform was $\sim 2.8 \mu\text{m}$ per pixel. A laser diode (D405-20; 405 nm, 20 mW, 5 V, 75 mA, Radial, Can, 3 Lead, 5.6 mm, TO-18) was the excitation source (US-Lasers, Baldwin Park, CA, USA). The laser diode was collimated by an aspheric lens ($f=3.3$ mm) then focused to a line (~ 2 mm) by a cylindrical lens ($f=12.5$ mm). The laser can be rotated to different angles of incidence via an adjustment rod and knob.

For the measurement, the test sample of cell solutions was injected into the microfluidic chip with a syringe pump and either collected via a sample recovery vial or discarded to a waste vial. Typically, a 2–3 min smartphone video (.mp4) was recorded using the pro mode of the built-in camera app (1/30s, 4000K, ISO100 or adjusted value based on the sample brightness) and then transferred to a computer for further data-analysis with a MATLAB cell counting algorithm (see **Appendix A.1**).

A



B

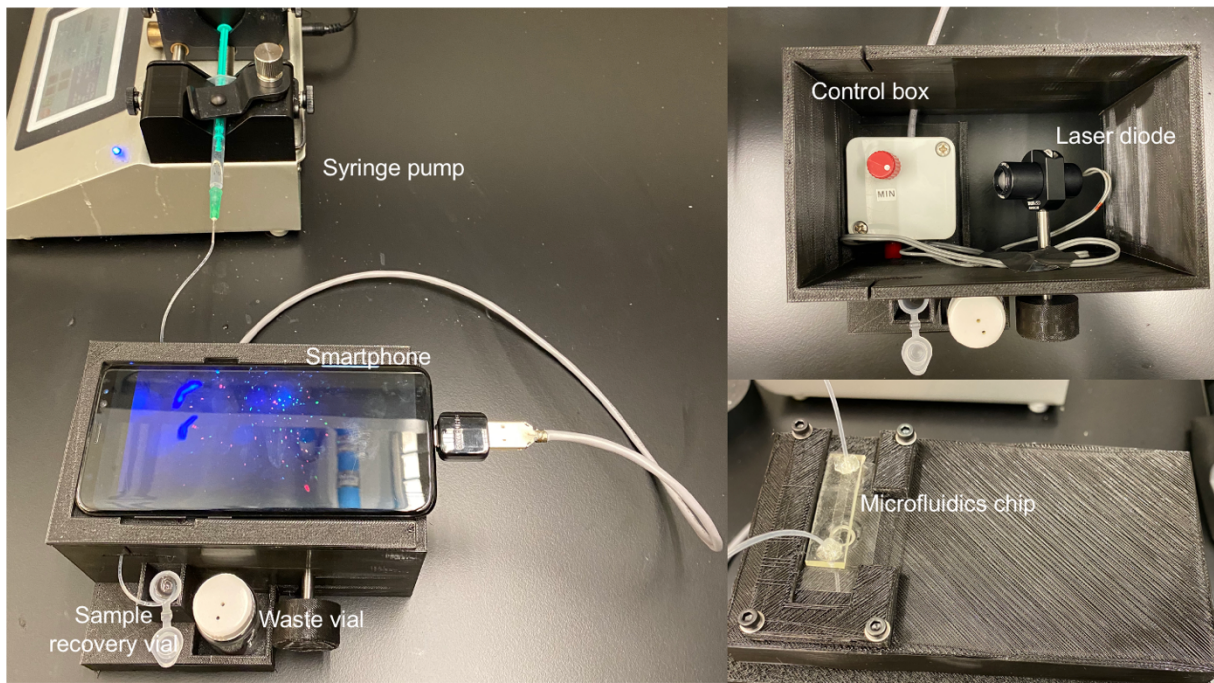


Figure 3.1 3D-printed smartphone-based flow cytometer (A) Illustration of the device with the laser diode optics. The laser light was collimated with an aspheric lens ($f = 3.3$ mm) and then focused to a line with a cylinder lens ($f = 12.5$ mm). An achromatic doublet ($f = 10$ mm) was used as a magnification lens for cell imaging. (B) Photographs of the device. The sample holder holding the microfluidics chip is attached to the black box lid with four screws. The laser diode can be adjusted with the dial for optimum illumination angle. The waste vial collects the wash solutions and can be replaced with a clean sample vial to re-collect test sample if needed.

3.2 Validation with non-specifically labeled cells

Dilutions ($\sim 200 \mu\text{L}$) of fixed SK-BR3 cells nonspecifically labeled with QD625-GSHs with a concentration between 9×10^2 to 2×10^5 cells/mL were injected to the microfluidic chip using syringe pump and a 1 mL plastic syringe. The cell sample volume was then pushed through the microfluidic channel by deionized water with a constant flow rate of $10 \mu\text{L}/\text{min}$. For each sample, ~ 3 min of video ($\sim 30 \mu\text{L}$ of cell solution) was recorded and analyzed through the MATLAB cell counting algorithm (see **Appendix A.1**) to obtain absolute cell counts that were converted into to a concentration in units of cells/mL. Any cell non-specifically bound to the microfluidic channel will be treated as background and not affect the cell counting results since the MATLAB algorithm only tracks moving objects. If too many cells were observed stick to the microfluidic channel, then a new PDMS microfluidics chip was used. Aliquots ($10 \mu\text{L}$) of the same samples were counted using the standard procedure on a commercial automated cell counter to generate an expected cell count for the correlation plot in **Figure 3.2 (C)**. For expected cell counts lower than the limit of the cell counter ($\sim 10^4$ cells/mL), the whole chamber slide was imaged under $4\times$ objective of a research-grade microscope and the images were analyzed with ImageJ to obtain cell counts. Representative image sequences of a smartphone video are shown in **Figure 3.2 (A)**. Representative smartphone images are shown in **Figure 3.2 (B)**.

3.3 TAC-mediated cell labeling with QDs and SiO₂@QD assemblies

QD625-GSH and SiO₂@QD625 composites were prepared and coated with API-dextran. Paraformaldehyde-fixed SK-BR3 cells were labeled with QD625-Dex and SiO₂@(QD625-Dex) with TAC conjugates. The bifunctional TAC conjugate was one part anti-HER2 antibody to target SK-BR3 cells and was one part anti-dextran antibody to target QD-Dex and SiO₂@(QD-Dex). (see **Figure 3.3**) Fixed SK-BR3 cells were incubated with TAC for 15 min and then SiO₂@(QD625-Dex) or QD625-Dex for another 15 min. Labeled cells were collected via centrifugation, washed, and resuspended in buffer. Labeled cells were imaged under a research-grade microscope and their relative brightnesses were compared (see **Figure 3.4**). SiO₂@(QD-Dex) was used for further smartphone-based cell-counting assays due to its almost 18-fold higher signal-to-background ratio (SBR) and 6-fold higher signal-to-noise ratio (SNR) compared to QD-Dex. SBR and SNR were calculated using equation 3.1 and equation 3.2, respectively, where I_{cell} is PL intensity of the labeled cell, I_{bg} is PL intensity of the background and $\sigma_{(I_{bg})}$ represents standard deviation of the background signal.

$$SBR = \frac{I_{cell} - I_{bg}}{I_{bg}} \quad (\text{Equation 3.1})$$

$$SNR = \frac{I_{cell} - I_{bg}}{\sigma_{(I_{bg})}} \quad (\text{Equation 3.2})$$

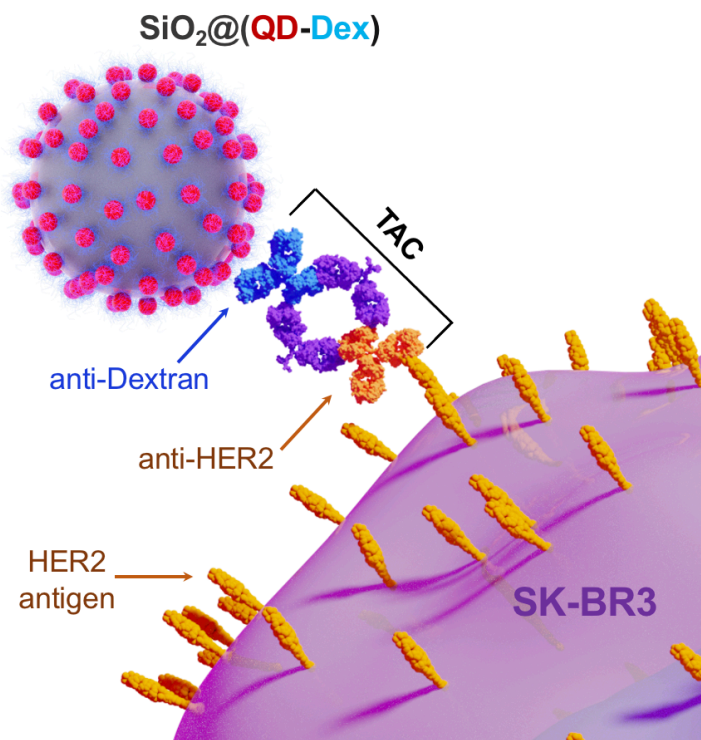


Figure 3.3 Schematic illustration of TAC-mediated immunolabeling to HER2 antigens on SK-BR3 cells with $\text{SiO}_2@(\text{QD-Dex})$.

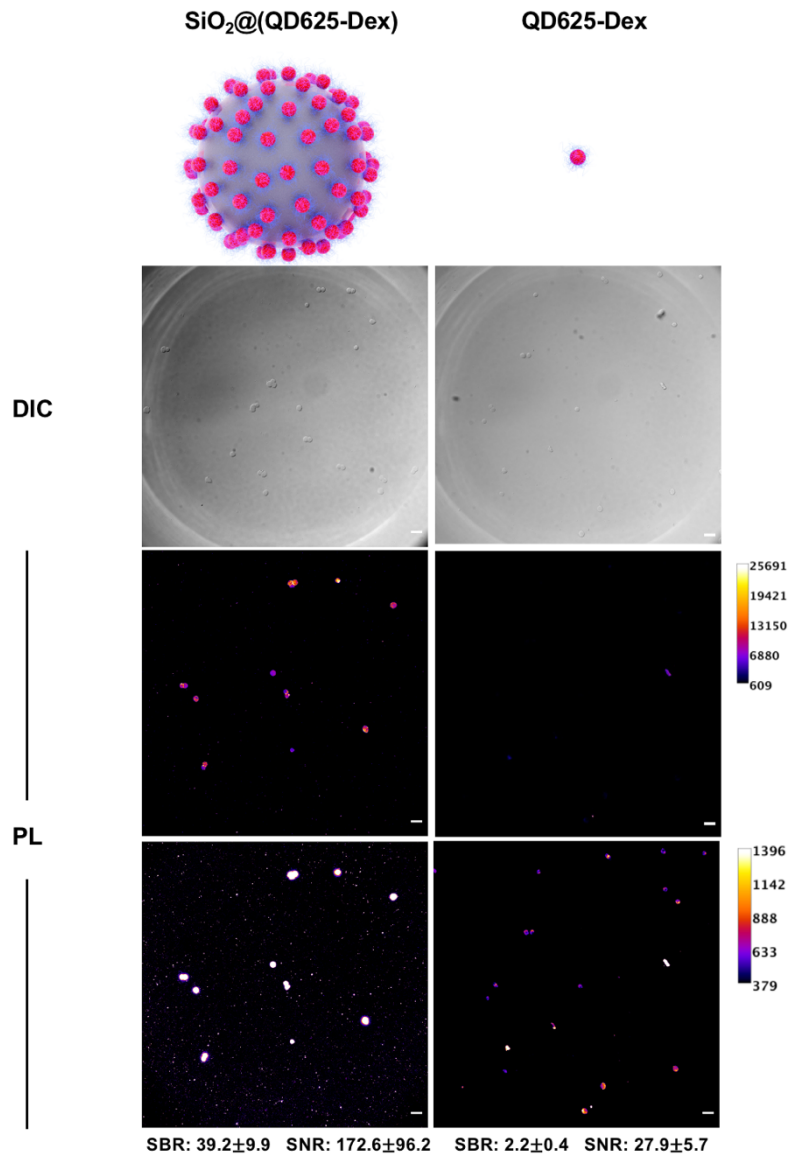


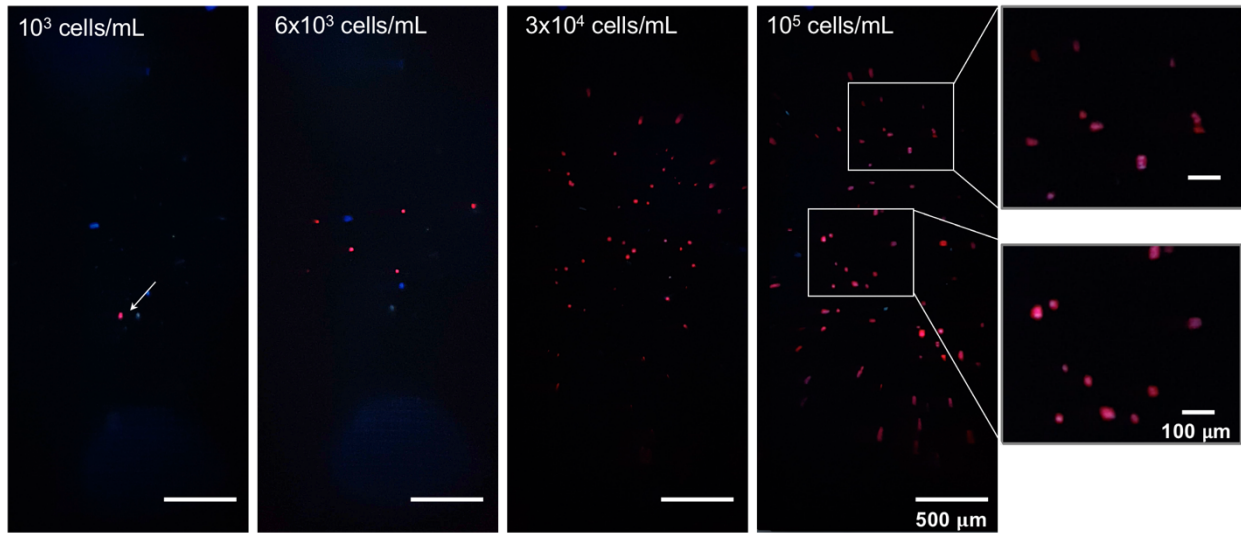
Figure 3.4 Microscope imaging (10× magnification) of fixed cells labeled with $\text{SiO}_2@(\text{QD625-Dex})$ (left) and QD625-Dex (right). Scale Bar: 50um. Images were acquired under the same microscope settings. The middle row shows pseudo-coloured PL images with contrast and brightness optimized for $\text{SiO}_2@(\text{QD625-Dex})$. The bottom row shows the same pseudo-coloured PL images but with contrast and brightness optimized for QD625-Dex .

3.4 Cell counting assays

3.4.1 Counting SK-BR3 cells immunolabeled with SiO₂@(QD625-Dex)

To demonstrate counting of immunolabeled cells, paraformaldehyde-fixed SK-BR3 cells labeled with SiO₂@QD625 assemblies and anti-HER2 TACs were tested with the smartphone-based flow cytometer. Stock solutions were stained with DAPI first, labeled with SiO₂@QD assemblies, and then diluted to different concentrations (~10, ~20, ~70, ~150, ~250, ~700, ~1.0k, ~2.4k, ~6.3k, ~24k, ~34k, ~150k cells/mL) with buffer. For each test sample, an average cell count was obtained from three runs with the smartphone-based flow cytometer. Representative images are shown in **Figure 3.5 (A)**. Cells labeled with SiO₂@QD625 appeared as red objects in the smartphone videos and unlabeled or poorly labeled cells appeared as blue objects because of the DAPI staining. The cell counting algorithm distinguished labeled cells (red objects) from unlabeled or poorly labeled cells (blue objects) and provided cell counts based on the red and blue colour. A simple area correction method was used to prevent underestimation of cell counts because of cell aggregates (see **Appendix A.2**). In **Figure 3.5 (B)**, the blue line with a slope of 0.90 is the total cell counts, inclusive of both labeled and unlabeled cells, whereas the red line with a slope of 0.86 represents cells successfully labeled with SiO₂@QD625. The two lines nearly overlapped, indicating the high efficiency of TAC labeling, with a paired t-test indicating a significance level $\alpha \leq 0.05$. The lower limit of the cell counts was obtained with a 3-4 min video (flow rate 50 $\mu\text{L}/\text{min}$) and, in general, can be reduced by increasing the sample volume and extending the measurement time. The capture efficiency of TAC labeled SK-BR3 cells from the smartphone-based flow cytometer is around 86%, consistent with other studies.³⁶ The capture efficiency was < 100% because some of the cells were not labeled successfully with TAC (visible as blue objects because of DAPI staining), and, presumably, because some of the cells were not successfully transported to the microfluidic channel and camera field of view.

A



B

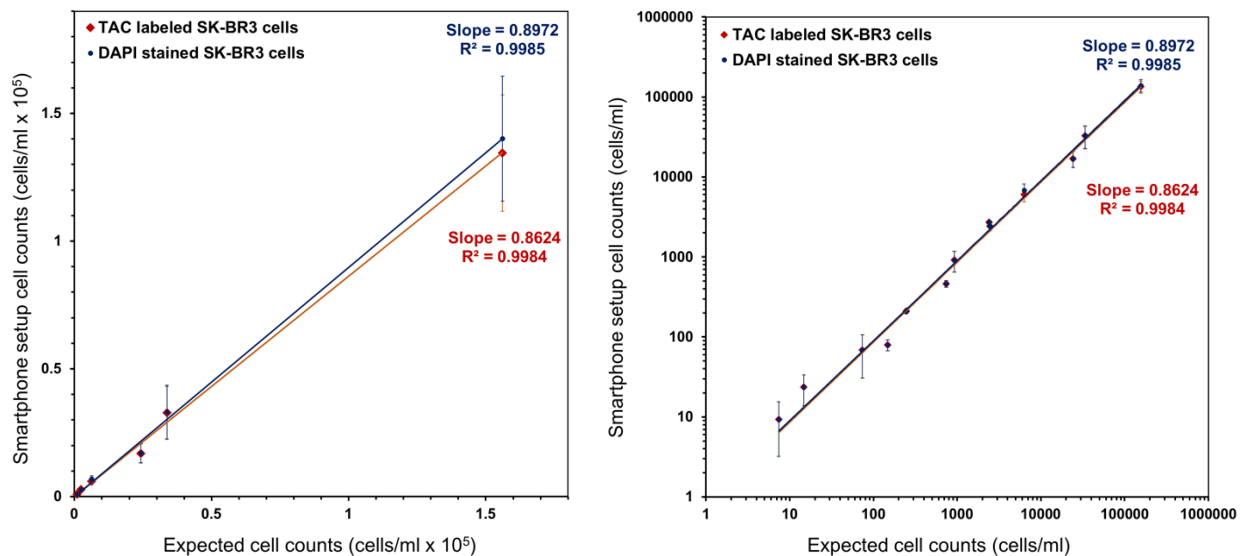
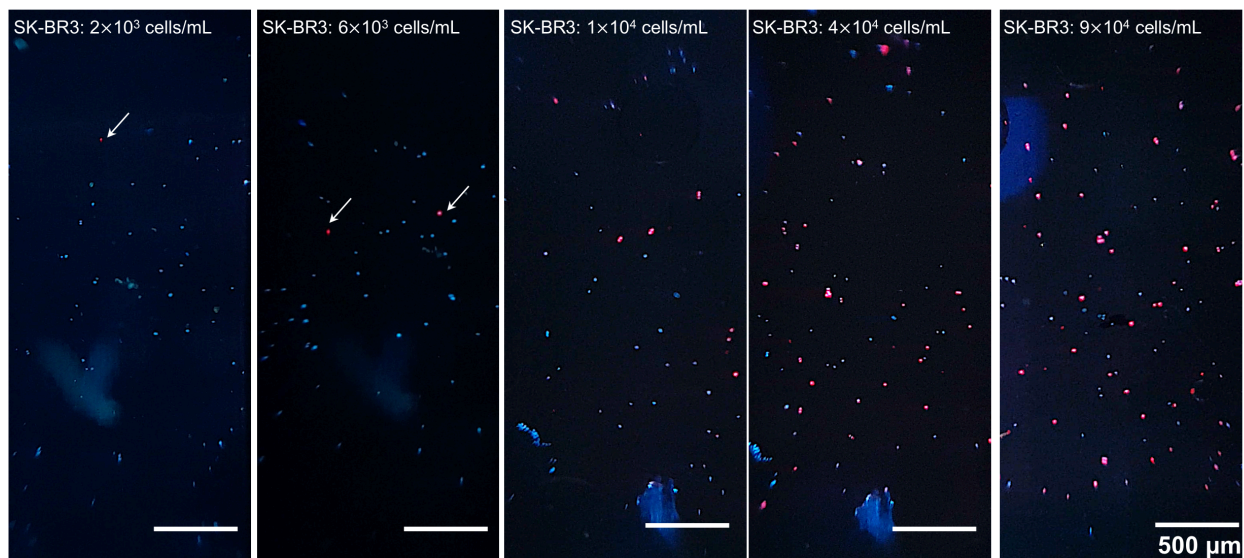


Figure 3.5 (A) Representative images taken from smartphone videos of TAC-labeled and DAPI-stained fixed SK-BR3 cells of different concentrations. The flow direction was from right to left. **(B)** Comparison of calibration curves (left: linear scales, right: log scales) for TAC-labeled (red) and DAPI stained (blue) fixed SK-BR3 cell counts from the smartphone setup, where the expected counts were from a commercial automated cell counter (TAC-labeled SK-BR3 cells: slope 0.86, correlation coefficient $R^2 > 0.99$; DAPI-stained SK-BR3 cells: slope 0.90, correlation coefficient $R^2 > 0.99$).

3.4.2 Counting SK-BR3 cells immunolabeled with SiO₂@(QD625-Dex) against a constant background of MDA-MB-231 cells

To confirm the specific labeling of SK-BR3 cells, a HER2-negative cell line, MDA-MB-231, was added into samples as a background cell type. Separate stock solutions of paraformaldehyde-fixed SK-BR3 cells and MDA-MB-231 cells were stained with DAPI first, then pipetted through a 40 μm cell strainer into two separate tubes. Test samples with various numbers of SK-BR3 cells and a constant number of MDA-MB-231 cells ($\sim 50\text{k}$ cells) were prepared, mixed with TAC and SiO₂@(QD625-Dex), and washed with Easy Sep buffer using the method mentioned in Section 2.8.3. The data is shown in **Figure 3.6**, the slope (without the outlier at $\sim 8.5 \times 10^4$ cells/mL (standardized residual $|r| > 3$)) is 0.87 with a correlation efficient of 0.99, consistent with the data in **Figure 3.5** without background cells. (with a paired t-test indicating a significance level $\alpha \leq 0.05$)

A



B

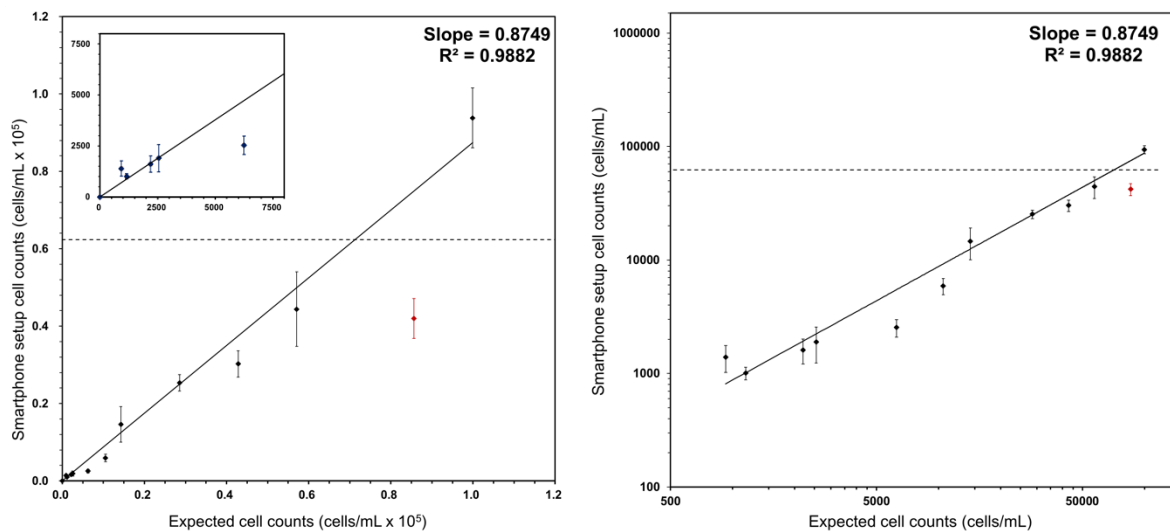


Figure 3.6 (A) Representative images taken from smartphone videos of an increasing number of TAC-labeled and DAPI-stained fixed SK-BR3 cells with background DAPI-stained MDA-MB-231 cells. The flow direction was from right to left. **(B)** Calibration curve (left: linear scales, right: log scales) of TAC-labeled SK-BR3 cells with a constant number of background MDA-MB-231 cells (represented by the dashed horizontal line). Inset image is the calibration curve of lower cell concentration from 0 to 8 000 cells/mL (slope 0.8749, correlation coefficient $R^2 \sim 0.99$).

3.5 Evaluating multiple colours of SiO₂@QD-Dex for immunolabeling

3.5.1 Characterization of various colours of SiO₂@QD

In addition to the red-emitting QD650 used in the previous sections, orange-emitting (QD605), yellow-emitting (QD575), and green-emitting (QD540) QDs were also of interest for immunolabeling SK-BR3 cells via anti-HER2 TACs. SiO₂@QD and SiO₂@QD-Dex assemblies were therefore prepared with these colours of QD following our previously published protocol.¹⁴³

Table 3.1 summarizes the size and concentration data from nanoparticle tracking analysis (NTA) on these batches of SiO₂@QD. **Figure 3.7** shows the normalized extinction spectra and normalized PL excitation and emission spectra of the various SiO₂@QD.

Table 3.1 Mode hydrodynamic diameters (\pm standard deviation) of SiO₂@QD and SiO₂@(Dex-QD) using scattering mode and fluorescence mode.

Material	Scatter mode		Fluorescence mode	
	Diameter (nm)	Particles (mL ⁻¹)	Diameter (nm)	Particles (mL ⁻¹)
SiO ₂ @QD625	97 \pm 48	(3.46 \pm 0.1) x 10 ¹²	98 \pm 43	(2.08 \pm 0.1) x 10 ¹²
SiO ₂ @(QD625-Dex)	92 \pm 39	(4.08 \pm 0.1) x 10 ¹²	97 \pm 41	(3.18 \pm 0.1) x 10 ¹²
SiO ₂ @QD605	93 \pm 68	(5.28 \pm 0.2) x 10 ¹¹	135 \pm 123	(3.38 \pm 0.2) x 10 ¹¹
SiO ₂ @(QD605-Dex)	117 \pm 44	(1.83 \pm 0.1) x 10 ¹²	104 \pm 52	(1.62 \pm 0.4) x 10 ¹²
SiO ₂ @QD575	120 \pm 52	(3.31 \pm 0.2) x 10 ¹²	117 \pm 85	(2.20 \pm 0.1) x 10 ¹²
SiO ₂ @(QD575-Dex)	85 \pm 31	(4.28 \pm 0.2) x 10 ¹²	81 \pm 41	(3.80 \pm 0.2) x 10 ¹²
SiO ₂ @QD540	116 \pm 52	(1.13 \pm 0.1) x 10 ¹²	155 \pm 75	(2.08 \pm 0.1) x 10 ¹¹
SiO ₂ @(QD540-Dex)	89 \pm 37	(1.60 \pm 0.1) x 10 ¹²	95 \pm 51	(6.76 \pm 0.3) x 10 ¹¹

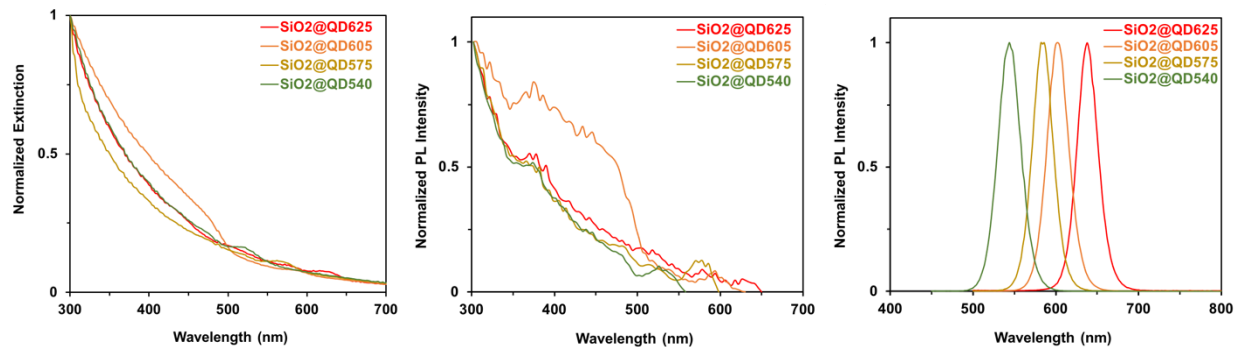


Figure 3.7 PL characterization of SiO₂@QD625, SiO₂@QD605, SiO₂@QD575, SiO₂@QD540. Left: Normalized extinction spectra, showing both a scattering component from the SiO₂ nanoparticle and absorption peaks from the QDs. Middle: Normalized PL excitation spectra. Right: Normalized emission spectra.

3.5.2 Immunolabeling of HER2 on SK-BR3 cells

Initial immunolabeling with the various colours of SiO₂@(QD625-Dex) was done with a protocol similar to that for SiO₂@(QD625-Dex). Aliquots of paraformaldehyde-fixed SK-BR3 cells were *separately* labeled with SiO₂@(QD625-Dex), SiO₂@(QD605-Dex), SiO₂@(QD575-Dex) and SiO₂@(QD540-Dex), all with anti-HER2 TACs. Aliquots of labeled cells (7.5 μL) were dispensed on a glass microscope slide, covered with a coverslip, and imaged under a research-grade microscope, as shown in **Figure 3.8 (A)**. Signal-to-background ratios of the smartphone-based FC were obtained through analysis of a RAW image captured during the video recording at same settings as shown in **Figure 3.8 (B)**. The background intensity can be significantly reduced by adding more wash cycles after cell incubation.

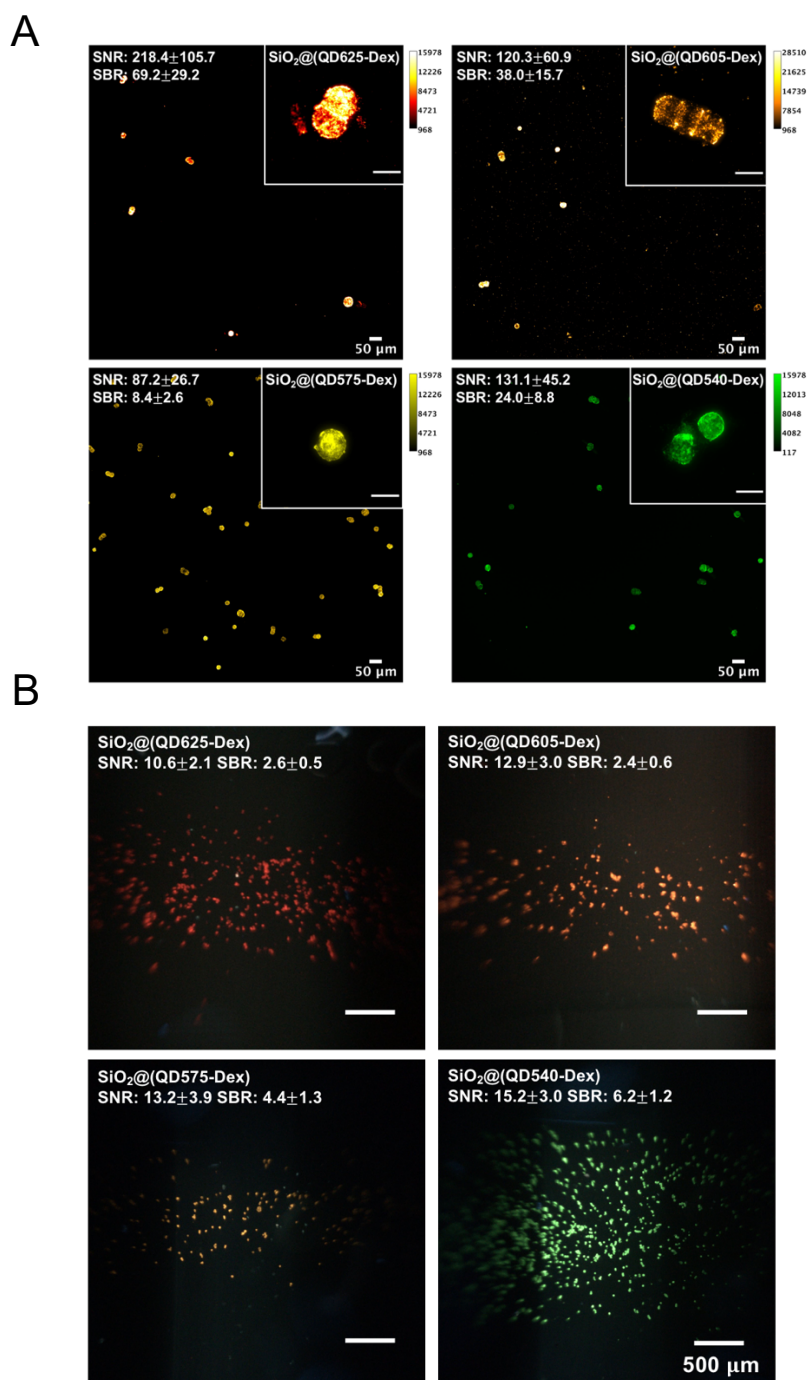


Figure 3.8 (A) Microscope PL images of fixed SK-BR3 cells labeled with $\text{SiO}_2@(\text{QD-Dex})$ of various colors (10 \times objective, scale bar = 50 μm , in main images; and 60 \times objective, scale bar = 20 μm , in inset images). All images were acquired under same lamp intensity and exposure time. PL-images are false-colored from the measured monochrome intensity values. SNR and SBR were calculated from the 10 \times objective images. **(B)** Smartphone RAW images of fixed SK-BR3 cells labeled with $\text{SiO}_2@(\text{QD-Dex})$ of various colors. All images were acquired under same smartphone settings (ISO200, exposure time 1/30s). The flow direction was from right to left.

In anticipation of multicolour labeling of multiple antigens in the same sample, SiO₂@(QD-CM-Dex)-(anti-HER2) conjugates were also prepared using carbodiimide coupling (*vide infra*) instead of anti-HER2 TAC. These conjugates were prepared in the four different PL emission colours (QD650, QD605, QD575, QD540). Aliquots (50 μ L, $\sim 1.1 \times 10^6$ cells/mL) of fixed SK-BR3 cells were then separately incubated with each of the conjugate colours and washed. Labeled cells were injected into the smartphone-based flow cytometer and smartphone videos were recorded for analysis. **Figure 3.9 (A)** shows representative images of the labeled cells during the smartphone video recording. The origin of the blue background is mainly scattered illumination light, which is mostly captured by the blue channel of the smartphone camera. There is low or no R or G channel background for the smartphone videos. **Figure 3.9 (B)** shows the red (mean R) and green colour (mean G) features of the fixed SK-BR3 cells labeled with the various colours of SiO₂@(QD-CM-Dex)-(anti-HER2) conjugates. Each data point represents an average R or G value of one tracked object detected in multiple image frames as it flowed through the microfluidic chip. In order to minimize effects caused by the fluctuation of the excitation laser light intensity (405nm) and non-uniform illumination across the microfluidic channel, a ratio of Mean R and Mean G value to colour feature of the blue channel (Mean B) was used. This ratio makes different groups more compact and easier to be separated. The Mean R/Mean B ratio and Mean G/Mean B ratio were also be used in subsequent experiments.

The four colours of SiO₂@(QD-CM-Dex) have a high SNR (7–18) under smartphone camera and can be used in multicolour imaging of cells with different antigens if proper antibodies were selected. For example, if four cell lines uniquely expressed four different antigens, these four cell lines could be imaged, categorized and counted at the same time based on the colour of immunolabeling. Another colour of SiO₂@(QD-CM-Dex) between yellow and green can potentially be added for a higher multiplexing capacity. However, this capacity decreases as signal values goes down since the lines for each colour in Figure 3.9(B) converge at low values. Also, the targeted cell lines should not have commonly targeted antigens in order to avoid crosstalk between colour channels. When one or more cell lines have multiple antigens of interest, the red

and green $\text{SiO}_2@(\text{QD-CM-Dex})$, which are approximately orthogonal in the colour feature plot, can be used for co-expression analysis.

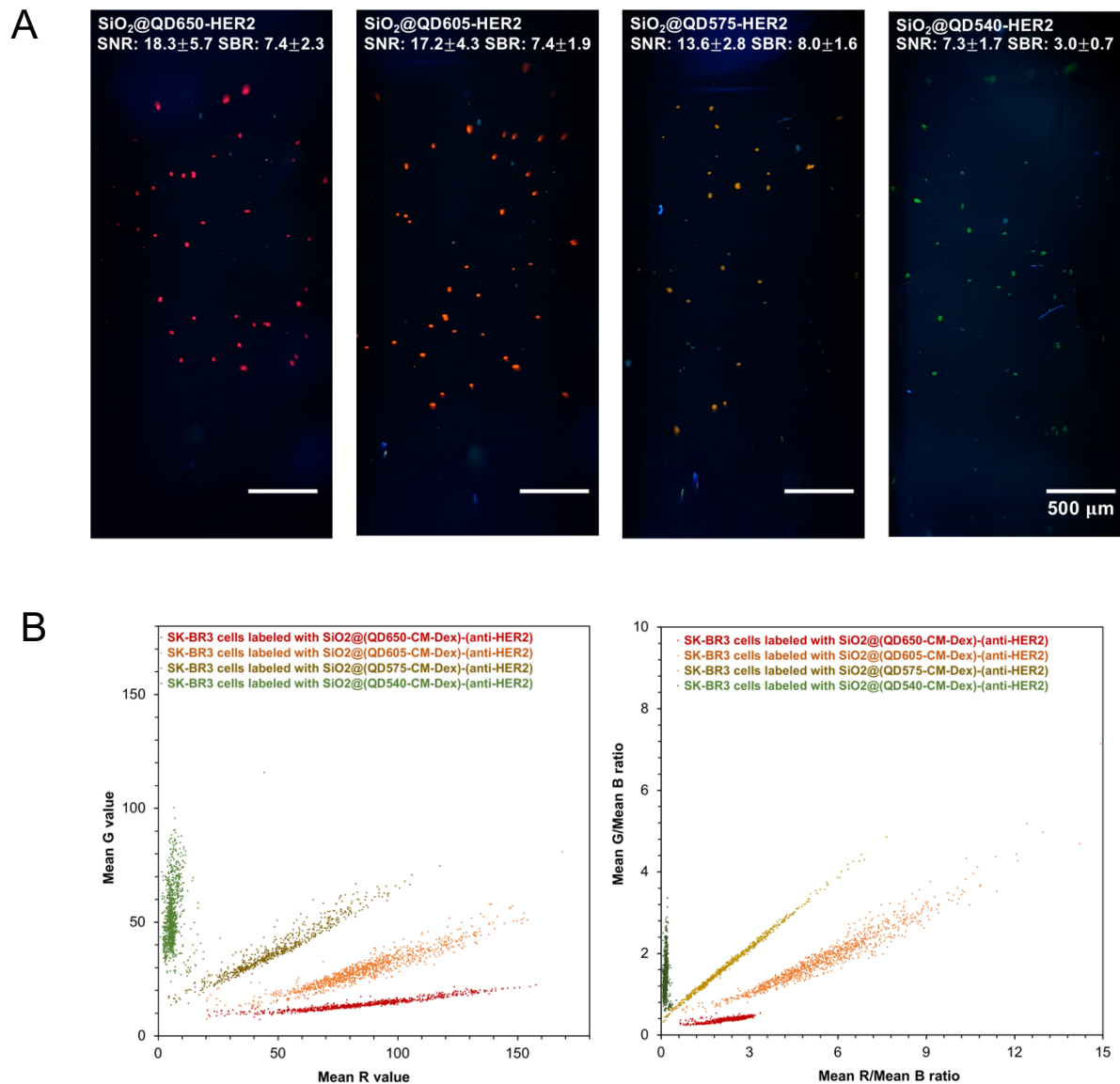
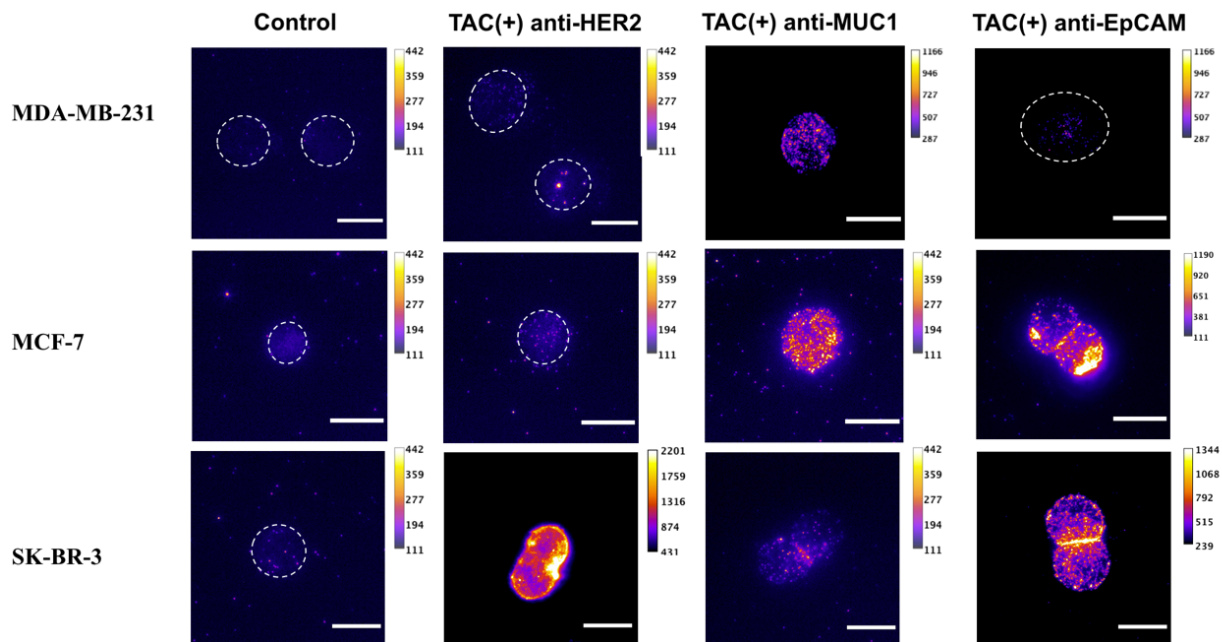


Figure 3.9 (A) Representative smartphone images of labeled SK-BR3 cells with $\text{SiO}_2@(\text{QD-CM-Dex})-(\text{anti-HER2})$ conjugates of various colours (QD650, QD605, QD575, and QD540, the notation of $\text{QD}\lambda$ refers to the wavelength of peak PL emission for the starting QDs). The smartphone images were all captured at same settings (ISO 100, 1/30s, 4000K). (B) Image colour features of SK-BR3 cells labeled with $\text{SiO}_2@(\text{QD-CM-Dex})-(\text{anti-HER2})$ conjugates of various QD colours. Each frame of the smartphone videos is a JPEG image in RGB color format.

3.5.3 Immunolabeling and imaging of multiple antigens across SK-BR3, MDA-MB-231, and MCF-7 cells

For an initial evaluation of the potential to analyze multiple antigens across multiple cell lines, SK-BR3, MDA-MB-231, and MCF-7 cells were immunolabeled with SiO₂@QD and TACs. In these experiments, an aliquot of fixed cells (50 μ L, $\sim 1.1 \times 10^6$ cells/mL) was pipetted into a 1.7 mL microcentrifuge tube and labeled with SiO₂@(QD625-Dex) using a TAC that targeted either HER2, MUC1, or EpCAM. Immunolabeled cells (7.5 μ L) were dispensed on a glass microscope slide and imaged under a research-grade microscope (see **Figure 3.10 (A)**). The expression levels, measured as PL intensities, are shown in **Figure 3.10 (B)** and are consistent with expectations from a database.¹⁴⁴ For subsequent multiplexed analyses, this data allowed us to match the brightest colours SiO₂@QD with the antibodies targeting the genes that show the lowest expression levels, ideally optimizing signals across all antigens.

A



B

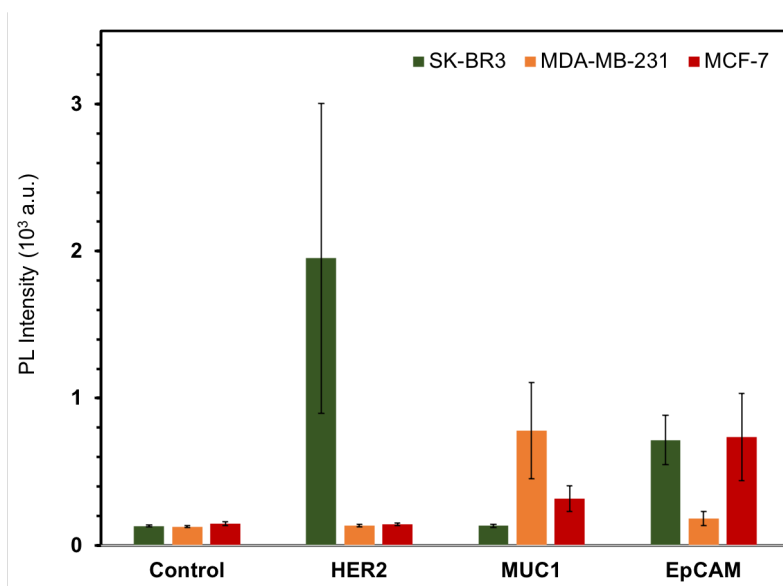


Figure 3.10 (A) Microscope PL images of labeled cells with different antigen expression levels acquired under a 60 \times objective. Control were cells incubated with SiO₂@(QD625-Dex) without TAC. Unlabeled cells are outlined with dashed circles. Scale bar = 20 μ m. All images were acquired under same lamp intensity and exposure time. PL images are false-coloured from the measured monochrome intensity values. **(B)** Average PL intensity of labeled cells (SK-BR3, MDA-MB-231, MCF-7) with error bars of one standard deviation. A minimum of 20 cells were analyzed from the microscope images acquired under a 60x objective. The dashed line represents the PL intensity level of control sample.

3.6 Multiplexed imaging SK-BR3, MDA-MB-231, and MCF-7 cells by EDC/NHS coupling of antibodies to multiple colours of SiO₂@QD

TAC with anti-dextran antibody at one end will bind to *any* SiO₂@(QD-Dex) and cannot be used for simultaneous imaging of multiple colors. A one-to-one correlation to multiple antigens is not possible because a specific anti-target TAC cannot be uniquely directed to a single color of QD. As such, EDC/NHS-based covalent coupling of different primary antibodies to SiO₂@QDs was used for multiplexed cell imaging. The API-modified dextran coating of QDs was therefore substituted with API-modified CM-Dex to provide the necessary carboxyl groups for coupling to amine groups (*e.g.* lysine residues) on the antibodies. (see **Figure 3.11**)

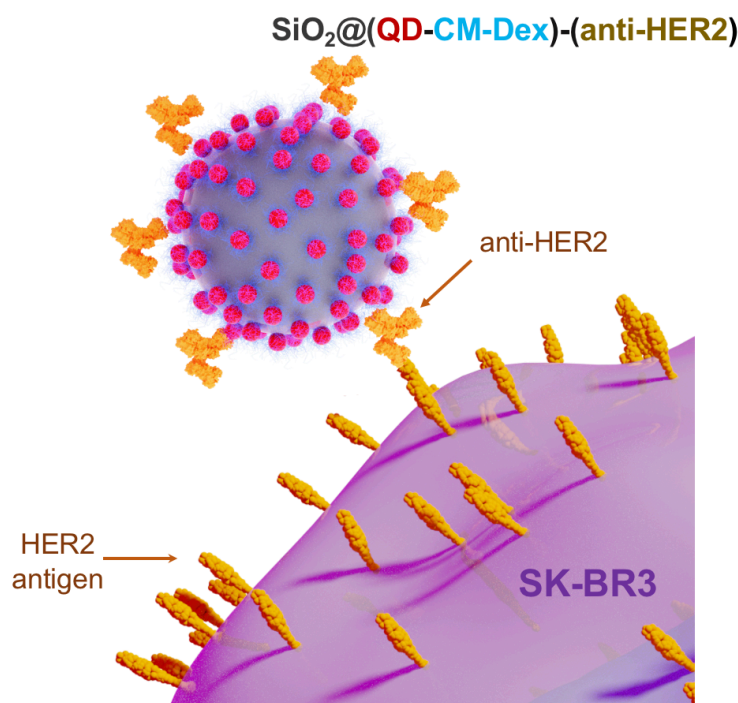


Figure 3.11 Schematic illustration of immunolabeling of HER2 antigens on SK-BR3 cells with SiO₂@(QD-CM-Dex)-(anti-HER2) conjugates. The SiO₂@(QD-CM-Dex)-(anti-HER2) conjugates were prepared via EDC/NHS-based covalent coupling first before cell labeling.

Figure 3.12 shows DIC images and PL images of the HER2+ SK-BR3 cells and HER2– MCF-7 cells labeled with SiO₂@(QD625-CM-Dex)-(anti-HER2) conjugate. SK-BR3 were successfully

labeled with the conjugates ($\text{SNR } 52.2 \pm 27.3$) and there was no significant PL intensity from the MCF-7 cells ($\text{SNR } 1.8 \pm 1.0$), indicating the specific labeling of SK-BR3 cells. When there was no EDC and NHS in the reaction between $\text{SiO}_2@QD625$ and anti-Her2 antibody, a lower PL intensity ($\text{SNR } 26.3 \pm 12.8$) was observed for the SK-BR3 cells, suggesting some adsorption of anti-HER2 antibody on the $\text{SiO}_2@(QD625\text{-Dex})$. When the SK-BR3 cells were directly incubated with $\text{SiO}_2@(QD625\text{-CM-Dex})$, no significant PL intensity was observed ($\text{SNR } 4.1 \pm 1.7$), indicating little or no non-specific binding of $\text{SiO}_2@(QD625\text{-CM-Dex})$ to the cells.

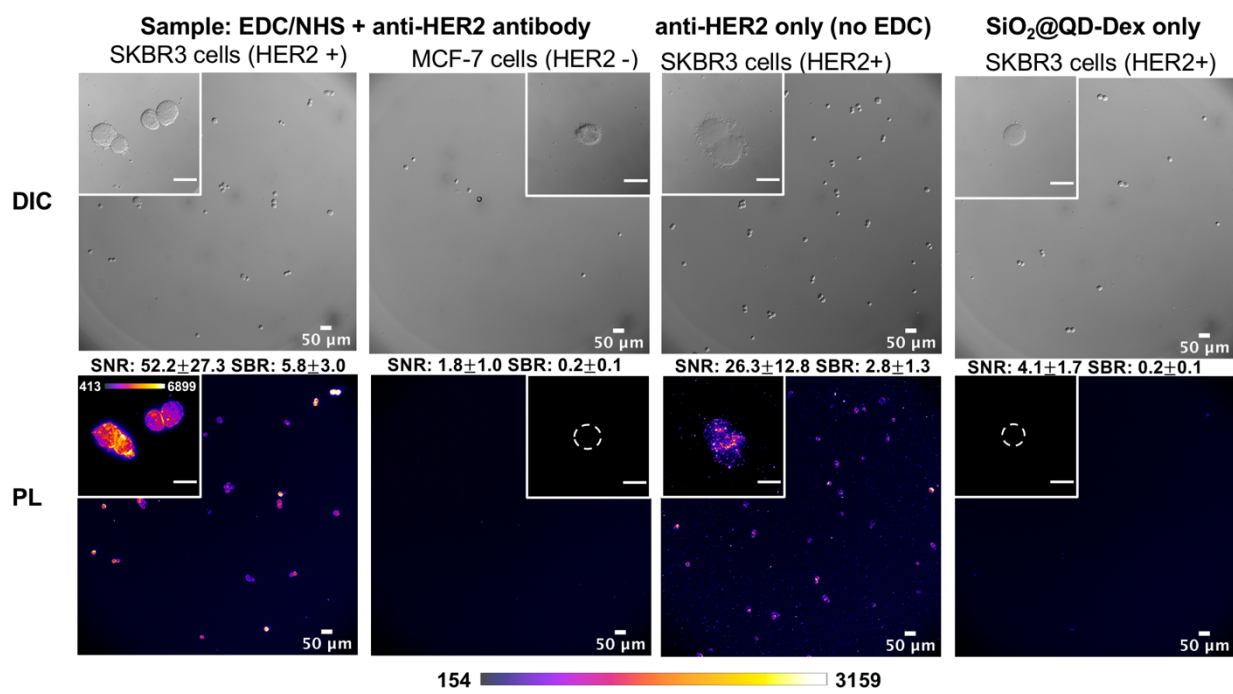


Figure 3.12 Immunolabeling of fixed SK-BR3 (HER2+) and MCF-7 (HER2-) cells with $\text{SiO}_2@QD625$ -antibody bioconjugates via EDC coupling. DIC images are shown in the top row and PL images (10× objective, scale bar = 50 μm , main images and 60× objective, scale bar = 20 μm , inset images) are shown in the bottom row. All images were acquired under the same microscope settings. SBR and SNR values for the PL images were calculated from the 10× objective images.

The above method was extended to multiple cancer cell lines with various colors of $\text{SiO}_2@(QD\text{-Dex})$. **Figure 3.13** shows microscope images of fixed MDA-MB-231 cells, A549 cells, and SK-

BR3 cells immunolabeled with SiO₂@QD-antibody conjugates, where the corresponding antibodies and QD emission colours are listed in **Table 3.2**. As the different colours of QD had different brightness, the brightest SiO₂@QD was paired with the antigen with the lowest anticipated expression level and *vice versa*.

Table 3.2 Targeted cell lines and corresponding antibodies conjugated to different colours of QDs

Labels	Conjugated antibody	Targeted cell lines
SiO ₂ @(QD650-CM-Dex)	CD44	A549
SiO ₂ @(QD605-CM-Dex)	MUC1	MDA-MB-231
SiO ₂ @(QD540-CM-Dex)	HER2	SK-BR3

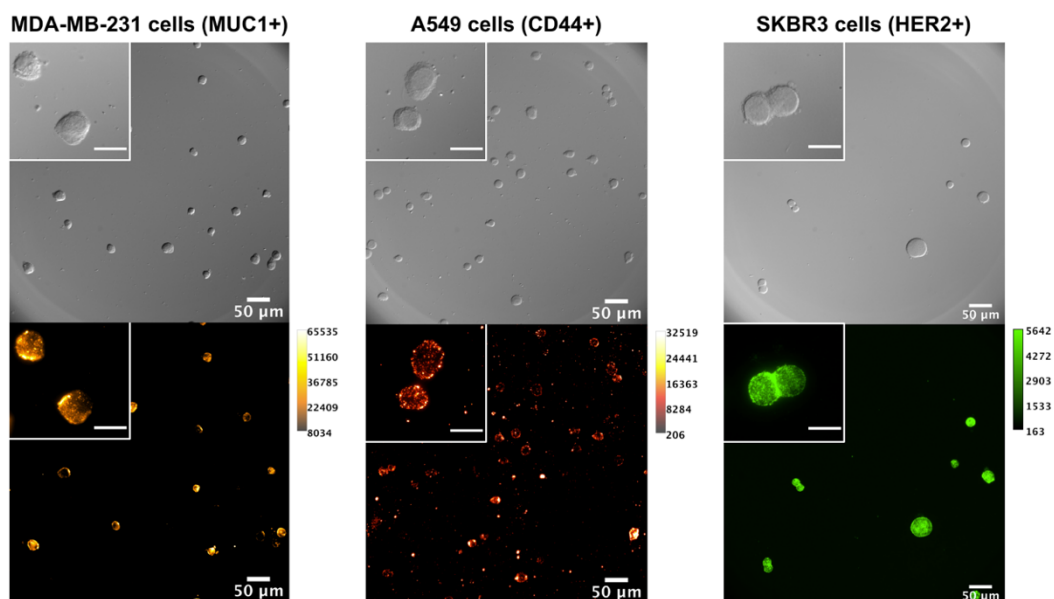


Figure 3.13 Microscope images (20× objective, scale bar = 50 μm, main images and 60× objective, scale bar = 20 μm, inset images) with calibration bars of fixed MDA-MB-231, A549, and SK-BR3 cells labeled with SiO₂@QD 605-anti-MUC1, SiO₂@QD650-anti-CD44 and SiO₂@QD540-anti-HER2 respectively.

Figure 3.14 shows the average PL intensities for MDA-MB-231, A549, and SK-BR3 cells labeled separately with SiO₂@QD605 self-assemblies, SiO₂@QD650 self-assemblies, and SiO₂@QD540

self-assemblies, respectively. Each colour of SiO₂@(QD-CM-Dex)-antibody conjugates were prepared with anti-MUC1, anti-CD44, and anti-HER2 in separate batches for incubation with the corresponding cell line. Consistent with expectations¹⁴⁴, the most prominent labeling was HER2 antigen for SK-BR3 cells, MUC1 for MDA-MB-231 cells, and CD44 for A549 cells.

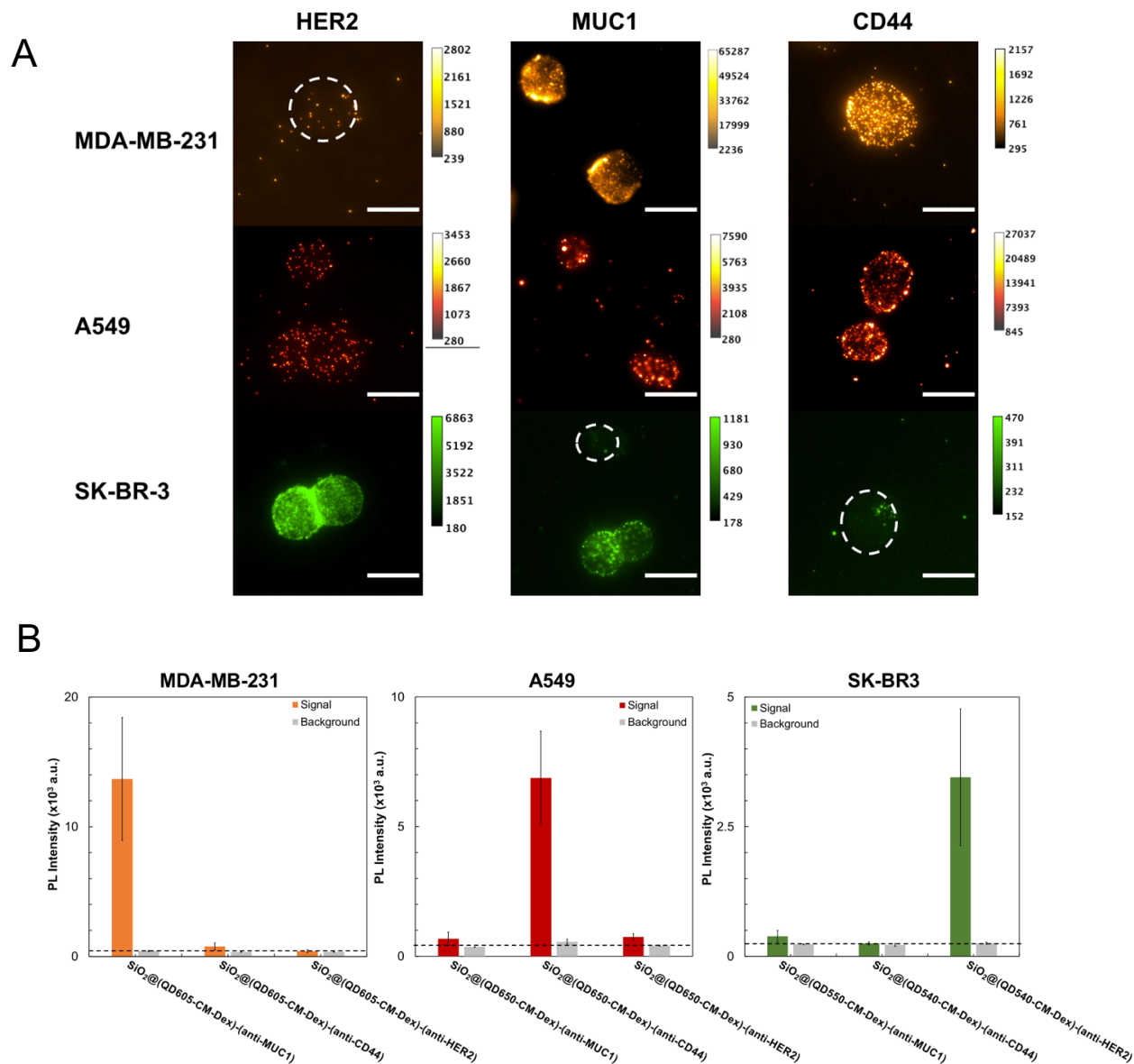


Figure 3.14 (A) Microscope PL images of fixed MDA-MB-231 cells, A549 cells, and SK-BR3 cells labeled with SiO₂@QD-antibody conjugates targeting multiple antigens (HER2, MUC1, CD44) under 60x magnification. Scale bar = 20 μ m. (B) Average PL intensity from the labeled cells and background for each antigen. A minimum of 20 cells were imaged with a research-grade microscope under 60x magnification.

3.7 Selective cell counting with multiple colors of SiO₂@QD assemblies

To test selective and parallel counting of fixed SK-BR3 and MDA-MB-231 cells in the same sample, SiO₂@(QD540-CM-Dex) were conjugated with anti-HER2 and SiO₂@(QD650-CM-Dex) were conjugated with anti-MUC1.

Cell counts of two cell lines were obtained using a MATLAB linear support-vector machine (SVM) classification model (see **Appendix A.3**). Two linear SVM models were trained and then used for the classification of the mixed test samples of two cell lines. A linear “SVM(RG)” model was trained based on a dataset consisting of two groups (red, R, and green, G) with an accuracy of 99.6%, whereas a linear “SVM(RGN)” model was trained based on a dataset of three groups (R, G, and non-categorized, N) with an accuracy of 99.4%. For both models, the red training group was suspensions of MDA-MB-231 cells immunolabeled with SiO₂@(QD650-CM-Dex)-(anti-MUC1) conjugates, and the green training group was suspensions of SK-BR3 cells immunolabeled with SiO₂@(QD540-CM-Dex)-(anti-HER2) conjugates. Non-categorized training groups were suspensions of unlabeled cells running through the smartphone-based flow cytometer. Mean R/Mean B ratio and Mean G/Mean B ratio extracted from the cell counting algorithm were used as two predictors for training the Linear SVM model.

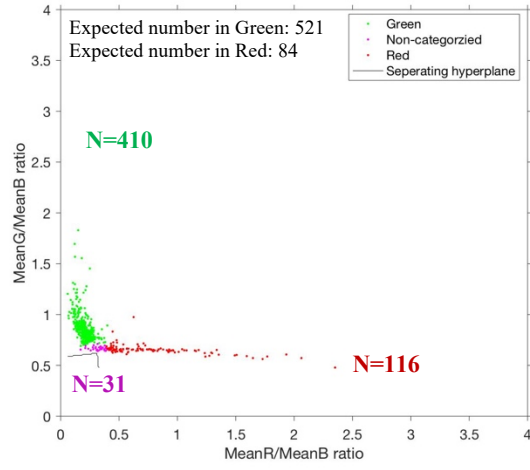
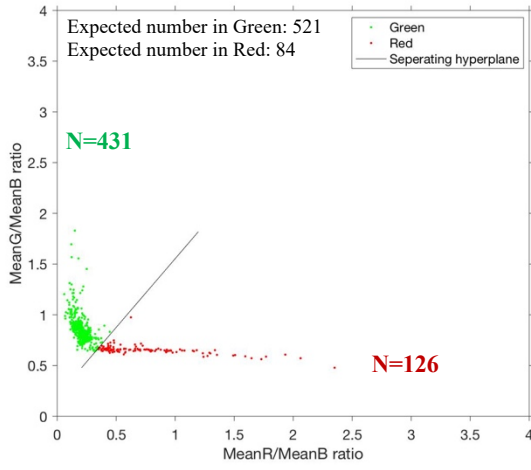
Five test samples with an increasing number of fixed MDA-MB-231 cells were mixed with a constant number of fixed SK-BR3 cells and then labeled with a mixture of SiO₂@(QD540-CM-Dex)-(anti-HER2) and SiO₂@(QD650-CM-Dex)-(anti-MUC1) bioconjugates. Two experiment sets with different number of SK-BR3 cells (low and high level) were tested to mimic the real situation. The classification results of these mixed cell suspensions are shown in **Figure 3.15**, **Figure 3.16** (low SK-BR3 cells level), **Figure 3.17**, and **Figure 3.18** (high SK-BR3 cell level) for both the linear SVM(RG) and linear SVM(RGN) models. When using the linear SVM(RG) model, some misclassification cases happened when the mean R value and mean G value were not high enough or the data points were localized around the separating hyperplane. A non-categorized group was used to exclude the objects with low R or G values. As shown in both **Figure 3.15 (B)** and **Figure 3.17 (B)**, the ratio of red objects to green objects categorized by Linear SVM(RGN) model is closer to expected red to green ratio.

A

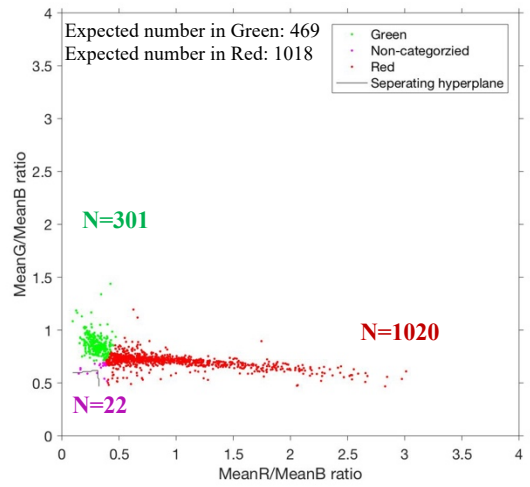
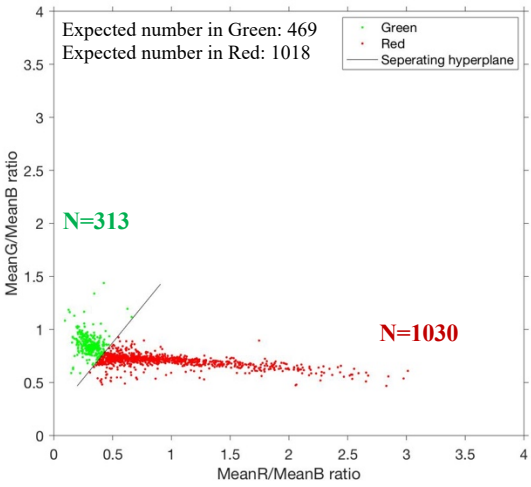
Linear SVM(RG) Model

Linear SVM (RGN)Model

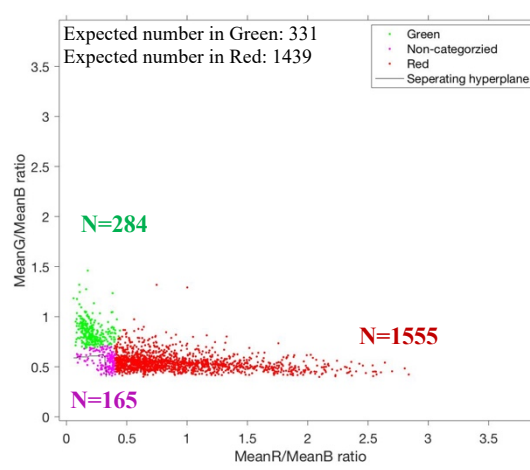
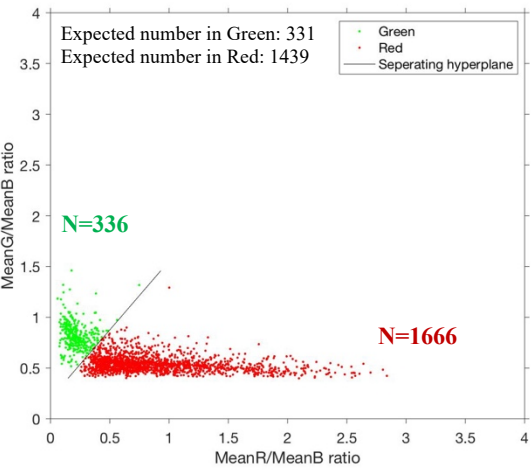
Sample 1



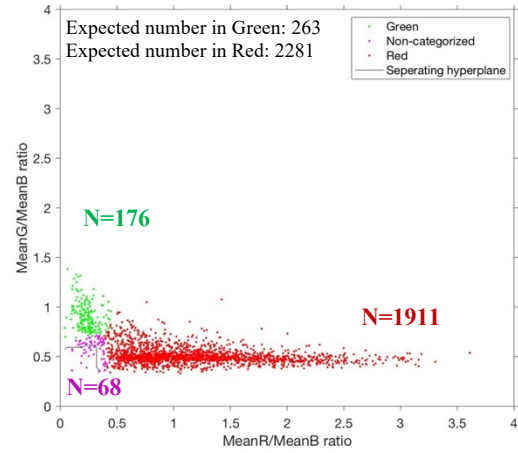
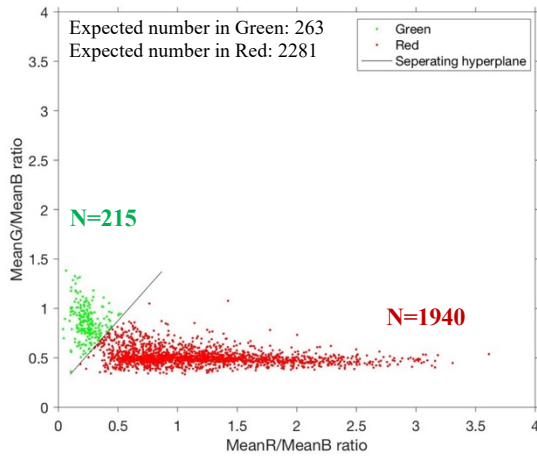
Sample 2



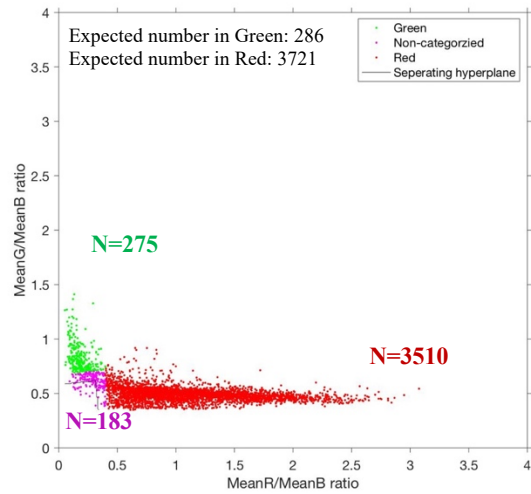
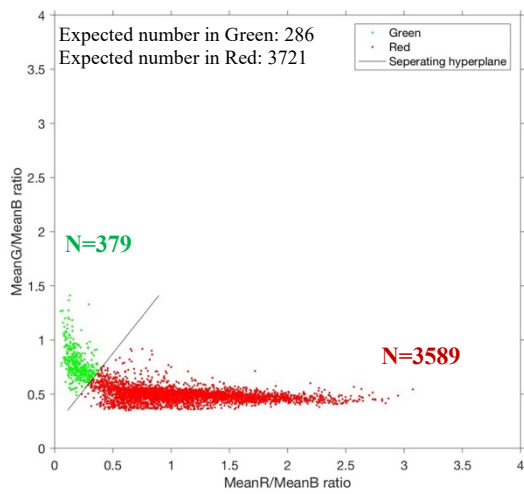
Sample 3



Sample 4



Sample 5



B

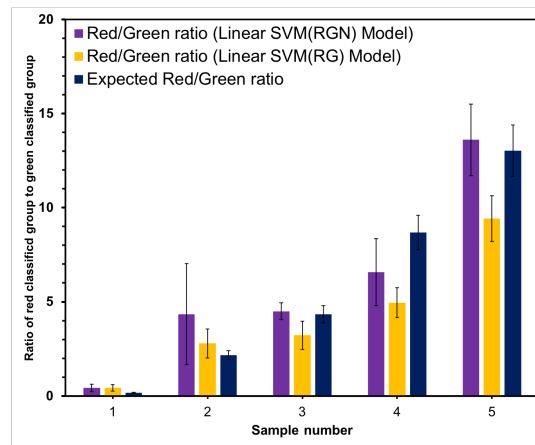


Figure 3.15 (A) Classification results of labeled SK-BR3 cells(green) and MDA-MB-231 cells(red) using a Linear SVM(RG) model (left) and labeled SK-BR3 cells(green), MDA-MB-231 cells(red), non-categorized groups(magenta) using Linear SVM(RGN) model (right). **(B)** Comparison of red objects and green objects ratio detected by MATLAB with Linear SVM(RGN) model and Linear SVM(RG) model with expected red objects to green objects ratio.

Representative smartphone images of the test samples are shown in **Figure 3.16 (A)**. Cell counts were obtained from both the smartphone-based flow cytometer and Countess II automated cell counter and shown in **Figure 3.16 (B)**. For the selective counting of MDA-MB-231 cells, the slope is 1.00 with a correlation efficient of 0.99 using Linar SVM(RG) Model and 0.96 with a correlation efficient of 0.99 using Linear SVM(RGN) Model. In a one-way analysis of variance, there was no statistically significant difference in the mean number of cell counts for SK-BR3 cells ($p>0.05$).

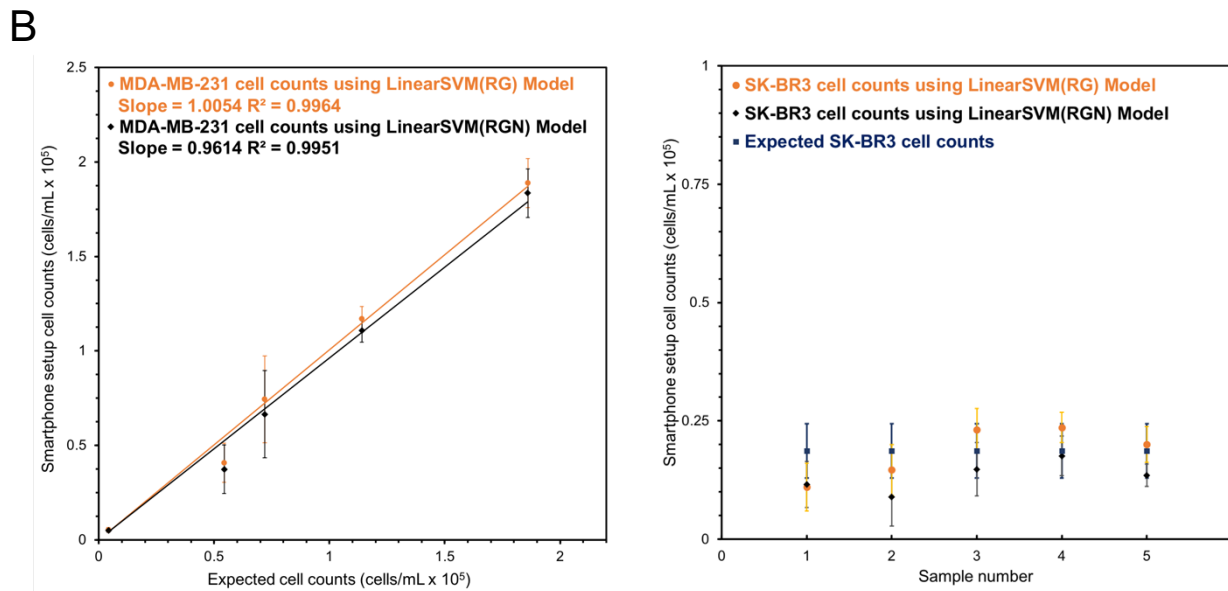
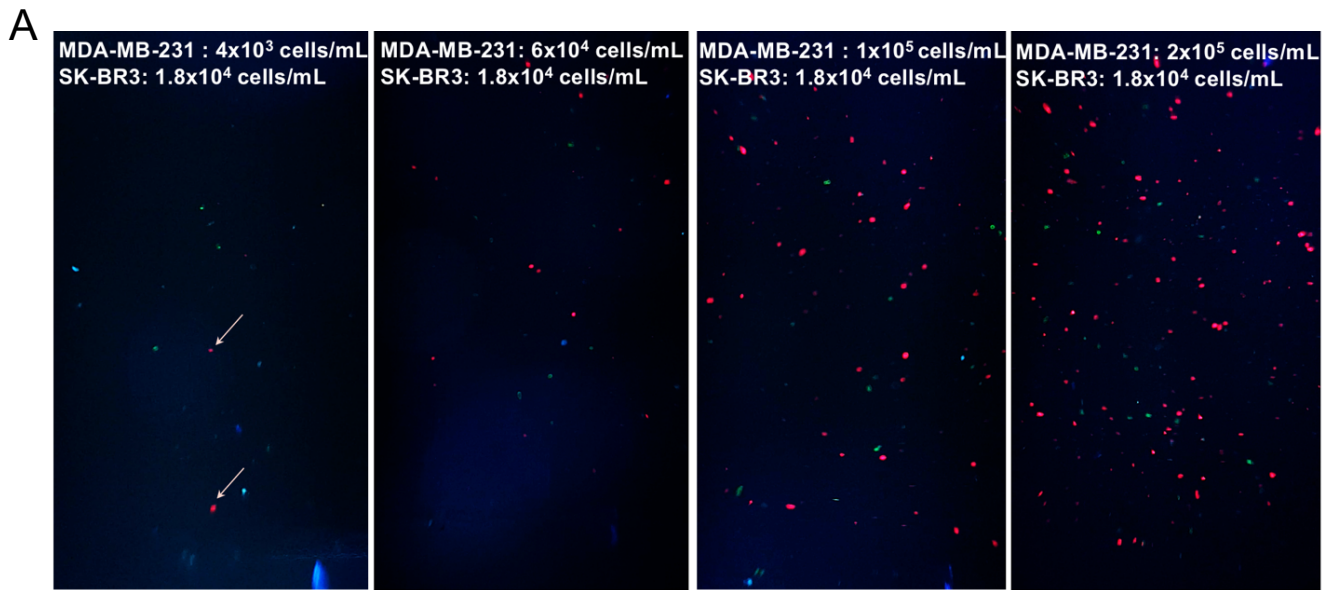


Figure 3.16 (A) Representative smartphone images of labeled SK-BR3 cells ($\text{SiO}_2\text{@QD540-anti-HER2}$) and labeled MDA-MB-231 cells ($\text{SiO}_2\text{@QD650-anti-MUC1}$). **(B)** Calibration curve of labeled MDA-MB-231 cells (left, slope 1.00, correlation coefficient $R^2 > 0.99$ using Linear SVM(RG) model; slope 0.96, correlation coefficient $R^2 > 0.99$ using Linear SVM(RGN) model) with a constant number of SK-BR3 cells (right). Error bars: expected cell counts are $\text{mean} \pm$ standard deviation of 5 test samples; SK-BR3 cell counts using the Linear SVM(RG) and Linear SVM(RGN) models are $\text{Mean} \pm$ standard deviation of 3 trials for each test sample.

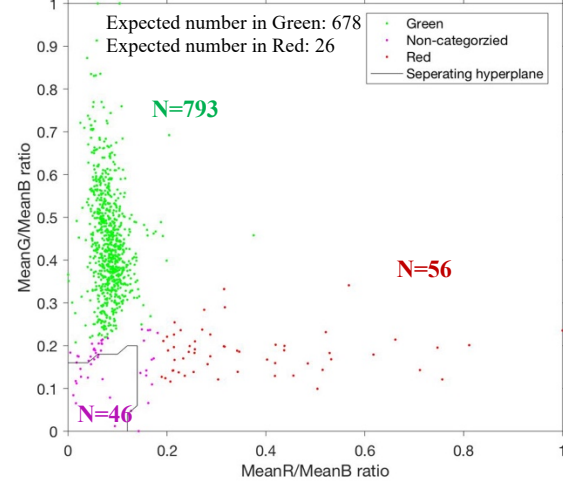
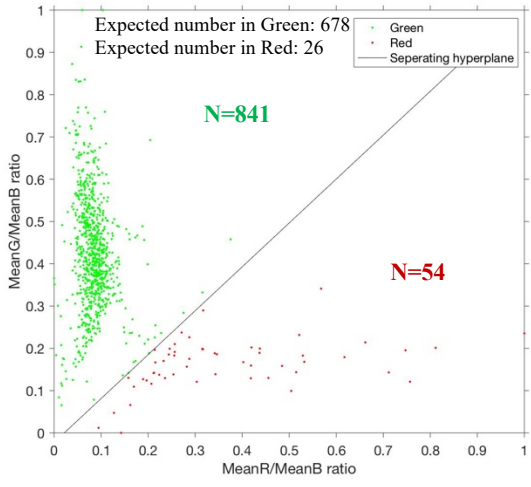
In **Figure 3.17** and **Figure 3.18**, a similar experiment as above was conducted with the smartphone-based flow cytometer except measuring an increasing number of fixed MDA-MB-231 cells against a higher number of fixed SK-BR3 cells. In both cases, the MeanR/MeanB ratio and MeanG/MeanB ratio were used as two predictors and both Linear SVM(RGN) and Linear SVM(RG) model were tested for cell classification. However, for this second set of experiments, the MeanR/MeanB ratio and MeanG/MeanB ratio of training dataset and test samples were normalized to range between 0–1 prior to classification. This normalization made the two predictors for the test samples have the same range as the training model. Representative MATLAB classification results using Linear SVM(RG) Model and Linear SVM(RGN) Model are shown in **Figure 3.17 (A)**. Comparison of the results of two models with the expected ratio of two cell lines are shown in **Figure 3.17 (B)**. Similar as the above experiment, with a higher cell concentration of background SK-BR3 cells, the Linear SVM(RGN) Model was also closer to the expected value than the Linear SVM(RG) Model. Representative smartphone images are shown in **Figure 3.18 (A)** and cell counts of both cell lines are shown in **Figure 3.18 (B)**. For the selective counting of MDA-MB-231 cells, the slope is 0.89 with a correlation efficient of 0.99 using the Linear SVM(RG) Model and 0.82 with a correlation efficient of 0.99 using the Linear SVM(RGN) Model. In a one-way analysis of variance, there was no statistically significant difference in the mean number of cell counts for SK-BR3 cells ($p>0.05$).

A

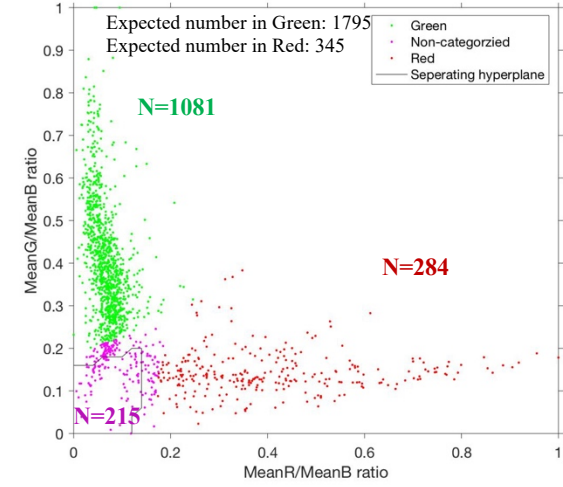
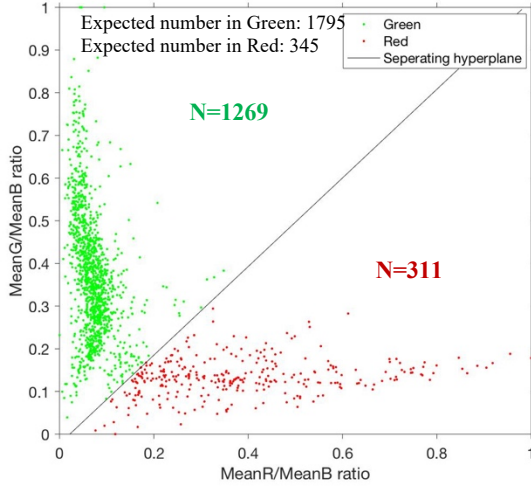
Linear SVM(RG) Model

Linear SVM(RGN) Model

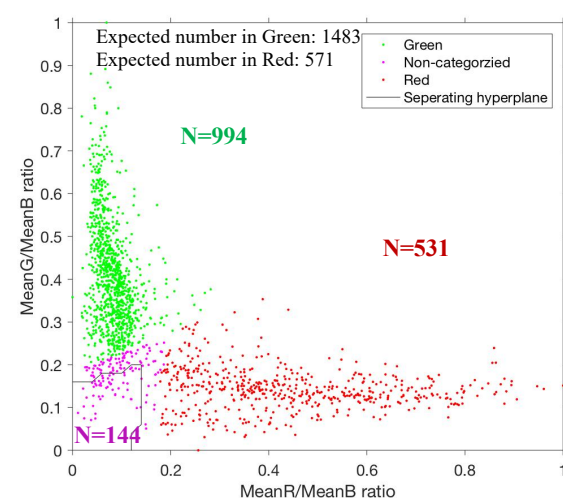
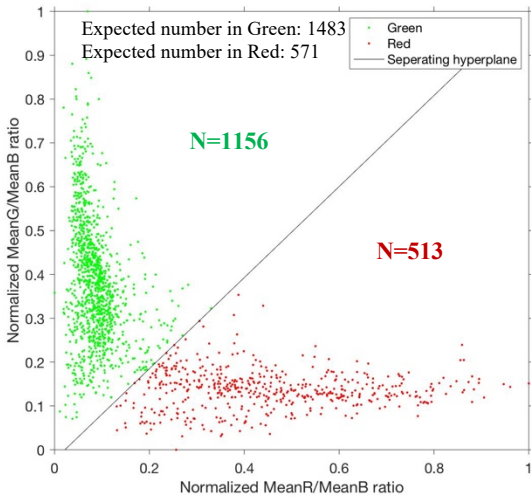
Sample 1



Sample 2



Sample 3



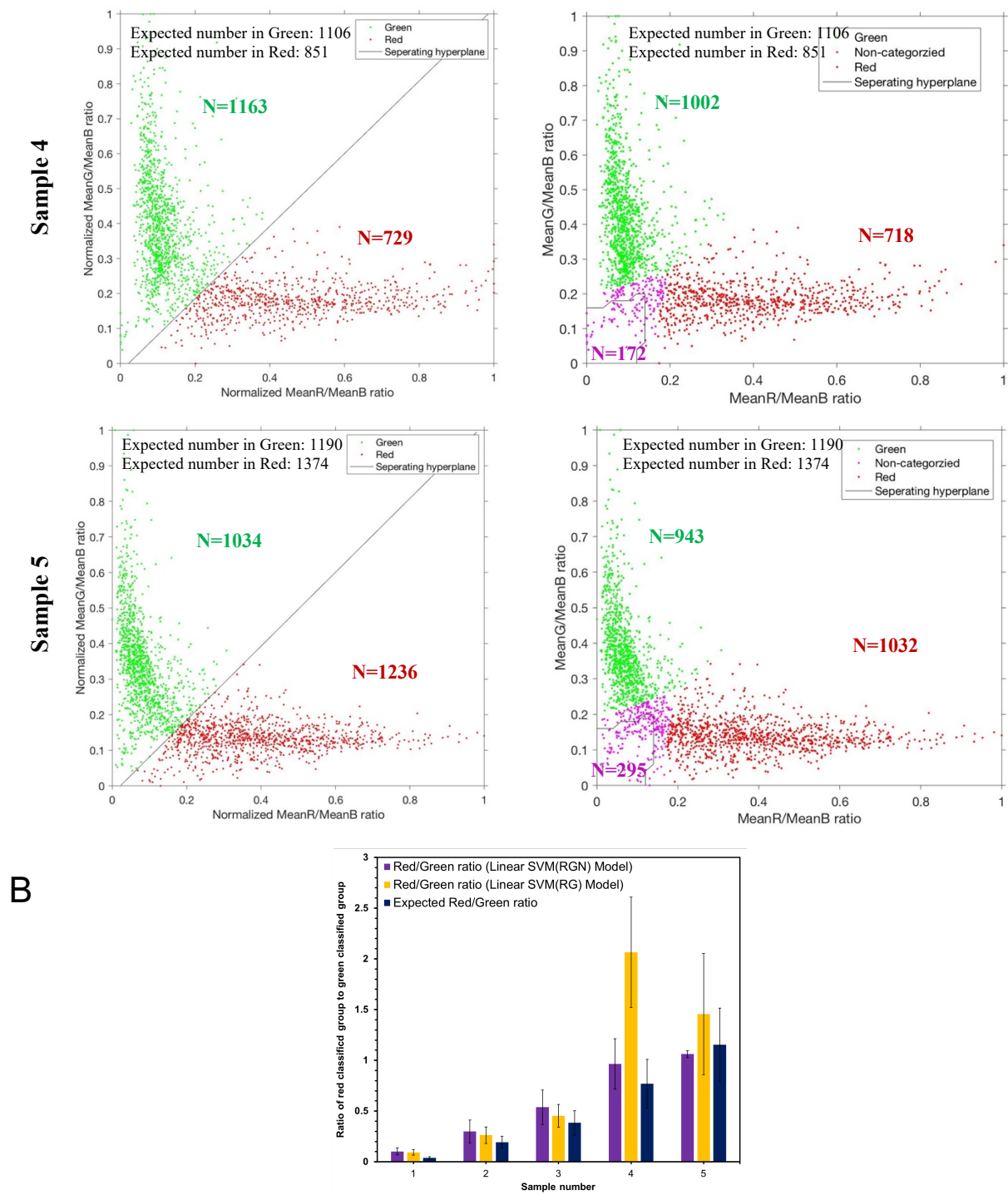
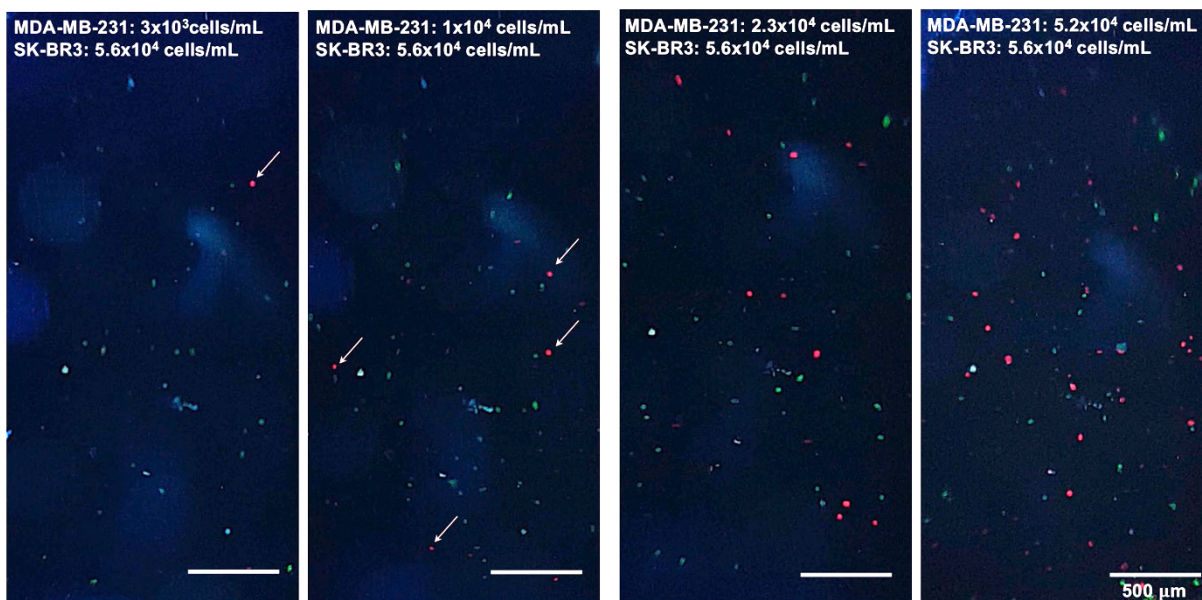


Figure 3.17 (A) Classification results of labeled SK-BR3 cells(green) and MDA-MB-231 cells(red) using Linear SVM(RG) model (left) and labeled SK-BR3 cells(green), MDA-MB-231 cells(red), non-categorized groups(magenta) using Linear SVM(RGN) model (right). **(B)** Comparison of red objects and green objects ratio detected by MATLAB with Linear SVM(RGN) model and Linear SVM(RG) model. The expected red objects-to-green objects ratio is also shown.

A



B

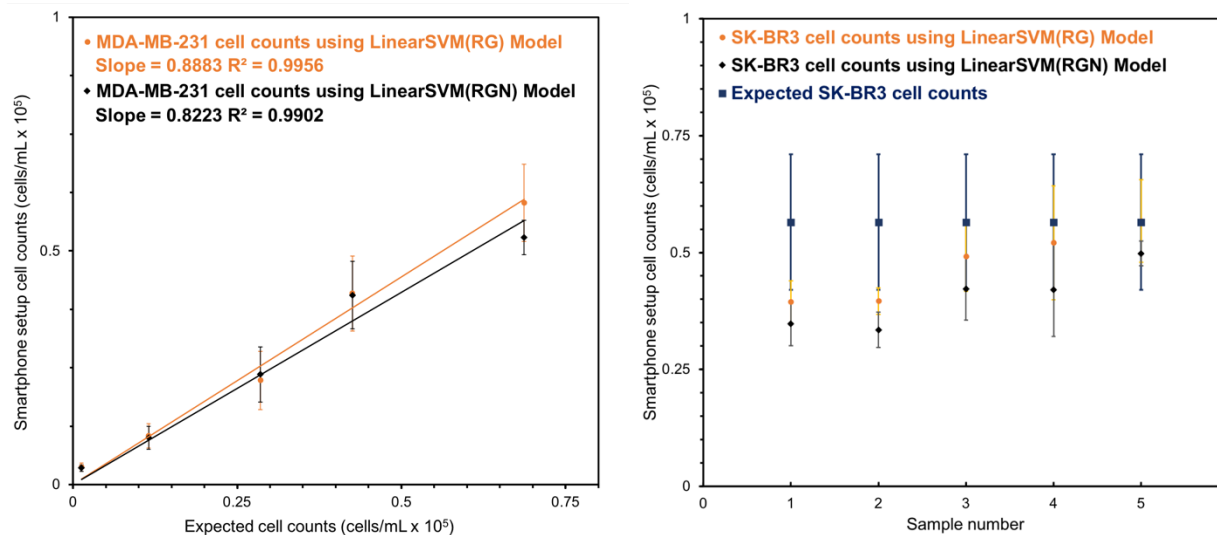


Figure 3.18 (A) Representative smartphone images of labeled SK-BR3 cells ($\text{SiO}_2@QD540\text{-anti-HER2}$) and labeled MDA-MB-231 cells ($\text{SiO}_2@QD650\text{-anti-MUC1}$). **(B)** Calibration curve of labeled MDA-MB-231 cells (left, slope 0.89, correlation coefficient $R^2 > 0.99$ using Linear SVM(RG) model; slope 0.82, correlation coefficient $R^2 > 0.99$ using Linear SVM(RGN) model) with a constant number of SK-BR3 cells (right). Error bars: expected cell counts are $\text{mean} \pm$ standard deviation of 5 test samples; SK-BR3 cell counts using the Linear SVM(RG) and Linear SVM(RGN) models are $\text{Mean} \pm$ standard deviation of 3 trials for each test sample.

3.8 Classification of different type of breast cancer cell lines with multiple colours of SiO₂@QD self-assemblies

There are many types of breast cancers, which differ in the molecular hallmarks. For example, some breast cancers have estrogen receptor (ER) or progesterone receptor (PR) and are sensitive to specific hormones, whereas others have different tumor biomarkers. In order to evaluate the aggressiveness of breast cancers and likely response to certain drugs used for treatment, clinicians categorize breast cancers into multiple groups based on the presence of ER or PR and HER2 status.¹⁴⁵ We therefore investigated the potential for classification of different type of breast cancer cell lines (SK-BR3, MDA-MB-231, MCF-7) using a combination of SiO₂@(QD650-CM-Dex)-(anti-ER), SiO₂@(QD575-CM-Dex)-(anti-MUC1), and SiO₂@(QD540-CM-Dex)-(anti-HER2).

The first step for the above was to evaluate immunolabeling with anti-ER, which had not been tested to this point. ER is mainly found intracellularly but can also be found in lesser quantities at cell membranes. In **Figure 3.19**, an aliquot (7.5 μ L) of paraformaldehyde fixed MCF-7 cells labeled with SiO₂@(QD650-CM-Dex)-(anti-ER) conjugates were imaged under a research-grade microscope. Considering the size of SiO₂@QD650 (~100 nm), cell permeabilization steps were not used and an anti-ER antibody (Abcam, Toronto, ON, Canada) targeting the ER in the cell membrane was chosen for cell labeling. Although successful labeling was observed with anti-ER antibody on MCF-7 cells, aggregates of (SiO₂@QD650-CM-Dex)-(anti-ER) conjugates were also shown in the background of different cell lines even after three wash cycles. The stability of the (SiO₂@QD650-CM-Dex)-(anti-ER) conjugates should be optimized in the future for cell immunolabeling and further cell classification applications. At this time, it is unclear why limited colloidal stability is observed for these antibody conjugates and not others.

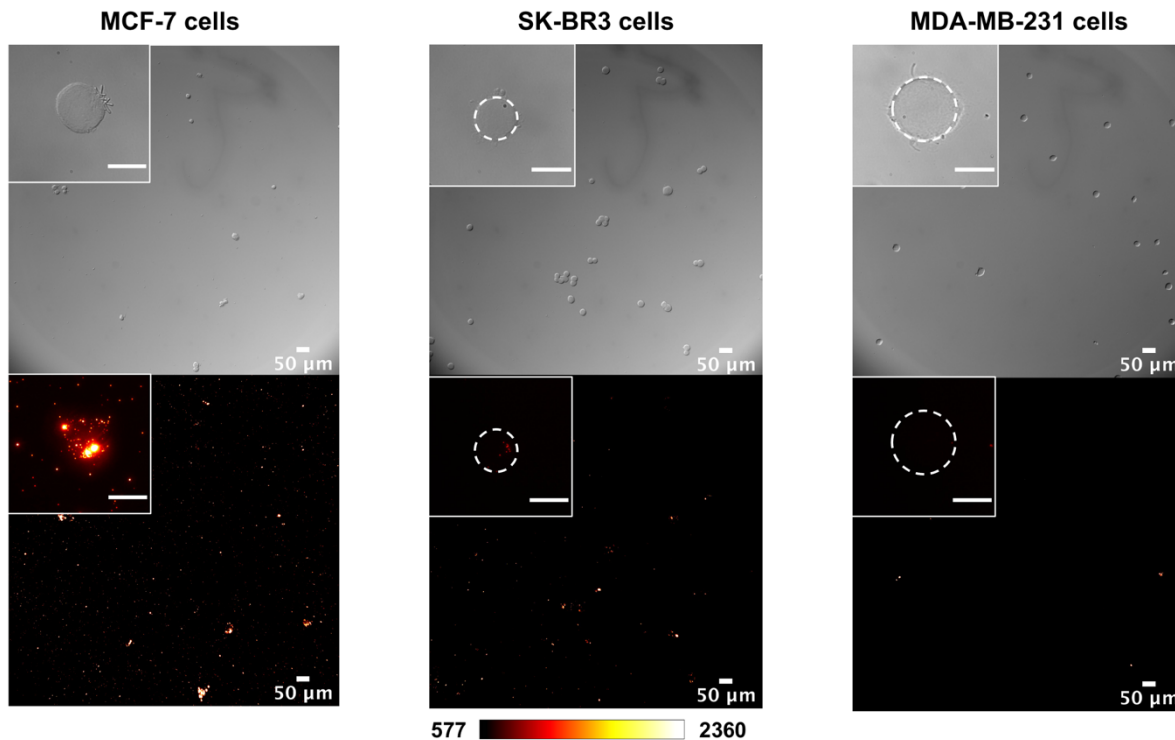


Figure 3.19 Microscope DIC and PL images (10x objective, scale bar = 50 μm , main images and 60x objective, scale bar = 20 μm , inset images) with calibration bars of fixed MCF-7, SK-BR3 and MDA-MB-231 cells labeled with $\text{SiO}_2\text{@QD 650-anti-ER}$ conjugate respectively.

Next, aliquots (50 μL) of paraformaldehyde fixed SK-BR3 cells, MDA-MB-231 cells and MCF-7 cells were resuspended in Easy Sep buffer (200 μL) in three separate microcentrifuge tubes and incubated in Easy Sep buffer for 1 h, followed by incubation with a combination of $\text{SiO}_2\text{@(QD650-CM-Dex)-(anti-ER)}$, $\text{SiO}_2\text{@(QD575-CM-Dex)-(anti-MUC1)}$ and $\text{SiO}_2\text{@(QD540-CM-Dex)-(anti-HER2)}$ conjugates. An aliquot (7.5 μL) of labeled cell solutions was dropped on a microscope glass slide and imaged under a microscope. PL emission spectra were measured for the labeled cells with a microscope-attached spectrometer and are also shown in **Figure 3.20**. SK-BR3 cells expressed mainly HER2 antigen and small amounts of ER antigen. MDA-MB-231 cells expressed mainly MUC1 antigen, which was confirmed in the PL spectra, as the PL shown in the red channel was due to crosstalk between the red-channel filter (600nm LP) and the yellow QD emission. Co-localization between the yellow and red filter-channel images further indicated crosstalk rather than labeling of two distinct antigens. MCF-7 cells expressed

mainly ER antigen but also MUC1 antigen, which was consistent with the TAC labeling results. All of the foregoing were consistent with expectations.¹⁴⁴

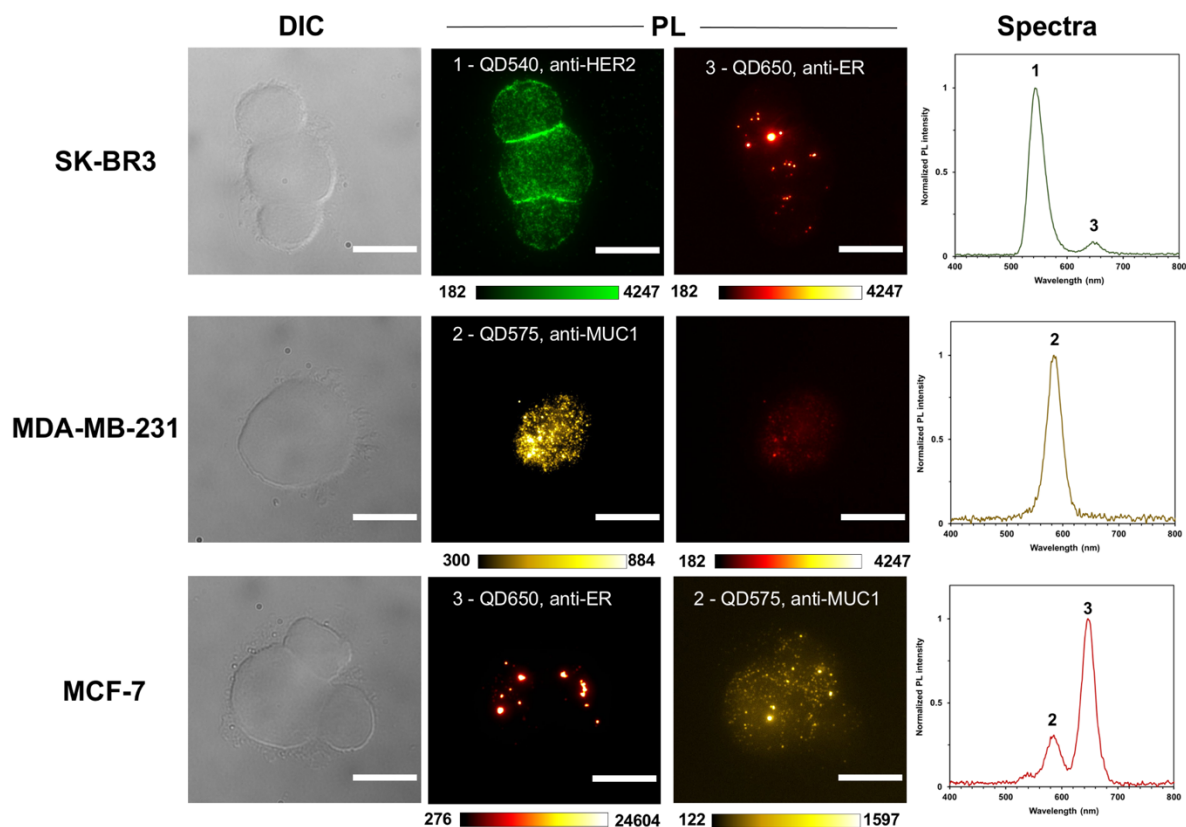


Figure 3.20 Microscope DIC and PL images (60x objective, scale bar = 20 μ m) with calibration bars and corresponding PL spectra of fixed SK-BR3, MDA-MB-231, and MCF-7 cells labeled with a combination of SiO₂@QD650-CM-Dex-(anti-ER), SiO₂@QD575-CM-Dex-(anti-MUC1), and SiO₂@QD540-CM-Dex-(anti-HER2) conjugates. The Excitation filter used for all PL images was 405/20 BP. The Dichroic mirrors used for the green QD, yellow QD, and red QD channel were T425, T510, T590, respectively. The emission filters used for the green QD, yellow QD, and red QD channel were 540/50 BP, 565/30 BP, and 600 LP, respectively.

The same cell suspensions from **Figure 3.20** were diluted with PBS buffer (100 μ L) and individually injected into the microfluidic chip of the smartphone flow cytometer. A control sample that contained only a mixture of the three SiO₂@QD-antibody conjugates in PBS buffer

was also prepared and injected. Smartphone videos were recorded at ISO 200, 4000K and 1/30s exposure time. Color features of the labeled cell solutions were extracted with the MATLAB algorithm and are shown in **Figure 3.21**. The data spots of the control sample were mostly SiO₂@QD650-anti-ER conjugate aggregates. The cutoff values of MeanG/MeanB ratio and MeanR/MeanB ratio were set as a mean value + 3SD of the control sample. As shown in **Figure 3.21**, labeled SK-BR3 cells had a major population along the green axis, as expected for SiO₂@QD540-anti-HER2, indicating a HER2⁺ ER⁻ cell group. Labeled MDA-MB-231 cells had a major population along the yellow trajectory, as expected for SiO₂@QD575-anti-MUC1, indicating a HER2⁻ ER⁻ cell group. Labeled MCF-7 cells had a major population along the red axis, as expected for SiO₂@QD650-anti-ER, indicating a HER2⁻ ER⁺ cell group.

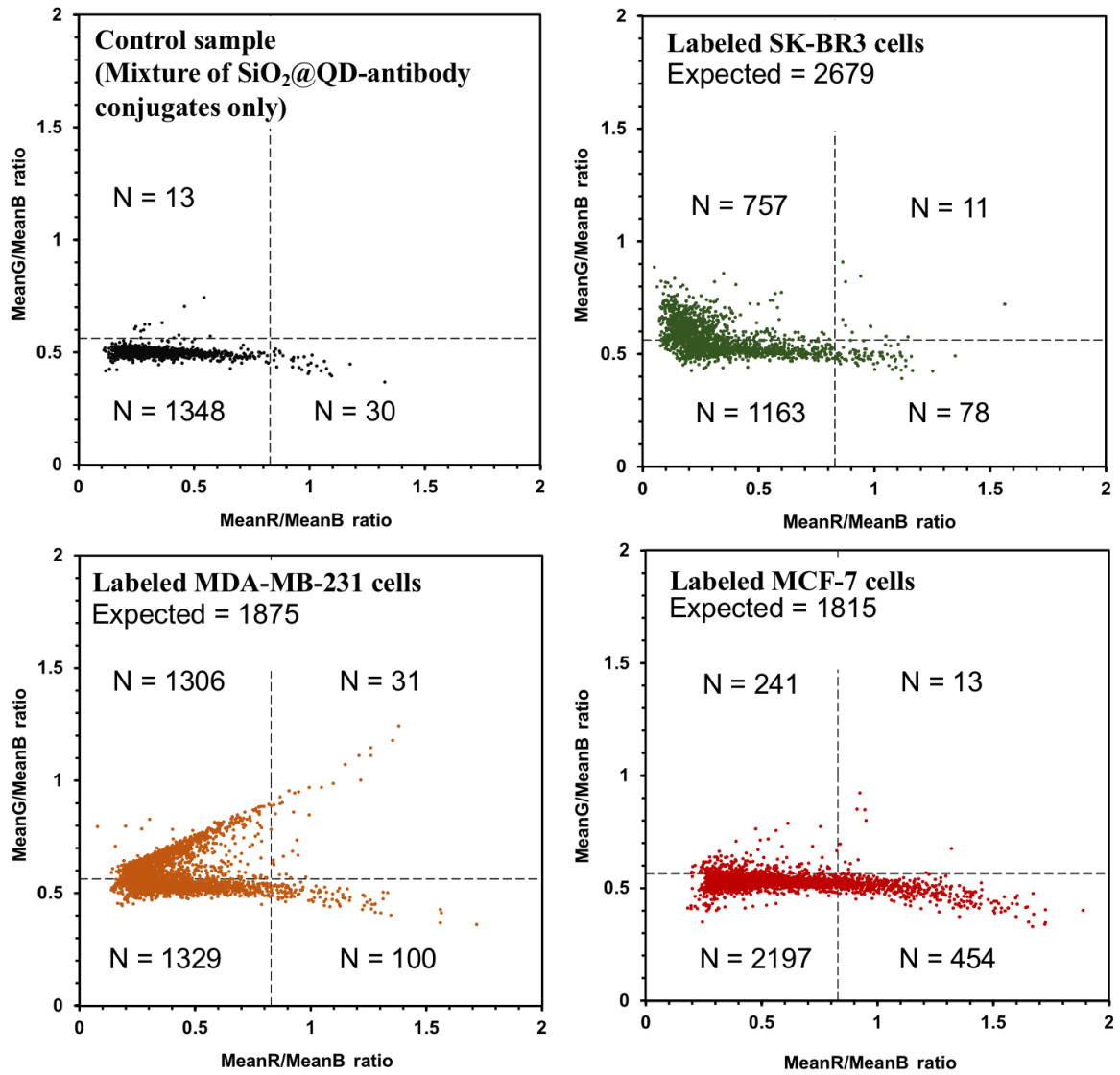


Figure 3.21 Colour feature of control sample, labeled SK-BR3 cells, MDA-MB-231 cells and MCF-7 cells extracted from the MATLAB algorithm. A Cutoff value of MeanG/MeanB ratio and MeanR/MeanB ratio were set as a mean value +3 × SD of control sample.

Chapter 4: Conclusion and Future Work

4.1 Conclusions

This thesis has presented the development of a prototype smartphone-based flow cytometer and shown a set of cell-counting and classification assays using the device. Dextran-coated SiO₂@QD assemblies of various colours were used as fluorescent labels for immunolabeling of different cancer cell types, where the brightness of these nanoparticles enabled cell imaging with sufficient signal-to-noise ratio under a smartphone camera. Selective immunolabeling of SK-BR3 cell lines was achieved with dextran-coated SiO₂@QD625 through TAC-mediated immunolabeling. A cell counting algorithm based on MATLAB computer vision toolbox was developed for object tracking and enumeration. The algorithm counted moving cells and identified their colours (RGB value) and pixel area. The smartphone-based flow cytometer quantified specifically-labeled cells within the range of around 10 cells/mL to 2×10⁵ cells/mL. The upper limit of the assay was set by leaving enough dark space between labeled cells during the measurement for reliable object detection in the MATLAB algorithm. The lower limit was based on the number of cells found in the video with a measurement time of around 4 min (~ 200 μL sample volume). The lower limit can potentially be reduced further if the measurement time is extended and more sample volume is analyzed.

The potential for multicolor FC was demonstrated, in part, with dextran-coated SiO₂@QDs with red, orange, yellow, and green emission. With TAC-mediated immunolabeling, it was shown that cells labeled with each of these colours were distinguishable based on their RGB coordinates when tracked in smartphone videos. For selective cell counting of multiple cell lines, CM-dextran-coated SiO₂@QD of various colours were prepared and conjugated with the desired antibodies through carbodiimide coupling. The smartphone-based flow cytometer categorized the cells based on colour features extracted from videos by the cell counting algorithm and quantified the cells in each colour group using an SVM machine learning model. For a proof-of-concept application, a combination of SiO₂@QD-antibody conjugates were used for classification of three types of breast cancer cell lines (SK-BR3, MDA-MB-231 and MCF-7) based on the scatter-plot pattern of the Mean G/Mean B and Mean R/Mean B ratios.

Overall, the smartphone-based flow cytometer shows the capabilities of cell imaging, enumeration, and classification using SiO₂@QD self-assemblies of multiple colours as fluorescent labels. It is a successful first prototype towards point-of-care diagnostics in the future, especially in remoted areas with limited health care resources.

4.2 Future work

In future work, more surface chemistries will be developed for SiO₂@QDs to enable TAC-based immunolabeling (*cf.* carbodiimide conjugation) multiple cell types in parallel. (Examples of such chemistries include peptide affinity tags, such as HA¹⁴⁶, and hyaluronic acid,¹⁴⁷ currently being developed by M. Massey in our group.) The TAC-based immunolabeling system is highly advantageous because it spontaneously conjugates antibodies to SiO₂@QDs and does not require crosslinking reagents and purification steps, making it an easier and more efficient approach. It also optimizes the orientation of antibodies (*i.e.* antigen-binding region point away from the nanoparticle) and provides a spacer between antibodies and SiO₂@QD assemblies (reducing potential steric hindrance from the nanoparticle). Potential applications for multicolour smartphone FC include quantitative antigen profiling of cancer cells, CTC detection, immune cell analysis, and more general detection of multiple cell types in biological samples.

Another direction for multiplexed cell imaging is to develop more SiO₂@QDs with different colours as fluorescent labels. The thesis has shown cell immunolabeling with four colours of SiO₂@QDs (red, orange, yellow, green), emitting mostly between the red and green channels of the smartphone camera. The addition of blue- and/or purple-emitting QDs,¹⁴⁸ emitting in full or in part in the blue channel of the smartphone camera, will increase the multiplexing capacity. For example, a 3D plot with red, green, and blue pixel value axes would be used for classification of cell types. (see **Figure 4.1**) Theoretically, up to 15 colours might be distinguished on the 3D plot with the addition of blue channel, and the SiO₂@QD self-assemblies might be prepared with more than one colour of QDs per SiO₂ NP in order to utilize the full RGB space. The capacity of multiplexed imaging is also limited by the different antigen expressed on multiple cell lines. If two

cell lines share the same antigen, then $\text{SiO}_2@\text{QD}$ self-assemblies that have orthogonal colour features should be used. In this case, there are up to three options (e.g. R, G and B).

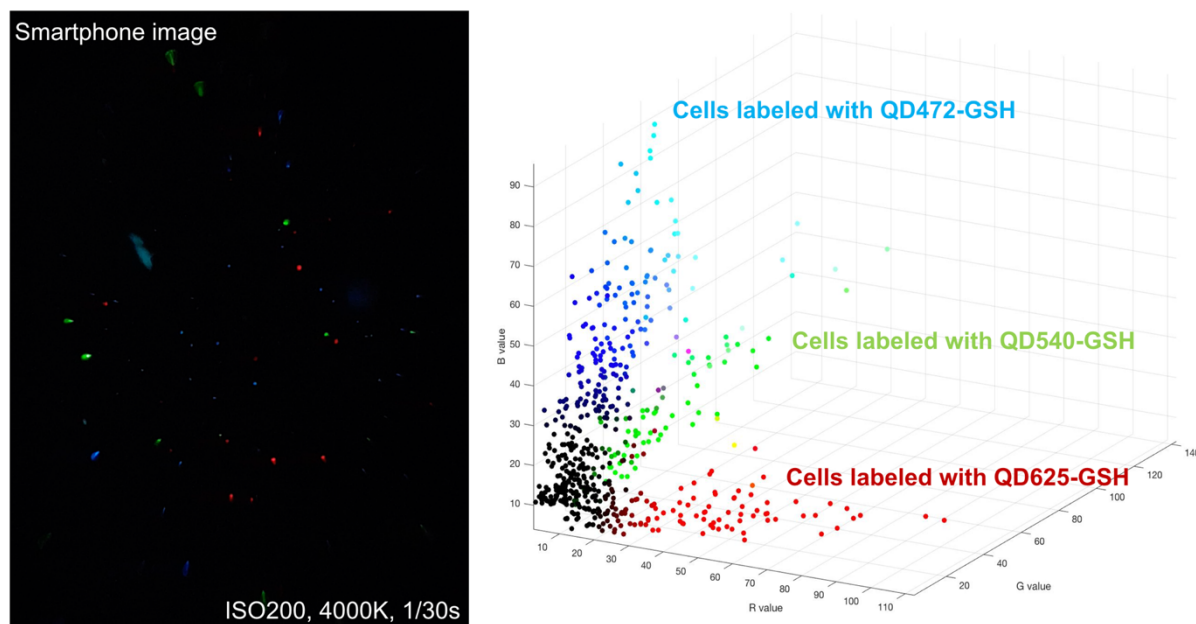


Figure 4.1 Representative smartphone image of fixed SK-BR3 cells non-specifically labeled with QD625-GSH (red), QD540-GSH (green), QD472-GSH (blue) and MATLAB result of the corresponding video different concentrations,

Another future direction for research is to upgrade the design of the smartphone-based FC. Although most of the components were inside a compact box, the smartphone FC still required an external syringe pump to inject the cell suspensions into the microfluidic chip. A 3D-printed syringe pump with different flow rates could be developed to reduce the total cost of the setup and have completed integration with the dark box. In addition, the microfluidic chip has a channel depth of $100\ \mu\text{m}$, which was limited by the resolution of the 3D printer. If the z-resolution of the 3D printing increases and a smaller channel depth can be achieved, then the cells will flow through the channel in more similar focal planes and be less easily missed by the smartphone camera, increasing the detection and tracking efficiency of the cells. Higher magnification may also allow for detection of bacterial cells, which are smaller than mammalian cells. The smartphone used in this setup was a Samsung Galaxy S8, released in 2017. Other models of smartphones can be used as well, presumably by tailoring the device lid to their design specifications. Other fluorescent

nanoparticles with higher brightness (*e.g.* Pdots¹⁴⁹) can be evaluated for use with the smartphone FC, which may increase sensitivity. New fluorescent materials with greater colloidal stability and lower non-specific binding, along with equal or better brightness, will also improve performance and reliability.

The initially targeted users for this smartphone-based flow cytometer are doctors and nurses in small clinics or communities without access to core flow cytometry facilities. Therefore, future work should also test the smartphone FC with clinical samples (*e.g.* blood, processed tissue). These samples will be more complex than those tested in the thesis and will have larger numbers of background cells and higher optical backgrounds. Aside from the abovementioned improvements in fluorescent nanoparticle brightness, colloidal stability, and non-fouling characteristics, another challenge with clinical samples may be surface modification of the PDMS-on-glass microfluidic chip. A potential obstacle with the PDMS will be its hydrophobicity, which it can quickly recover after a hydrophilization process. Non-specific binding, other fouling, or clogging of the channel may cause problems with background or operation. Different strategies have been utilized to improve the non-fouling properties of PDMS microfluidics chips,^{150–152} and these should be evaluated for tests with clinical samples.

In summary, the current prototype device and materials have compellingly demonstrated proof-of-concept for smartphone flow cytometry. Future work should explore next-generation enhancements of each component, broaden the potential scope of applications, and investigate clinical translation.

Bibliography

- (1) Algar, W. R.; Susumu, K.; Delehanty, J. B.; Medintz, I. L. Semiconductor Quantum Dots in Bioanalysis: Crossing the Valley of Death. *Anal. Chem.* **2011**, *83* (23), 8826–8837.
- (2) Fu, H.; Tsang, S. W. Infrared Colloidal Lead Chalcogenide Nanocrystals: Synthesis, Properties, and Photovoltaic Applications. *Nanoscale* **2012**, *4* (7), 2187–2201.
- (3) Bottrill, M.; Green, M. Some Aspects of Quantum Dot Toxicity. *Chem. Commun.* **2011**, *47* (25), 7039–7050.
- (4) Cheng, X.; Lowe, S. B.; Reece, P. J.; Gooding, J. J. Colloidal Silicon Quantum Dots: From Preparation to the Modification of Self-Assembled Monolayers (SAMs) for Bio-Applications. *Chem. Soc. Rev.* **2014**, *43* (8), 2680–2700.
- (5) Yong, K. T.; Law, W. C.; Hu, R.; Ye, L.; Liu, L.; Swihart, M. T.; Prasad, P. N. Nanotoxicity Assessment of Quantum Dots: From Cellular to Primate Studies. *Chem. Soc. Rev.* **2013**, *42* (3), 1236–1250.
- (6) Deka, S.; Quarta, A.; Lupo, M. G.; Falqui, A.; Boninelli, S.; Giannini, C.; Morello, G.; De Giorgi, M.; Lanzani, G.; Spinella, C.; Cingolani, R.; Pellegrino, T.; Manna, L. CdSe/CdS/ZnS Double Shell Nanorods with High Photoluminescence Efficiency and Their Exploitation as Biolabeling Probes. *J. Am. Chem. Soc.* **2009**, *131* (8), 2948–2958.
- (7) Chen, N.; He, Y.; Su, Y.; Li, X.; Huang, Q.; Wang, H.; Zhang, X.; Tai, R.; Fan, C. The Cytotoxicity of Cadmium-Based Quantum Dots. *Biomaterials* **2012**, *33* (5), 1238–1244.
- (8) Murray, C. B.; Norris, D. J.; Bawendi, M. G. Synthesis and Characterization of Nearly Monodisperse CdE (E = S, Se, Te) Semiconductor Nanocrystallites. *J. Am. Chem. Soc.* **1993**, *115* (19), 8706–8715.
- (9) Peng, Z. A.; Peng, X. Nearly Monodisperse and Shape-Controlled CdSe Nanocrystals via Alternative Routes: Nucleation and Growth. *J. Am. Chem. Soc.* **2002**, *124* (13), 3343–3353.
- (10) Peng, Z. A.; Peng, X. Formation of High-Quality CdTe, CdSe, and CdS Nanocrystals Using CdO as Precursor. *J. Am. Chem. Soc.* **2001**, *123* (1), 183–184.
- (11) Qu, L.; Peng, Z. A.; Peng, X. Alternative Routes toward High Quality CdSe Nanocrystals. *Nano Lett.* **2001**, *1* (6), 333–337.
- (12) Rosenthal, S. J.; Chang, J. C.; Kovtun, O.; McBride, J. R.; Tomlinson, I. D. Biocompatible Quantum Dots for Biological Applications. *Chem. Biol.* **2011**, *18* (1), 10–24.
- (13) Al-Salim, N.; Young, A. G.; Tilley, R. D.; McQuillan, A. J.; Xia, J. Synthesis of CdSeS

- Nanocrystals in Coordinating and Noncoordinating Solvents: Solvent's Role in Evolution of the Optical and Structural Properties. *Chem. Mater.* **2007**, *19* (21), 5185–5193.
- (14) Dabbousi, B. O.; Rodriguez-Viejo, J.; Mikulec, F. V.; Heine, J. R.; Mattoussi, H.; Ober, R.; Jensen, K. F.; Bawendi, M. G. (CdSe)ZnS Core-Shell Quantum Dots: Synthesis and Characterization of a Size Series of Highly Luminescent Nanocrystallites. *J. Phys. Chem. B* **1997**, *101* (46), 9463–9475.
- (15) McBride, J.; Treadway, J.; Feldman, L. C.; Pennycook, S. J.; Rosenthal, S. J. Structural Basis for near Unity Quantum Yield Core/Shell Nanostructures. *Nano Lett.* **2006**, *6* (7), 1496–1501.
- (16) Schwartz, O.; Oron, D.; Yuan, G.; Gómez, D. E.; Kirkwood, N.; Boldt, K.; Mulvaney, P. Two Mechanisms Determine Quantum Dot Blinking. *ACS Nano* **2018**, *52* (4), 992–1001.
- (17) Schwartz, O.; Oron, D. A Present Understanding of Colloidal Quantum Dot Blinking. *Isr. J. Chem.* **2012**, *52* (11–12), 992–1001.
- (18) Mahler, B.; Spinicelli, P.; Buil, S.; Quelin, X.; Hermier, J. P.; Dubertret, B. Towards Non-Blinking Colloidal Quantum Dots. *Nat. Mater.* **2008**, *7* (8), 659–664.
- (19) Ishikawa, M.; Biju, V. *Luminescent Quantum Dots, Making Invisibles Visible in Bioimaging*; Elsevier Inc., 2011; Vol. 104.
- (20) Foubert, A.; Beloglazova, N. V.; Rajkovic, A.; Sas, B.; Madder, A.; Goryacheva, I. Y.; De Saeger, S. Bioconjugation of Quantum Dots: Review & Impact on Future Application. *TrAC - Trends Anal. Chem.* **2016**, *83*, 31–48.
- (21) Zheng, Y.; Gao, S.; Ying, J. Y. Synthesis and Cell-Imaging Applications of Glutathione-Capped CdTe Quantum Dots. *Adv. Mater.* **2007**, *19* (3), 376–380.
- (22) Boulmedais, F.; Bauchat, P.; Brienne, M. J.; Arnal, I.; Artzner, F.; Gacoin, T.; Dahan, M.; Marchi-Artzner, V. Water-Soluble Pegylated Quantum Dots: From a Composite Hexagonal Phase to Isolated Micelles. *Langmuir* **2006**, *22* (23), 9797–9803.
- (23) Shen, L. Biocompatible Polymer/Quantum Dots Hybrid Materials: Current Status and Future Developments. *J. Funct. Biomater.* **2011**, *2* (4), 355–372.
- (24) Gerion, D.; Pinaud, F.; Williams, S. C.; Parak, W. J.; Zanchet, D.; Weiss, S.; Alivisatos, A. P. Synthesis and Properties of Biocompatible Water-Soluble Silica-Coated CdSe/ZnS Semiconductor Quantum Dots. *J. Phys. Chem. B* **2001**, *105* (37), 8861–8871.
- (25) Zhang, B.; Gong, X.; Hao, L.; Cheng, J.; Han, Y.; Chang, J. A Novel Method to Enhance Quantum Yield of Silica-Coated Quantum Dots for Biodetection. *Nanotechnology* **2008**, *19*

- (46).
- (26) Wagner, A. M.; Knipe, J. M.; Orive, G.; Peppas, N. A. Quantum Dots in Biomedical Applications. *Acta Biomater.* **2019**, *94*, 44–63.
- (27) Derfus, A. M.; Chen, A. A.; Min, D. H.; Ruoslahti, E.; Bhatia, S. N. Targeted Quantum Dot Conjugates for SiRNA Delivery. *Bioconjug. Chem.* **2007**, *18* (5), 1391–1396.
- (28) Bilan, R.; Fleury, F.; Nabiev, I.; Sukhanova, A. Quantum Dot Surface Chemistry and Functionalization for Cell Targeting and Imaging. *Bioconjug. Chem.* **2015**, *26* (4), 609–624.
- (29) Xing, Y.; Chaudry, Q.; Shen, C.; Kong, K. Y.; Zhau, H. E.; Chung, L. W.; Petros, J. A.; O'Regan, R. M.; Yezhelyev, M. V.; Simons, J. W.; Wang, M. D.; Nie, S. Bioconjugated Quantum Dots for Multiplexed and Quantitative Immunohistochemistry. *Nat. Protoc.* **2007**, *2* (5), 1152–1165.
- (30) Chan, W. C. W.; Maxwell, D. J.; Gao, X.; Bailey, R. E.; Han, M.; Nie, S. Luminescent Quantum Dots for Multiplexed Biological Detection and Imaging. *Current Opinion in Biotechnology*. Elsevier Current Trends February 1, 2002, pp 40–46.
- (31) Gao, X.; Yang, L.; Petros, J. A.; Marshall, F. F.; Simons, J. W.; Nie, S. In Vivo Molecular and Cellular Imaging with Quantum Dots. *Curr. Opin. Biotechnol.* **2005**, *16* (1 SPEC. ISS.), 63–72.
- (32) Rizvi, S. B.; Ghaderi, S.; Keshtgar, M.; Seifalian, A. M. Semiconductor Quantum Dots as Fluorescent Probes for in Vitro and in Vivo Bio-Molecular and Cellular Imaging . *Nano Rev.* **2010**, *1* (1), 5161.
- (33) Jin, Z.; Hildebrandt, N. Semiconductor Quantum Dots for in Vitro Diagnostics and Cellular Imaging. *Trends Biotechnol.* **2012**, *30* (7), 394–403.
- (34) Liu, W.; Howarth, M.; Greytak, A. B.; Zheng, Y.; Nocera, D. G.; Ting, A. Y.; Bawendi, M. G. Compact Biocompatible Quantum Dots Functionalized for Cellular Imaging. *J. Am. Chem. Soc.* **2008**, *130* (4), 1274–1284.
- (35) Mitchell, P. Advances in Imaging Are Enabling Researchers to Track More Accurately the Localization Of. *Imaging* **2001**, *19* (November).
- (36) Tran, M. V.; Susumu, K.; Medintz, I. L.; Algar, W. R. Supraparticle Assemblies of Magnetic Nanoparticles and Quantum Dots for Selective Cell Isolation and Counting on a Smartphone-Based Imaging Platform. *Anal. Chem.* **2019**, acs.analchem.9b02853.
- (37) Rosenthal, S. J.; Chang, J. C.; Kovtun, O.; McBride, J. R.; Tomlinson, I. D. Biocompatible

- Quantum Dots for Biological Applications. *Chem. Biol.* **2011**, *18* (1), 10–24.
- (38) Goldman, E. R.; Balighian, E. D.; Mattoussi, H.; Kuno, M. K.; Mauro, J. M.; Tran, P. T.; Anderson, G. P. Avidin: A Natural Bridge for Quantum Dot-Antibody Conjugates. *J. Am. Chem. Soc.* **2002**, *124* (22), 6378–6382.
- (39) Lee, J.; Choi, Y.; Kim, K.; Hong, S.; Park, H. Y.; Lee, T.; Cheon, G. J.; Song, R. Characterization and Cancer Cell Specific Binding Properties of Anti-EGFR Antibody Conjugated Quantum Dots. *Bioconjug. Chem.* **2010**, *21* (5), 940–946.
- (40) (No Title) https://images.novusbio.com/design/BR_ICCguide.pdf (accessed Mar 25, 2021).
- (41) Peckys, D. B.; Quint, C.; Jonge, N. de. Determining the Efficiency of Single Molecule Quantum Dot Labeling of HER2 in Breast Cancer Cells. *Nano Lett.* **2020**, *23*, 31.
- (42) Rakovich, T. Y.; Mahfoud, O. K.; Mohamed, B. M.; Prina-Mello, A.; Crosbie-Staunton, K.; Van Den Broeck, T.; De Kimpe, L.; Sukhanova, A.; Baty, D.; Rakovich, A.; Maier, S. A.; Alves, F.; Nauwelaers, F.; Nabiev, I.; Chames, P.; Volkov, Y. Highly Sensitive Single Domain Antibody-Quantum Dot Conjugates for Detection of HER2 Biomarker in Lung and Breast Cancer Cells. *ACS Nano* **2014**, *8* (6), 5682–5695.
- (43) Sweeney, E.; Ward, T. H.; Gray, N.; Womack, C.; Jayson, G.; Hughes, A.; Dive, C.; Byers, R. Quantitative Multiplexed Quantum Dot Immunohistochemistry. *Biochem. Biophys. Res. Commun.* **2008**, *374* (2), 181–186.
- (44) Kwon, S.; Cho, C. H.; Lee, E. S.; Park, J. K. Automated Measurement of Multiple Cancer Biomarkers Using Quantum-Dot-Based Microfluidic Immunohistochemistry. *Anal. Chem.* **2015**, *87* (8), 4177–4183.
- (45) Tholouli, E.; Hoyland, J. A.; Di Vizio, D.; O’Connell, F.; MacDermott, S. A.; Twomey, D.; Levenson, R.; Yin, J. A. L.; Golub, T. R.; Loda, M.; Byers, R. Imaging of Multiple mRNA Targets Using Quantum Dot Based in Situ Hybridization and Spectral Deconvolution in Clinical Biopsies. *Biochem. Biophys. Res. Commun.* **2006**, *348* (2), 628–636.
- (46) Chattopadhyay, P. K.; Price, D. A.; Harper, T. F.; Betts, M. R.; Yu, J.; Gostick, E.; Perfetto, S. P.; Goepfert, P.; Koup, R. A.; De Rosa, S. C.; Bruchez, M. P.; Roederer, M. Quantum Dot Semiconductor Nanocrystals for Immunophenotyping by Polychromatic Flow Cytometry. *Nat. Med.* **2006**, *12* (8), 972–977.
- (47) Chattopadhyay, P. K. *Quantum Dot Technology in Flow Cytometry*, Second Edi.; Elsevier Inc., 2011; Vol. 102.

- (48) Harrison, C. Coronavirus Puts Drug Repurposing on the Fast Track. *Nat. Biotechnol.* **2020**, *38* (4), 379–381.
- (49) Yang, T.; Wang, Y. C.; Shen, C. F.; Cheng, C. M. Point-of-Care RNA-Based Diagnostic Device for Covid-19. *Diagnostics* **2020**, *10* (3), 9–11.
- (50) Hoffman, T.; Nissen, K.; Krambrich, J.; Rönnberg, B.; Akaberi, D.; Esmaeilzadeh, M.; Salaneck, E.; Lindahl, J.; Lundkvist, Å. Evaluation of a COVID-19 IgM and IgG Rapid Test; an Efficient Tool for Assessment of Past Exposure to SARS-CoV-2. *Infect. Ecol. Epidemiol.* **2020**, *10* (1), 1754538.
- (51) Chen, X.; Mei, Q.; Yu, L.; Ge, H.; Yue, J.; Zhang, K.; Hayat, T.; Alsaedi, A.; Wang, S. Rapid and On-Site Detection of Uranyl Ions via Ratiometric Fluorescence Signals Based on a Smartphone Platform. *ACS Appl. Mater. Interfaces* **2018**, *10* (49), 42225–42232.
- (52) Zhou, Y.; Huang, X.; Liu, C.; Zhang, R.; Gu, X.; Guan, G.; Jiang, C.; Zhang, L.; Du, S.; Liu, B.; Han, M. Y.; Zhang, Z. Color-Multiplexing-Based Fluorescent Test Paper: Dosage-Sensitive Visualization of Arsenic(III) with Discernable Scale as Low as 5 Ppb. *Anal. Chem.* **2016**, *88* (12), 6105–6109.
- (53) Shyam, K. U.; Jeong, H. N.; Oh, M. J.; Kim, C. S.; Kim, W. S. Development of a Lateral Flow Immuno-Chromatic Strip Assay for the Detection of Nervous Necrosis Virus (NNV, RGNNV Genotype). *Aquaculture* **2020**, *520* (November 2019), 734944.
- (54) Liu, J.; Yu, Q.; Zhao, G.; Dou, W. A Novel Immunochromatographic Assay Using Ultramarine Blue Particles as Visible Label for Quantitative Detection of Hepatitis B Virus Surface Antigen. *Anal. Chim. Acta* **2020**, *1098*, 140–147.
- (55) Liu, J.; Yu, Q.; Zhao, G.; Dou, W. A Au@Pt Bimetallic Nanoparticle and Blue Silica Nanoparticle Nanocomposite as a Probe of Immunochromatographic Assay for HBsAg Detection. *Anal. Methods* **2019**, *11* (48), 6103–6110.
- (56) Lu, L.; Yu, J.; Liu, X.; Yang, X.; Zhou, Z.; Jin, Q.; Xiao, R.; Wang, C. Rapid, Quantitative and Ultra-Sensitive Detection of Cancer Biomarker by a SERRS-Based Lateral Flow Immunoassay Using Bovine Serum Albumin Coated Au Nanorods. *RSC Adv.* **2019**, *10* (1), 271–281.
- (57) Chen, J.; Meng, H. M.; An, Y.; Liu, J.; Yang, R.; Qu, L.; Li, Z. A Fluorescent Nanosphere-Based Immunochromatography Test Strip for Ultrasensitive and Point-of-Care Detection of Tetanus Antibody in Human Serum. *Anal. Bioanal. Chem.* **2020**, *412* (5), 1151–1158.
- (58) Wu, M.; Zhang, X.; Wu, R.; Wang, G.; Li, J.; Chai, Y.; Shen, H.; Li, L. S. Sensitive and

- Quantitative Determination of Cardiac Troponin I Based on Silica-Encapsulated CdSe/ZnS Quantum Dots and a Fluorescence Lateral Flow Immunoassay. *Anal. Lett.* **2020**, *0* (0), 1–17.
- (59) Wang, C.; Shen, W.; Rong, Z.; Liu, X.; Gu, B.; Xiao, R.; Wang, S. Layer-by-Layer Assembly of Magnetic-Core Dual Quantum Dot-Shell Nanocomposites for Fluorescence Lateral Flow Detection of Bacteria. *Nanoscale* **2020**, *12* (2), 795–807.
- (60) Rong, Z.; Bai, Z.; Li, J.; Tang, H.; Shen, T.; Wang, Q.; Wang, C.; Xiao, R.; Wang, S. Dual-Color Magnetic-Quantum Dot Nanobeads as Versatile Fluorescent Probes in Test Strip for Simultaneous Point-of-Care Detection of Free and Complexed Prostate-Specific Antigen. *Biosens. Bioelectron.* **2019**, *145* (September), 111719.
- (61) Xu, L. Di; Zhang, Q.; Ding, S. N.; Xu, J. J.; Chen, H. Y. Ultrasensitive Detection of Severe Fever with Thrombocytopenia Syndrome Virus Based on Immunofluorescent Carbon Dots/SiO₂ Nanosphere-Based Lateral Flow Assay. *ACS Omega* **2019**, *4* (25), 21431–21438.
- (62) Huang, D.; Ying, H.; Jiang, D.; Liu, F.; Tian, Y.; Du, C.; Zhang, L.; Pu, X. Rapid and Sensitive Detection of Interleukin-6 in Serum via Time-Resolved Lateral Flow Immunoassay. *Anal. Biochem.* **2020**, *588* (August 2019), 113468.
- (63) Rajendran, V. K.; Bakthavathsalam, P.; Bergquist, P. L.; Sunna, A. Smartphone Detection of Antibiotic Resistance Using Convective PCR and a Lateral Flow Assay. *Sensors Actuators B Chem.* **2019**, *298* (July), 126849.
- (64) Ivanov, A. V.; Safenkova, I. V.; Zherdev, A. V.; Dzantiev, B. B. Nucleic Acid Lateral Flow Assay with Recombinase Polymerase Amplification: Solutions for Highly Sensitive Detection of RNA Virus. *Talanta* **2020**, *210* (December 2019), 120616.
- (65) Qie, Z.; Yan, W.; Gao, Z.; Meng, W.; Xiao, R.; Wang, S. An Anti-BSA Antibody-Based Immunochromatographic Assay for Chloramphenicol and Aflatoxin M1 by Using Carboxy-Modified CdSe/ZnS Core–Shell Nanoparticles as Label. *Microchim. Acta* **2020**, *187* (1), 1–8.
- (66) Li, R.; Meng, C.; Wen, Y.; Fu, W.; He, P. Fluorometric Lateral Flow Immunoassay for Simultaneous Determination of Three Mycotoxins (Aflatoxin B1, Zearalenone and Deoxynivalenol) Using Quantum Dot Microbeads. *Microchim. Acta* **2019**, *186* (12).
- (67) Yan, J. X.; Hu, W. J.; You, K. H.; Ma, Z. E.; Xu, Y.; Li, Y. P.; He, Q. H. Biosynthetic Mycotoxin Conjugate Mimetics-Mediated Green Strategy for Multiplex Mycotoxin Immunochromatographic Assay. *J. Agric. Food Chem.* **2020**, *68* (7), 2193–2200.
- (68) Wang, Z.; Wu, X.; Liu, L.; Xu, L.; Kuang, H.; Xu, C. Rapid and Sensitive Detection of

- Diclazuril in Chicken Samples Using a Gold Nanoparticle-Based Lateral-Flow Strip. *Food Chem.* **2020**, *312* (December 2019), 126116.
- (69) Chao, M.; Liu, L.; Song, S.; Wu, X.; Kuang, H. Development of a Gold Nanoparticle-Based Strip Assay for Detection of Clopidol in the Chicken. *Food Agric. Immunol.* **2020**, *31* (1), 489–500.
- (70) Fadlalla, M. H.; Ling, S.; Wang, R.; Li, X.; Yuan, J.; Xiao, S.; Wang, K.; Tang, S.; Elsir, H.; Wang, S. Development of ELISA and Lateral Flow Immunoassays for Ochratoxins (OTA and OTB) Detection Based on Monoclonal Antibody. *Front. Cell. Infect. Microbiol.* **2020**, *10* (March), 1–10.
- (71) Zhang, B.; Yang, X.; Liu, X.; Li, J.; Wang, C.; Wang, S. Polyethyleneimine-Interlayered Silica-Core Quantum Dot-Shell Nanocomposites for Sensitive Detection of: Salmonella Typhimurium via a Lateral Flow Immunoassay. *RSC Adv.* **2020**, *10* (5), 2483–2489.
- (72) Vasimalai, N.; Fernández-Argüelles, M. T.; Espiña, B. Detection of Sulfide Using Mercapto Tetrazine-Protected Fluorescent Gold Nanodots: Preparation of Paper-Based Testing Kit for On-Site Monitoring. *ACS Appl. Mater. Interfaces* **2018**, *10* (2), 1634–1645.
- (73) Yu, X.; Yang, L.; Zhao, T.; Zhang, R.; Yang, L.; Jiang, C.; Zhao, J.; Liu, B.; Zhang, Z. Multicolorful Ratiometric-Fluorescent Test Paper for Determination of Fluoride Ions in Environmental Water. *RSC Adv.* **2017**, *7* (84), 53379–53384.
- (74) Lan, J.; Sun, W.; Chen, L.; Zhou, H.; Fan, Y.; Diao, X.; Wang, B.; Zhao, H. Simultaneous and Rapid Detection of Carbofuran and 3-Hydroxy-Carbofuran in Water Samples and Pesticide Preparations Using Lateral-Flow Immunochromatographic Assay. *Food Agric. Immunol.* **2020**, *31* (1), 165–175.
- (75) Wang, J.; Meng, H. M.; Chen, J.; Liu, J.; Zhang, L.; Qu, L.; Li, Z.; Lin, Y. Quantum Dot-Based Lateral Flow Test Strips for Highly Sensitive Detection of the Tetanus Antibody. *ACS Omega* **2019**, *4* (4), 6789–6795.
- (76) Hu, J.; Zhang, Z. L.; Wen, C. Y.; Tang, M.; Wu, L. L.; Liu, C.; Zhu, L.; Pang, D. W. Sensitive and Quantitative Detection of C-Reaction Protein Based on Immunofluorescent Nanospheres Coupled with Lateral Flow Test Strip. *Anal. Chem.* **2016**, *88* (12), 6577–6584.
- (77) Fang, C. C.; Chou, C. C.; Yang, Y. Q.; Wei-Kai, T.; Wang, Y. T.; Chan, Y. H. Multiplexed Detection of Tumor Markers with Multicolor Polymer Dot-Based Immunochromatography Test Strip. *Anal. Chem.* **2018**, *90* (3), 2134–2140.

- (78) Duan, H.; Li, Y.; Shao, Y.; Huang, X.; Xiong, Y. Multicolor Quantum Dot Nanobeads for Simultaneous Multiplex Immunochromatographic Detection of Mycotoxins in Maize. *Sensors Actuators, B Chem.* **2019**, *291* (March), 411–417.
- (79) Danthanarayana, A. N.; Finley, E.; Vu, B.; Kourentzi, K.; Willson, R. C.; Brgoch, J. A Multicolor Multiplex Lateral Flow Assay for High-Sensitivity Analyte Detection Using Persistent Luminescent Nanophosphors. *Anal. Methods* **2020**, *12* (3), 272–280.
- (80) Li, Y.; Lin, F.; Sun, L.; Huang, A.; Chen, J.; Hao, G.; Yuan, X.; Zhang, H.; Su, S. Detection of Cyprinid Herpesvirus 2 by Loop-Mediated Isothermal Amplification in Combination with a Lateral Flow Dipstick. *Mol. Cell. Probes* **2020**, *50* (December 2019), 101507.
- (81) Bai, X.; Ma, X.; Li, M.; Li, X.; Fan, G.; Zhang, R.; Wang, R.; Duan, Q.; Shen, X.; Xie, Y.; Rong, X. Field Applicable Detection of Hepatitis B Virus Using Internal Controlled Duplex Recombinase-Aided Amplification Assay and Lateral Flow Dipstick Assay. *J. Med. Virol.* **2020**, No. December 2019, 1–10.
- (82) Suntornsuk, W.; Suntornsuk, L. Recent Applications of Paper-Based Point-of-Care Devices for Biomarker Detection. *Electrophoresis* **2020**, *41* (5–6), 287–305.
- (83) Phillips, E. A.; Moehling, T. J.; Ejendal, K. F. K.; Hoilett, O. S.; Byers, K. M.; Basing, L. A.; Jankowski, L. A.; Bennett, J. B.; Lin, L. K.; Stanciu, L. A.; Linnes, J. C. Microfluidic Rapid and Autonomous Analytical Device (MicroRAAD) to Detect HIV from Whole Blood Samples. *Lab Chip* **2019**, *19* (20), 3375–3386.
- (84) Liu, D.; Zhu, Y.; Li, N.; Lu, Y.; Cheng, J.; Xu, Y. A Portable Microfluidic Analyzer for Integrated Bacterial Detection Using Visible Loop-Mediated Amplification. *Sensors Actuators, B Chem.* **2020**, *310* (November 2019), 127834.
- (85) Kung, C. Te; Hou, C. Y.; Wang, Y. N.; Fu, L. M. Microfluidic Paper-Based Analytical Devices for Environmental Analysis of Soil, Air, Ecology and River Water. *Sensors Actuators, B Chem.* **2019**, *301* (July), 126855.
- (86) Guan, Y.; Sun, B. Detection and Extraction of Heavy Metal Ions Using Paper-Based Analytical Devices Fabricated via Atom Stamp Printing. *Microsystems Nanoeng.* **2020**, *6* (1).
- (87) Paterson, A. S.; Raja, B.; Mandadi, V.; Townsend, B.; Lee, M.; Buell, A.; Vu, B.; Brgoch, J.; Willson, R. C. A Low-Cost Smartphone-Based Platform for Highly Sensitive Point-of-Care Testing with Persistent Luminescent Phosphors. *Lab Chip* **2017**, *17* (6), 1051–1059.
- (88) Gupta, R.; Peveler, W. J.; Lix, K.; Algar, W. R. Comparison of Semiconducting Polymer Dots

- and Semiconductor Quantum Dots for Smartphone-Based Fluorescence Assays. *Anal. Chem.* **2019**, *91*, 10955–10960.
- (89) Ma, Y. D.; Li, K. H.; Chen, Y. H.; Lee, Y. M.; Chou, S. T.; Lai, Y. Y.; Huang, P. C.; Ma, H. P.; Lee, G. Bin. A Sample-to-Answer, Portable Platform for Rapid Detection of Pathogens with a Smartphone Interface. *Lab Chip* **2019**, *19* (22), 3804–3814.
- (90) Joung, H. A.; Ballard, Z. S.; Ma, A.; Tseng, D. K.; Teshome, H.; Burakowski, S.; Garner, O. B.; Di Carlo, D.; Ozcan, A. Paper-Based Multiplexed Vertical Flow Assay for Point-of-Care Testing. *Lab Chip* **2019**, *19* (6), 1027–1034.
- (91) Ballard, Z.; Bazargan, S.; Jung, D.; Sathianathan, S.; Clemens, A.; Shir, D.; Al-Hashimi, S.; Ozcan, A. Contact Lens-Based Lysozyme Detection in Tear Using a Mobile Sensor. *Lab Chip* **2020**, *20* (8), 1493–1502.
- (92) Feng, S.; Tseng, D.; Di Carlo, D.; Garner, O. B.; Ozcan, A. High-Throughput and Automated Diagnosis of Antimicrobial Resistance Using a Cost-Effective Cellphone-Based Micro-Plate Reader. *Sci. Rep.* **2016**, *6* (August), 1–9.
- (93) Ludwig, S. K. J.; Tokarski, C.; Lang, S. N.; Van Ginkel, L. A.; Zhu, H.; Ozcan, A.; Nielen, M. W. F. Calling Biomarkers in Milk Using a Protein Microarray on Your Smartphone. *PLoS One* **2015**, *10* (8), 1–13.
- (94) Berg, B.; Cortazar, B.; Tseng, D.; Ozkan, H.; Feng, S.; Wei, Q.; Chan, R. Y. L.; Burbano, J.; Farooqui, Q.; Lewinski, M.; Di Carlo, D.; Garner, O. B.; Ozcan, A. Cellphone-Based Hand-Held Microplate Reader for Point-of-Care Testing of Enzyme-Linked Immunosorbent Assays. *ACS Nano* **2015**, *9* (8), 7857–7866.
- (95) Giavazzi, F.; Salina, M.; Ceccarello, E.; Ilacqua, A.; Damin, F.; Sola, L.; Chiari, M.; Chini, B.; Cerbino, R.; Bellini, T.; Buscaglia, M. A Fast and Simple Label-Free Immunoassay Based on a Smartphone. *Biosens. Bioelectron.* **2014**, *58*, 395–402.
- (96) Switz, N. A.; D’Ambrosio, M. V.; Fletcher, D. A. Low-Cost Mobile Phone Microscopy with a Reversed Mobile Phone Camera Lens. *PLoS One* **2014**, *9* (5).
- (97) Jung, D.; Choi, J. H.; Kim, S.; Ryu, S.; Lee, W.; Lee, J. S.; Joo, C. Smartphone-Based Multi-Contrast Microscope Using Color-Multiplexed Illumination. *Sci. Rep.* **2017**, *7* (1), 1–10.
- (98) Breslauer, D. N.; Maamari, R. N.; Switz, N. A.; Lam, W. A.; Fletcher, D. A. Mobile Phone Based Clinical Microscopy for Global Health Applications. *PLoS One* **2009**, *4* (7), 1–7.
- (99) Wei, Q.; Luo, W.; Chiang, S.; Kappel, T.; Mejia, C.; Tseng, D.; Chan, R. Y. L.; Yan, E.; Qi,

- H.; Shabbir, F.; Ozkan, H.; Feng, S.; Ozcan, A. Imaging and Sizing of Single DNA Molecules on a Mobile Phone. *ACS Nano* **2014**, *8* (12), 12725–12733.
- (100) Wei, Q.; Qi, H.; Luo, W.; Tseng, D.; Ki, S. J.; Wan, Z.; Gorocs, Z.; Bentolila, L. A.; Wu, T. T.; Sun, R.; Ozcan, A. Fluorescent Imaging of Single Nanoparticles and Viruses on a Smart Phone. *ACS Nano*. 2013, pp 9147–9155.
- (101) Long, K. D.; Woodburn, E. V.; Le, H. M.; Shah, U. K.; Lumetta, S. S.; Cunningham, B. T. Multimode Smartphone Biosensing: The Transmission, Reflection, and Intensity Spectral (TRI)-Analyzer. *Lab Chip* **2017**, *17* (19), 3246–3257.
- (102) Kong, L.; Gan, Y.; Liang, T.; Zhong, L.; Pan, Y.; Kirsanov, D.; Legin, A.; Wan, H.; Wang, P. A Novel Smartphone-Based CD-Spectrometer for High Sensitive and Cost-Effective Colorimetric Detection of Ascorbic Acid. *Anal. Chim. Acta* **2020**, *1093*, 150–159.
- (103) Hossain, M. A.; Canning, J.; Yu, Z. Fluorescence-Based Determination of Olive Oil Quality Using an Endoscopic Smart Mobile Spectrofluorimeter. *IEEE Sens. J.* **2020**, *20* (8), 4156–4163.
- (104) Jian, D.; Wang, B.; Huang, H.; Meng, X.; Liu, C.; Xue, L.; Liu, F.; Wang, S. Sunlight Based Handheld Smartphone Spectrometer. *Biosens. Bioelectron.* **2019**, *143* (August), 111632.
- (105) Petryayeva, E.; Algar, W. R. Toward Point-of-Care Diagnostics with Consumer Electronic Devices: The Expanding Role of Nanoparticles. *RSC Adv.* **2015**, *5* (28), 22256–22282.
- (106) Wei, Q.; Qi, H.; Luo, W.; Tseng, D.; Ki, S. J.; Wan, Z.; Göröcs, Z.; Bentolila, L. A.; Wu, T. T.; Sun, R.; Ozcan, A. Fluorescent Imaging of Single Nanoparticles and Viruses on a Smart Phone. *ACS Nano* **2013**, *7* (10), 9147–9155.
- (107) Mutlu, A. Y.; Kiliç, V.; Özdemir, G. K.; Bayram, A.; Horzum, N.; Solmaz, M. E. Smartphone-Based Colorimetric Detection: Via Machine Learning. *Analyst* **2017**, *142* (13), 2434–2441.
- (108) Koydemir, H. C.; Gorocs, Z.; Tseng, D.; Cortazar, B.; Feng, S.; Chan, R. Y. L.; Burbano, J.; McLeod, E.; Ozcan, A. Rapid Imaging, Detection and Quantification of Giardia Lambliia Cysts Using Mobile-Phone Based Fluorescent Microscopy and Machine Learning. *Lab Chip* **2015**, *15* (5), 1284–1293.
- (109) Igoe, D.; Parisi, A. V. Characterization of the Corrosion of Iron Using a Smartphone Camera. *Instrum. Sci. Technol.* **2016**, *44* (2), 139–147.
- (110) Burggraaff, O.; Schmidt, N.; Zamorano, J.; Pauly, K.; Pascual, S.; Tapia, C.; Spyrakos, E.; Snik, F. Standardized Spectral and Radiometric Calibration of Consumer Cameras. *Opt.*

Express **2019**, 27 (14), 19075.

- (111) Adan, A.; Alizada, G.; Kiraz, Y.; Baran, Y.; Nalbant, A. Flow Cytometry: Basic Principles and Applications. *Crit. Rev. Biotechnol.* **2017**, 37 (2), 163–176.
- (112) Flow Cytometry - Semrock <https://www.semrock.com/flow-cytometry.aspx> (accessed May 17, 2021).
- (113) Büscher, M. Flow Cytometry Instrumentation – An Overview. *Curr. Protoc. Cytom.* **2019**, 87 (1), 1–16.
- (114) Zhang, Y.; Yu, J.; Gallina, M. E.; Sun, W.; Rong, Y.; Chiu, D. T. Highly Luminescent, Fluorinated Semiconducting Polymer Dots for Cellular Imaging and Analysis. *Chem. Commun.* **2013**, 49 (74), 8256–8258.
- (115) Saeys, Y.; Van Gassen, S.; Lambrecht, B. N. Computational Flow Cytometry: Helping to Make Sense of High-Dimensional Immunology Data. *Nat. Rev. Immunol.* **2016**, 16 (7), 449–462.
- (116) Whitesides, G. M. The Origins and the Future of Microfluidics. *Nature* **2006**, 442 (7101), 368–373.
- (117) Torino, S.; Corrado, B.; Iodice, M.; Coppola, G. Pdms-Based Microfluidic Devices for Cell Culture. *Inventions* **2018**, 3 (3), 1–14.
- (118) Kamei, K. ichiro; Mashimo, Y.; Koyama, Y.; Fockenber, C.; Nakashima, M.; Nakajima, M.; Li, J.; Chen, Y. 3D Printing of Soft Lithography Mold for Rapid Production of Polydimethylsiloxane-Based Microfluidic Devices for Cell Stimulation with Concentration Gradients. *Biomed. Microdevices* **2015**, 17 (2).
- (119) Halldorsson, S.; Lucumi, E.; Gómez-Sjöberg, R.; Fleming, R. M. T. Advantages and Challenges of Microfluidic Cell Culture in Polydimethylsiloxane Devices. *Biosens. Bioelectron.* **2015**, 63, 218–231.
- (120) Yu, L.; Huang, H.; Dong, X.; Wu, D.; Qin, J.; Lin, B. Simple, Fast and High-Throughput Single-Cell Analysis on PDMS Microfluidic Chips. *Electrophoresis* **2008**, 29 (24), 5055–5060.
- (121) Kellogg, R. A.; Gómez-Sjöberg, R.; Leyrat, A. A.; Tay, S. High-Throughput Microfluidic Single-Cell Analysis Pipeline for Studies of Signaling Dynamics. *Nat. Protoc.* **2014**, 9 (7), 1713–1726.
- (122) Ginn, B. T.; Steinbock, O. Polymer Surface Modification Using Microwave-Oven-Generated Plasma. *Langmuir* **2003**, 19 (19), 8117–8118.

- (123) Berdichevsky, Y.; Khandurina, J.; Guttman, A.; Lo, Y. H. UV/Ozone Modification of Poly(Dimethylsiloxane) Microfluidic Channels. *Sensors Actuators, B Chem.* **2004**, *97* (2–3), 402–408.
- (124) Slentz, B. E.; Penner, N. A.; Lugowska, E.; Regnier, F. Nanoliter Capillary Electrochromatography Columns Based on Collocated Monolithic Support Structures Molded in Poly(Dimethyl Siloxane). *Electrophoresis* **2001**, *22* (17), 3736–3743.
- (125) Lee, D.; Yang, S. Surface Modification of PDMS by Atmospheric-Pressure Plasma-Enhanced Chemical Vapor Deposition and Analysis of Long-Lasting Surface Hydrophilicity. *Sensors Actuators, B Chem.* **2012**, *162* (1), 425–434.
- (126) Makamba, H.; Hsieh, Y. Y.; Sung, W. C.; Chen, S. H. Stable Permanently Hydrophilic Protein-Resistant Thin-Film Coatings on Poly(Dimethylsiloxane) Substrates by Electrostatic Self-Assembly and Chemical Cross-Linking. *Anal. Chem.* **2005**, *77* (13), 3971–3978.
- (127) Zhou, J.; Khodakov, D. A.; Ellis, A. V.; Voelcker, N. H. Surface Modification for PDMS-Based Microfluidic Devices. *Electrophoresis* **2012**, *33* (1), 89–104.
- (128) Bodas, D.; Khan-Malek, C. Hydrophilization and Hydrophobic Recovery of PDMS by Oxygen Plasma and Chemical Treatment-An SEM Investigation. *Sensors Actuators, B Chem.* **2007**, *123* (1), 368–373.
- (129) Almutairi, Z.; Ren, C. L.; Simon, L. Evaluation of Polydimethylsiloxane (PDMS) Surface Modification Approaches for Microfluidic Applications. *Colloids Surfaces A Physicochem. Eng. Asp.* **2012**, *415*, 406–412.
- (130) Yeh, P. Y.; Rossi, N. A. A.; Kizhakkedathu, J. N.; Chiao, M. A Silicone-Based Microfluidic Chip Grafted with Carboxyl Functionalized Hyperbranched Polyglycerols for Selective Protein Capture. *Microfluid. Nanofluidics* **2010**, *9* (2–3), 199–209.
- (131) Sia, S. K.; Whitesides, G. M. Microfluidic Devices Fabricated in Poly(Dimethylsiloxane) for Biological Studies. *Electrophoresis* **2003**, *24* (21), 3563–3576.
- (132) The human cell in cell line - The Human Protein Atlas https://www.proteinatlas.org/humanproteome/cell/cell+line#a_diversity_of_cell_lines (accessed May 17, 2021).
- (133) Hanash, S. Integrated Global Profiling of Cancer. *Nat. Rev. Cancer* **2004**, *4* (8), 638–644.
- (134) Rusnak, D. W.; Alligood, K. J.; Mullin, R. J.; Spehar, G. M.; Arenas-Elliott, C.; Martin, A. M.; Degenhardt, Y.; Rudolph, S. K.; Haws, T. F.; Hudson-Curtis, B. L.; Gilmer, T. M.

- Assessment of Epidermal Growth Factor Receptor (EGFR, ErbB1) and HER2 (ErbB2) Protein Expression Levels and Response to Lapatinib (Tykerb®, GW572016) in an Expanded Panel of Human Normal and Tumour Cell Lines. *Cell Prolif.* **2007**, *40* (4), 580–594.
- (135) Walsh, M. D.; Luckie, S. M.; Cummings, M. C.; Antalis, T. M.; McGuckin, M. A. Heterogeneity of MUC1 Expression by Human Breast Carcinoma Cell Lines in Vivo and in Vitro. *Breast Cancer Res. Treat.* **1999**, *58* (3), 255–266.
- (136) Goode, G.; Gunda, V.; Chaika, N. V.; Purohit, V.; Yu, F.; Singh, P. K. MUC1 Facilitates Metabolomic Reprogramming in Triple-Negative Breast Cancer. *PLoS One* **2017**, *12* (5), e0176820.
- (137) Poudineh, M.; Sargent, E. H.; Pantel, K.; Kelley, S. O. Profiling Circulating Tumour Cells and Other Biomarkers of Invasive Cancers. *Nat. Biomed. Eng.* **2018**, *2* (2), 72–84.
- (138) Yin, H.; Marshall, D. Microfluidics for Single Cell Analysis. *Curr. Opin. Biotechnol.* **2012**, *23* (1), 110–119.
- (139) Liu, L.; Yang, H.; Men, D.; Wang, M.; Gao, X.; Zhang, T.; Chen, D.; Xue, C.; Wang, Y.; Wang, J.; Chen, J. Development of Microfluidic Platform Capable of High-Throughput Absolute Quantification of Single-Cell Multiple Intracellular Proteins from Tumor Cell Lines and Patient Tumor Samples. *Biosens. Bioelectron.* **2020**, *155* (February), 112097.
- (140) Yeo, T.; Tan, S. J.; Lim, C. L.; Lau, D. P. X.; Chua, Y. W.; Krisna, S. S.; Iyer, G.; Tan, G. S.; Lim, T. K. H.; Tan, D. S. W.; Lim, W. T.; Lim, C. T. Microfluidic Enrichment for the Single Cell Analysis of Circulating Tumor Cells. *Sci. Rep.* **2016**, *6* (February), 1–12.
- (141) Li, J. J.; Wang, Y. A.; Guo, W.; Keay, J. C.; Mishima, T. D.; Johnson, M. B.; Peng, X. Large-Scale Synthesis of Nearly Monodisperse CdSe/CdS Core/Shell Nanocrystals Using Air-Stable Reagents via Successive Ion Layer Adsorption and Reaction. *J. Am. Chem. Soc.* **2003**, *125* (41), 12567–12575.
- (142) William Yu, W.; Peng, X. *Formation of High-Quality CdS and Other II ± VI Semiconductor Nanocrystals in Noncoordinating Solvents: Tunable Reactivity of Monomers***; 2002; Vol. 41.
- (143) Darwish, G. H.; Asselin, J.; Tran, M. V.; Gupta, R.; Kim, H.; Boudreau, D.; Algar, W. R. Fully Self-Assembled Silica Nanoparticle-Semiconductor Quantum Dot Supra-Nanoparticles and Immunoconjugates for Enhanced Cellular Imaging by Microscopy and Smartphone Camera. *ACS Appl. Mater. Interfaces* **2020**, *12* (30), 33530–33540.
- (144) The Human Protein Atlas <https://www.proteinatlas.org/> (accessed May 17, 2021).

- (145) Akram, M.; Iqbal, M.; Daniyal, M.; Khan, A. U. Awareness and Current Knowledge of Breast Cancer. *Biological Research*. BioMed Central Ltd. 2017, p 33.
- (146) Wang, J.; Qin, Y.; Qin, H.; Liu, L.; Ding, S.; Teng, Y.; Ji, J.; Qiu, L.; Jiang, P. Simultaneous Detection of Assembly and Disassembly of Multivalent HA Tag and Anti-HA Antibody in Single in-Capillary Assay. *Electrophoresis* **2016**, *37* (15–16), 2163–2169.
- (147) Wang, H.; Sun, H.; Wei, H.; Xi, P.; Nie, S.; Ren, Q. Biocompatible Hyaluronic Acid Polymer-Coated Quantum Dots for CD44+ Cancer Cell-Targeted Imaging. *J. Nanoparticle Res.* **2014**, *16* (10), 1–13.
- (148) Susumu, K.; Field, L. D.; Oh, E.; Hunt, M.; Delehanty, J. B.; Palomo, V.; Dawson, P. E.; Huston, A. L.; Medintz, I. L. Purple-, Blue-, and Green-Emitting Multishell Alloyed Quantum Dots: Synthesis, Characterization, and Application for Ratiometric Extracellular PH Sensing. *Chem. Mater.* **2017**, *29* (17), 7330–7344.
- (149) Gupta, R.; Peveler, W. J.; Lix, K.; Algar, W. R. Comparison of Semiconducting Polymer Dots and Semiconductor Quantum Dots for Smartphone-Based Fluorescence Assays. *Anal. Chem.* **2019**, *91* (17), 10955–10960.
- (150) Zhang, H.; Chiao, • Mu. Anti-Fouling Coatings of Poly(Dimethylsiloxane) Devices for Biological and Biomedical Applications. *J. Med. Biol. Eng.*
- (151) Qin, Y.; Yang, X.; Zhang, J.; Cao, X. Developing a Non-Fouling Hybrid Microfluidic Device for Applications in Circulating Tumour Cell Detections. *Colloids Surfaces B Biointerfaces* **2017**, *151*, 39–46.
- (152) Qin, B.; Yan, J.; Li, W.; Yu, D.; Tang, L.; Dong, Z.; Loftis, K. A.; Ding, Z.; Cheng, J. Biomaterials Science Rsc.Li/Biomaterials-Science Eff Ective Reduction of Non-Specific Binding of Blood Cells in a Microfl Uidic Chip for Isolation of Rare Cancer Cells Effective Reduction of Non-Specific Binding of Blood Cells in a Microfluidic Chip for Isolation of Rare Cancer Cells †. *Cite this Biomater. Sci* **2018**, *6*, 2871.
- (153) Common Cell Culture Problems: Cell Clumping | Sigma-Aldrich <https://www.sigmaaldrich.com/technical-documents/articles/biology/cell-culture-troubleshooting-cell-clumping.html> (accessed May 19, 2021).
- (154) Cossarizza, A.; Chang, H. D.; Radbruch, A.; Akdis, M.; Andrä, I.; Annunziato, F.; Bacher, P.; Barnaba, V.; Battistini, L.; Bauer, W. M.; et al., Guidelines for the Use of Flow Cytometry and Cell Sorting in Immunological Studies. *Eur. J. Immunol.* **2017**, *47* (10), 1584–1797.

(155) Motion-Based Multiple Object Tracking - MATLAB & Simulink
<https://www.mathworks.com/help/vision/ug/motion-based-multiple-object-tracking.html>
(accessed May 20, 2021).

Appendices

The following appendices summarize the MATLAB-based data analysis of the smartphone videos obtained from the smartphone-based flow cytometer. A cell counting algorithm was coded to obtain the total cell counts and extract colour features from each labeled cell. A simple area correction was used to compensate for small aggregates of cells. A support-vector machine (SVM) model was used for classification of different cell lines. Appendix B shows the size analysis of the SiO₂@QD of different colours using NTA.

Appendix A MATLAB algorithms

A.1 Cell counting algorithm

Smartphone videos (Samsung Galaxy S8, mp4 file format) of fluorescently labeled cells were analyzed through a cell counting algorithm developed using the MATLAB R2019b computer vision toolbox. The frames extracted from the smartphone video (.mp4) for further analysis are JPEG files, which is a much smaller file size compared to RAW images, but still provides RGB values that are sufficient for further data analysis. Quantification and classification of different cancer cells were achieved according to the color of SiO₂@QD used for cell labeling. Each smartphone video was recorded under FHD mode at a frame rate of 30 frame per seconds (fps) with a resolution of 1920 × 1080 pixels. As shown in **Figure A. 1**, after the video frames were imported and read, the foreground detection extracted objects from the background. Cell counts were based on the number of reliable tracks.

The algorithm mainly included three main parts across four steps: detection (Step 1 and 2), tracking (Step 3), and classification (Step 4). These steps are described in detail below and summarized in **Figure A. 2**.

Step1 (read video):

Smartphone videos were imported and read frame by frame. Each frame was cropped to the relevant field of view (400 × 1920 pixels) and separated into three separate RGB color channels.

Step 2 (foreground detection):

Each video frame was converted to a binary image using the *vision.ForegroundDetector* function that compared a colour or grayscale video frame to a background model to determine which pixels were part of the foreground and which were part of the background. Small holes inside the detected object, which is noted as a *blob*, were filled up with an *imfill* operator. Noise or small objects other than cells were removed based on the minimum blob area set by the user. This process was repeated for every frame in the video. A blob analysis system was used to compute the properties of each visible object detected (*e.g.* blob areas, centroid, *etc.*) using the *vision.BlobAnalysis* function. The color coordinates

(RGB value) of each object was extracted with the *regionprops* operator from the separated RGB channels.

Step 3 (track assignment):

An array of tracks was initialized to represent the moving objects in the video and to store the characteristics of each object. The predicted location of an object in the next frame was computed using the *Kalman filter* function. This function predicts an object's future location and computes the Euclidean distance between the predicted centroid of the track and the centroid of the detection. Objects were then attributed to their corresponding tracks using Munkres' version of the Hungarian algorithm that computes the cost of assigning the N^{th} detection to the M^{th} track and finds the assignment that minimizes the total cost (Euclidean distance between the prediction and the detection). In the end, the function returned a matrix containing the indices of assigned tracks and detections, as well as the indices and detections that were not assigned. For detected objects that were invisible for too long, the track was deleted from the track array. The maximum number of frames in which a detected object is permitted to be invisible was adjustable by the user (set as 8 in the experiments). After discarding the lost tracks, all the reliable tracks were displayed in the video.

Step 4 (classification and export results):

The data for all reliable tracks were exported to a comma-separated value (.csv) file with the following data: track number, blob pixel area, and RGB pixel intensities. Mean RGB values were calculated for each track. When labeled cells had more than one colour, a threshold of RGB values was set in order to distinguish different colors and obtain cell counts based by colour. For cells labeled via TACs, a threshold for the ratio of Mean R and Mean B value was set to 1 to separate the red and blue objects. For cells labeled with SiO₂@(QD-CM-Dex)-antibody conjugates, a Linear SVM model was used to classify different colours (see **Appendix A.3**). A single-cell blob area threshold, set by the user (*vide infra*), as used to discard any tracked objects that were smaller than single cells. To take potential aggregates of cells into consideration, the blob area was divided by a user-defined area for a single cell (*vide infra*), with rounding to the nearest integer. Final cell counts were corrected by adding these integers together. More details will be discussed in the following section.

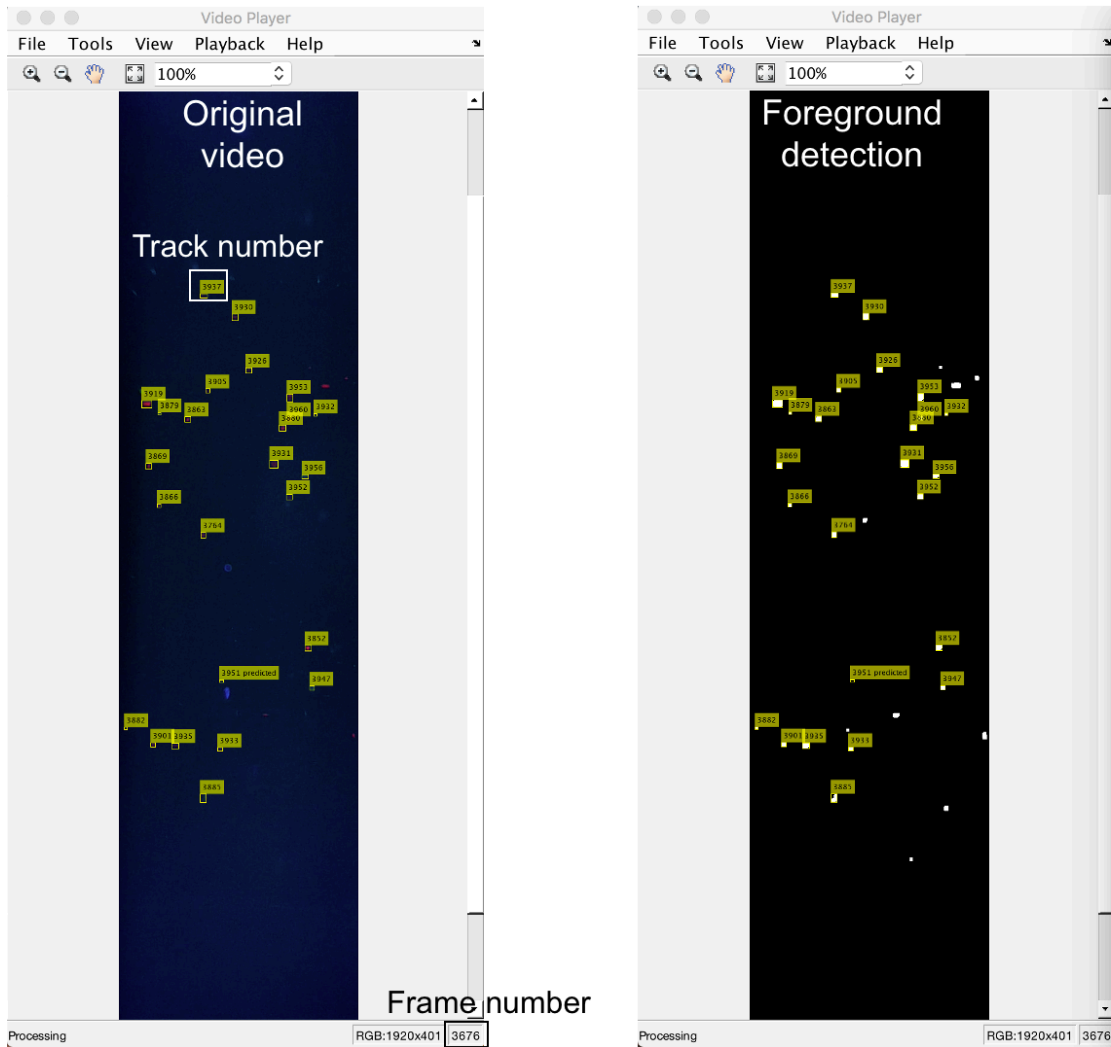


Figure A. 1 MATLAB analysis of a smartphone video. Left image: Original frame with the track number in a yellow box. Right image: the binary image obtained after foreground detection.

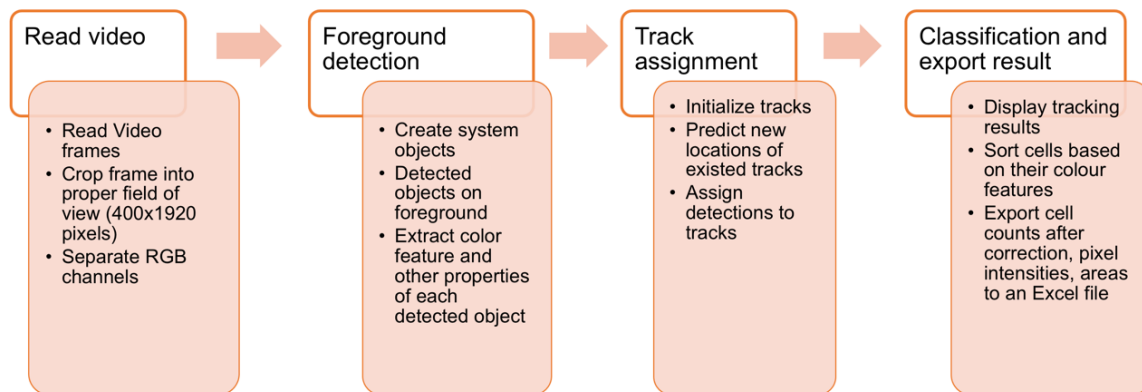


Figure A. 2 Workflow of MATLAB object-tracking algorithm.

A.2 Area-based correction for cell aggregates

Single-cell suspensions are critical for flow cytometry (FC) experiments. Likewise, with the smartphone-based FC, cell aggregates will cause inaccuracy to the final cell counts. Possible causes of cell clumping include cell lysis and DNA release, the presence of bivalent cations (*e.g.* Ca^{2+} , Mg^{2+}), high cell density during fixation, mycoplasma contamination, or improper handling.^{153,154} Sample preparation protocols have been reported to help reduce cell aggregation problems. These protocols include adding anti-clumping agents, using cation-free buffer, adding chelators such as EDTA, and using cell strainers.¹⁵³

Prior to cell labeling with $\text{SiO}_2@\text{QD}$ -antibody conjugates, a 40 μm cell strainer was used to minimize cell clumping. For experiments with TAC, the ratio between TAC complexes and $\text{SiO}_2@\text{QD}$ -Dex was optimized to minimize potential crosslinking of two cells through TACs. However, small cell aggregates (*e.g.* duplets, triplets, quadruplets) still appeared and had potential to affect the cell counting process, although video and data matching showed a majority of single cells. To mathematically correct for cell aggregates, the average area of each blob that was recorded during the object detection process was exported. A histogram of these areas was obtained through the *histogram* operation in MATLAB and fitted with a non-parametric method via the *Distribution Fitter* app (see **Figure A. 3**). From the histogram, an average area for a single cell was set as 102 (the highest peak in **Figure A. 3**) and then used to calculate the area ratio between a detected object and the average single cell for all the experiments. The area ratio was rounded to the nearest integer using the *round* operation. For example, if a detected object had an area of 220, it was identified as a double cell and counted as 2 cells. Any area ratio higher than 10 was discarded. Corrected cell counts were obtained by summing up the rounded area ratios for all detected objects.

The same process was conducted for DAPI stained MDA-MB-231 cells that were not labeled with SiO₂@(QD625-Dex) in the cell counting assay, and the single cell threshold was set to 77 for blue objects. As DAPI is a nuclear stain, the area of a single cell in this case was expected to be smaller.

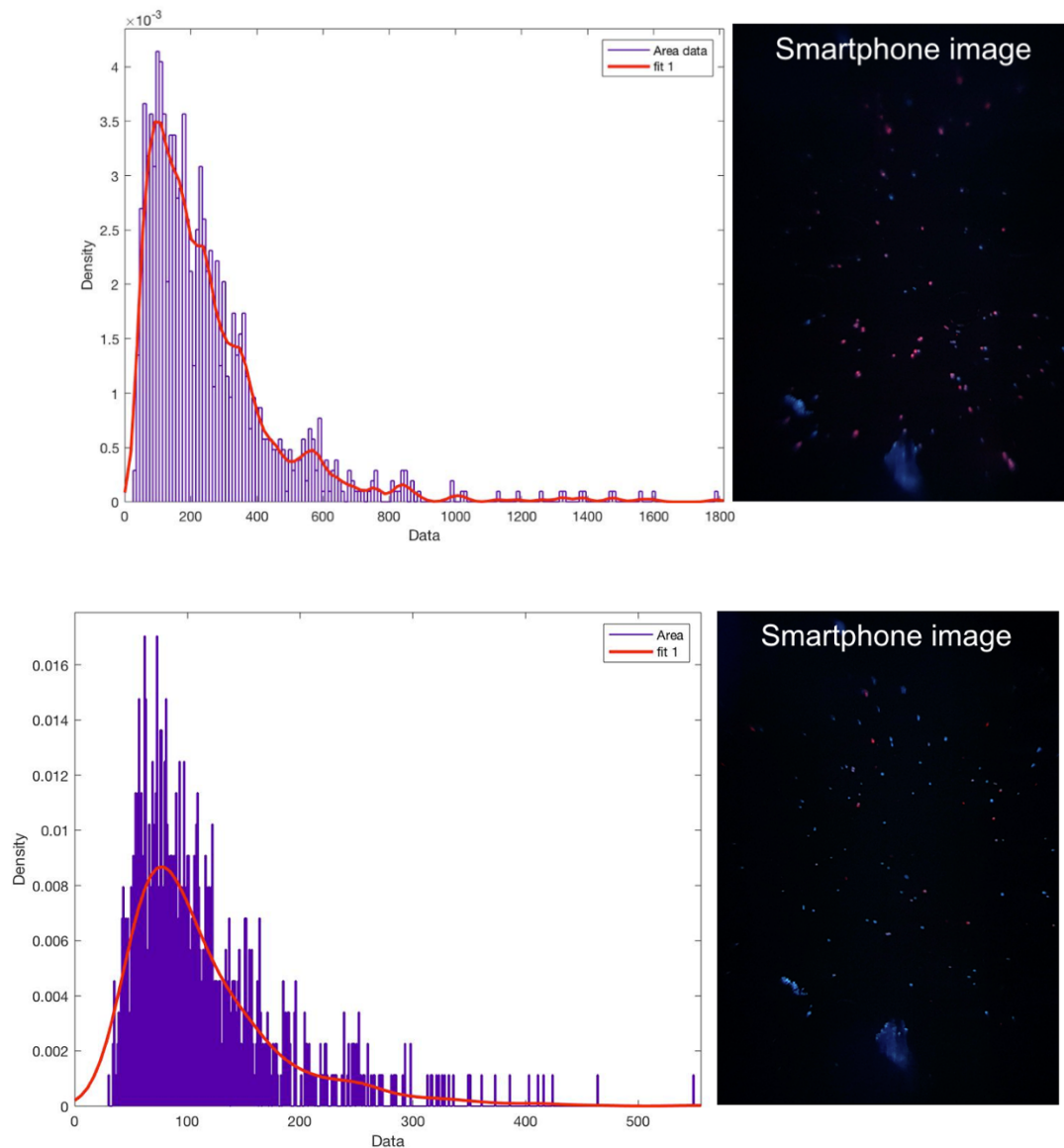


Figure A. 3 Non-parametric fitting of the histogram of area data exported from MATLAB cell counting algorithm: **(A)** majority of labeled SK-BR3 cells, peak at (102, 0.003529). **(B)** majority of unlabeled MDA-MB-231 cells, peak at (77, 0.008688). Bin rules for the histogram were set as “bins centered on integers”. A nonparametric fit (Kernel normal) was applied to the data with a bandwidth of 20.

A.3 Selective cell counting and classification with linear support vector machine (SVM)

model

Support vector machine (SVM) is a supervised machine learning algorithm widely used for classification problems. The goal of the algorithm is to find a hyperplane in an N -dimensional space (N is the number of features used) that can separate data sets into different classes. The margin represents the width of the section parallel to the separating hyperplane that does not include data points. (see **Figure A. 4**) In order to find the optimal hyperplane to best separate the data sets, the margin needs to be maximized. For the soft-margin SVM method, the algorithm will allow a few misclassification points in that region without changing the hyperplane. This condition is usually needed for real data analysis when there is an intersection of two classes.

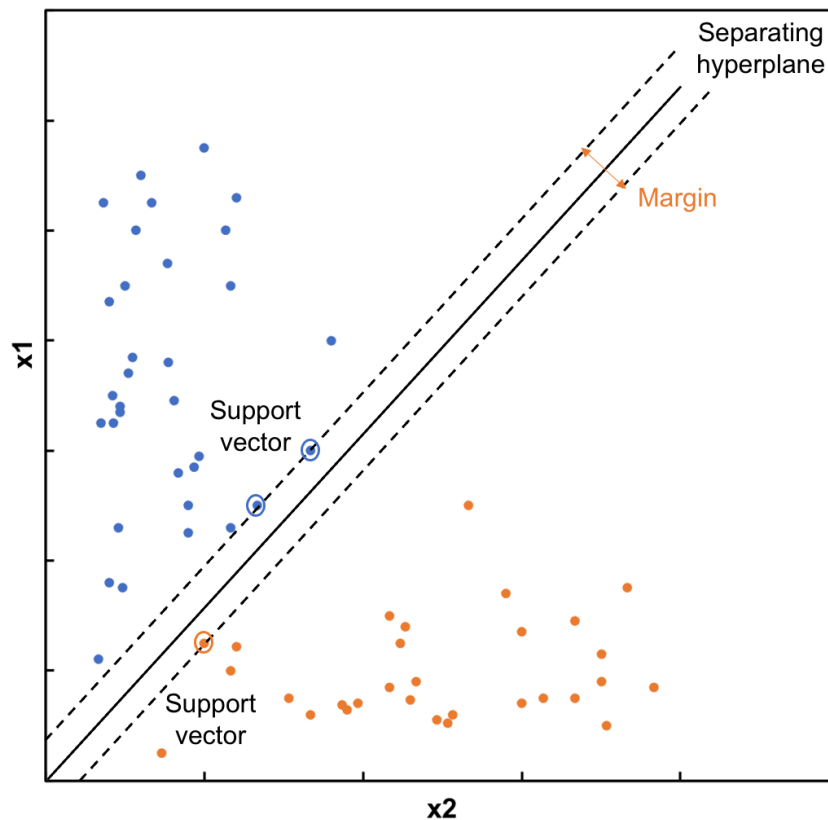


Figure A. 4 Illustration of support vector machine (SVM) model. The blue and orange points represent data sets classified into two classes by the algorithm.

An SVM model was used for classification of different cancer cell lines labeled with various colours of SiO₂@(QD-CM-Dex)-antibody conjugates. Color features extracted from the detected objects mentioned in **Section 3.7** were used as original data sets. The two predictors were the Mean R/Mean B ratio value and the Mean G/Mean B ratio value. SK-BR3 cells labeled with SiO₂@(QD540-CM-Dex)-anti-HER2 conjugate, MDA-MB-231 cells labeled with SiO₂@(QD650-CM-Dex)-anti-MUC1 conjugate and unlabeled cells were separately injected into the smartphone FC to generate three data sets with pre-determined categories. The data sets were imported to MATLAB and trained with *Classification Learner* app. Two Linear SVM models were then exported and used for classification of test samples. The Linear SVM(RG) model was trained with the first two data groups above, and the Linear SVM(RGN) model was trained with all three of the data groups above. Each test sample was a mixture of SK-BR3 and MDA-MB-231 cells incubated with a mixture of SiO₂@QD-antibody conjugates and then imaged under the smartphone FC. Two LinearSVM models provided data numbers for each class. Data classification details are summarized below.

Step 1 (import training data set from file):

A data file with two columns of predictors (RtoBratio and GtoBratio) and one column of categories was imported into the *Classification Learner* app. (See **Figure A. 5**)

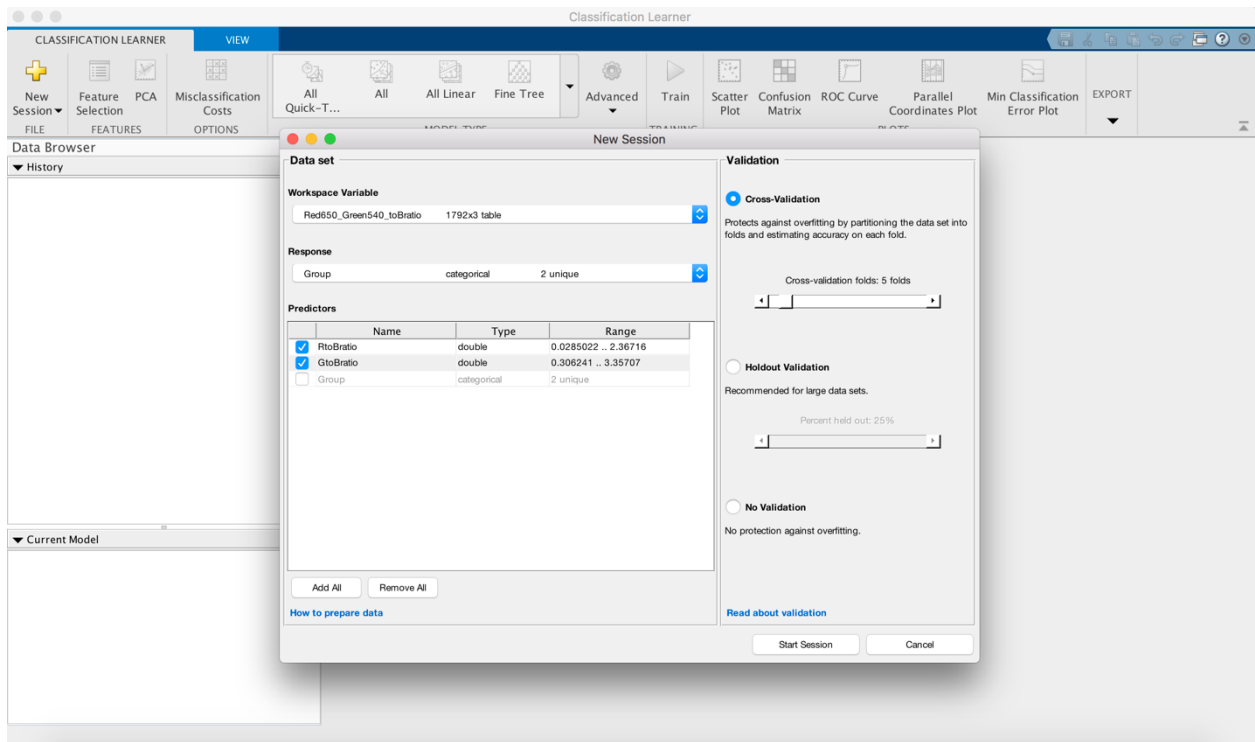
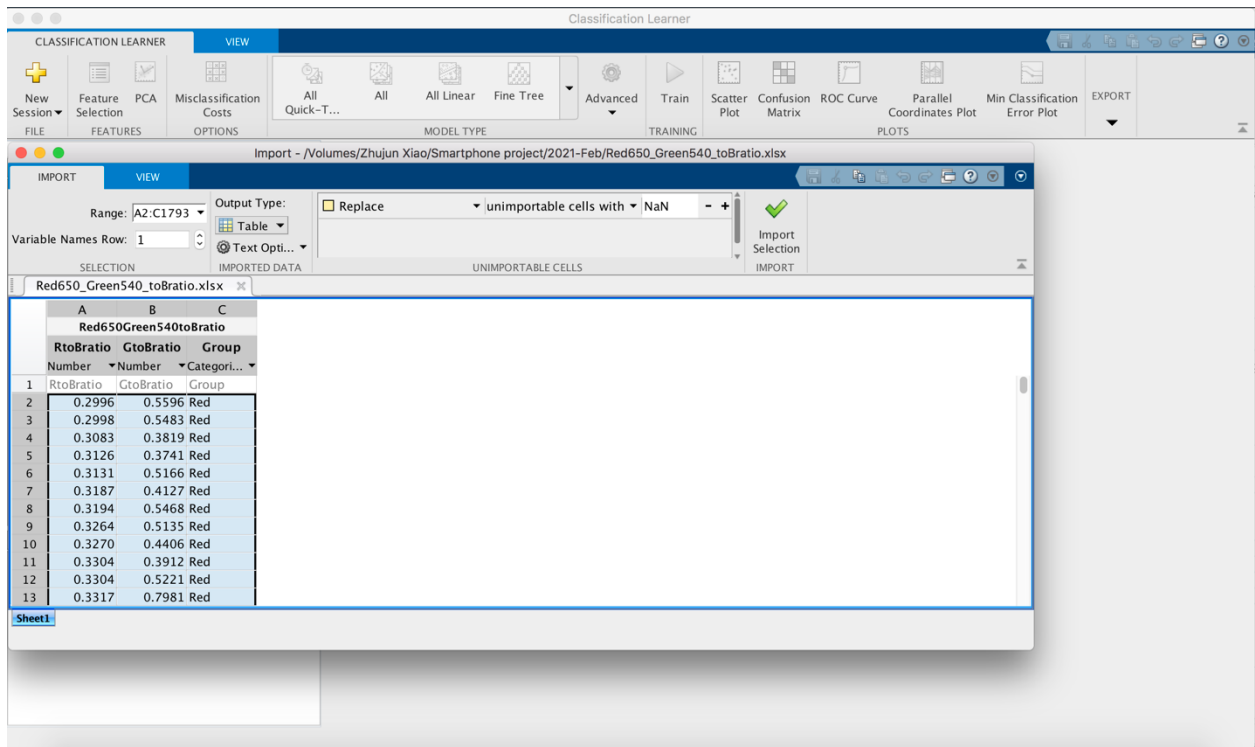


Figure A. 5 MATLAB *Classification Learner* app page. Import desired data (top) by clicking New Session >> From file, select predictors from the dataset imported (bottom) and then start session.

Step 2 (train data sets with SVM model):

MATLAB provides multiple learning models for classification. The models were tested with the training data set and chosen based on a higher accuracy and lower training time. A linear SVM model was selected for the data training in our experiment. Two training datasets were chosen to generate Linear SVM(RG) and Linear SVM(RGN) model. An accuracy of 99.6% was achieved for Linear SVM(RG) model and an accuracy of 99.4% was achieved for Linear SVM(RGN) model. The total training time was ~8.6 s and ~2.3 s, respectively. (See **Figure A. 6**)

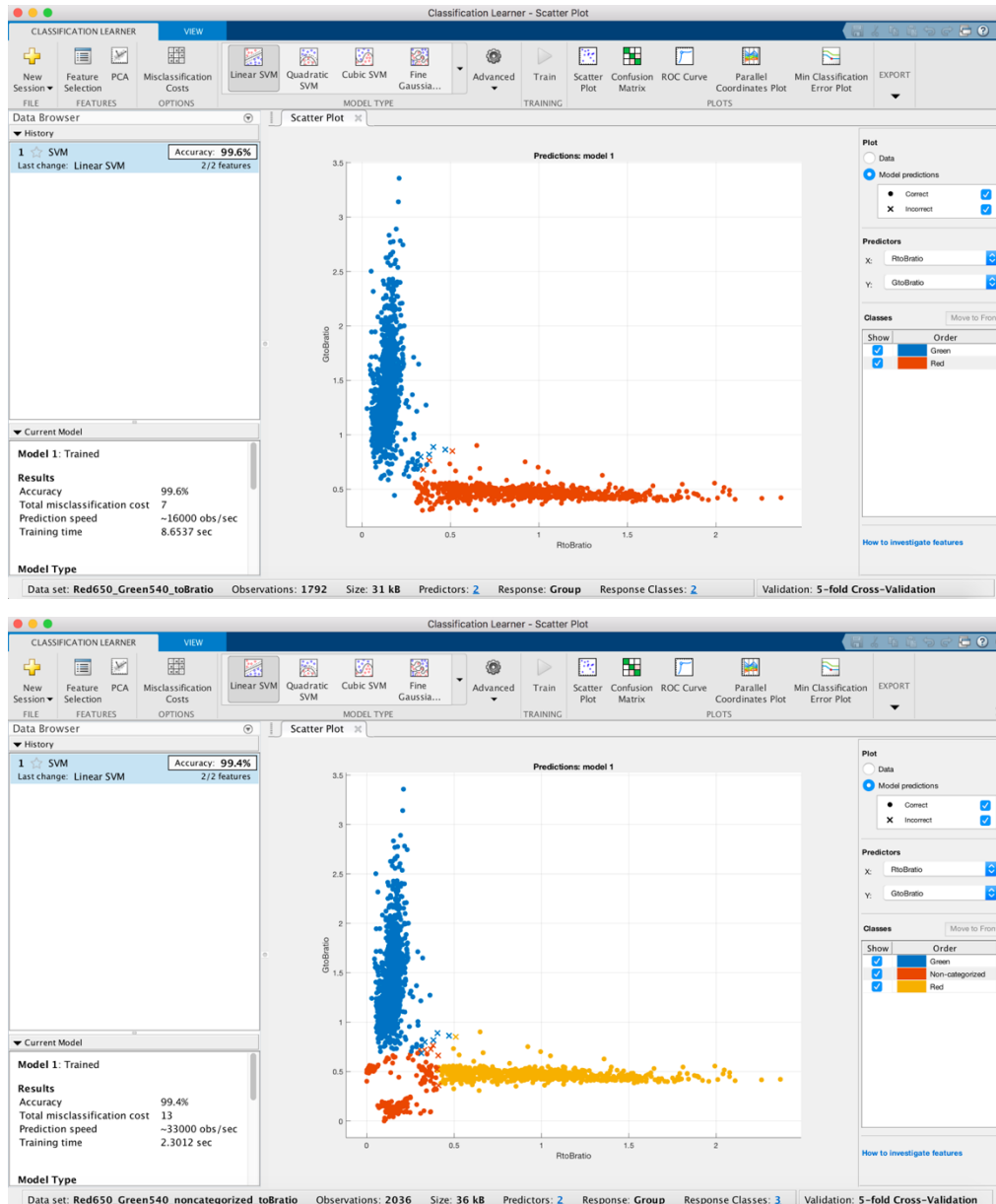


Figure A. 6 Select training model in Model Type Panel and then train the model with dataset (top: LinearSVM(RG) Model, bottom: LinearSVM(RGN) Model). The accuracy and training time of the model were shown in the left.

Step 3 (export model to workspace for test data classification):

The LinearSVM model with two training dataset was exported (Linear SVM(RG) and Linear SVM(RGN) model) and used for classification of test data via the *predict* operation. A scatter plot for the test sample was generated with data points separated into classification groups by the model. (See **Figure A. 7**) The number of data points in each group was obtained with the *hist* operation and number of bin categories was set as number of classified groups.

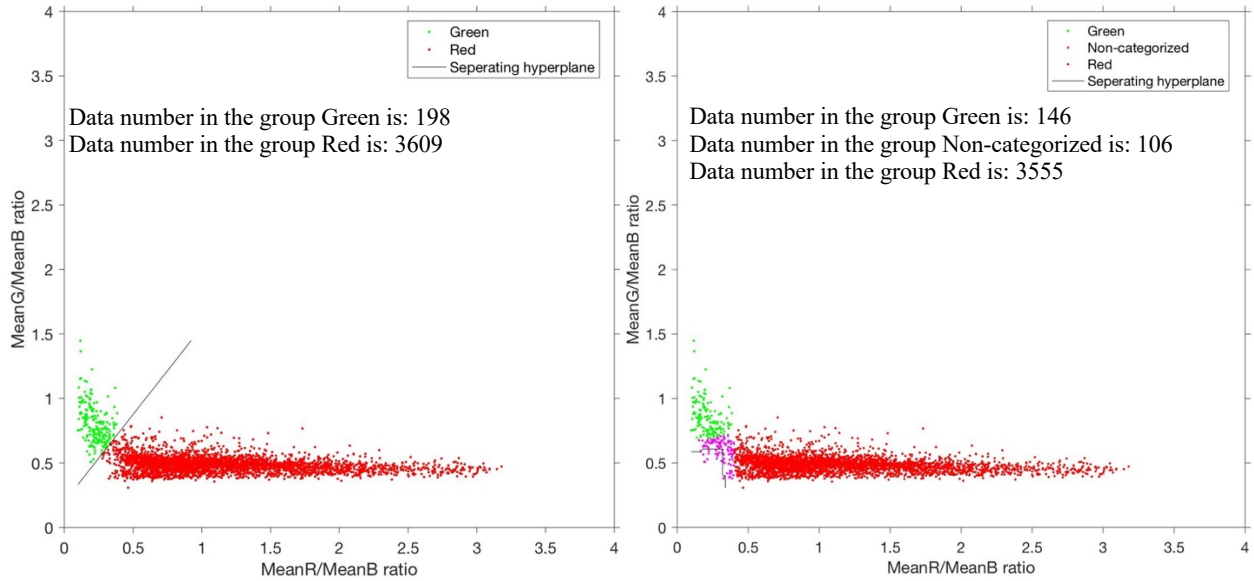


Figure A. 7 MATLAB classification results of a test sample (with low concentration of background SK-BR3 cells, left: using LinearSVM(RG) Model, right: using LinearSVM(RGN) Model)

A.4 MATLAB source code

A.4.1 Cell counting algorithm

Cell counting algorithm was modified from an open-source code (Motion-Based Multiple Object Tracking) on MATLAB.¹⁵⁵

```
Function CellCountingRGB()

close all;

% Create System objects used for reading video, detecting moving
% objects, and displaying the results.

obj = setupSystemObjects();

tracks = initializeTracks(); % Create an empty array of tracks.

nextId = 1; % ID of the next track

% Set videoframes to analysis and saved filepath.
lastframe = input("What's the last frame number?");

[savedfile, path] = uinputfile('*.csv');

if isequal(savedfile,0) || isequal(path,0)
    disp('User clicked Cancel.')
else
    disp(['User selected ',fullfile(path,savedfile),...
        ' and then clicked Save.'])
end

fileID = fopen(savedfile,'a');
fprintf(fileID, 'j, TrackId, Area in Pixels, Mean R, Mean G, Mean
B\n');

% Detect moving objects, and track them across video frames.

for j = 1:lastframe frame_1 = readFrame();
    frame = imcrop (frame_1, [400 0 400 1920]); % Crop ROI for further
    analysis

    Redframe = frame(:,:,1);
    Greenframe = frame(:,:,2);
    Blueframe = frame(:,:,3); % Separate RGB image to three channels
    [centroids, bboxes, mask, meanRGB, areas] =detectObjects(frame);
    predictNewLocationsOfTracks();
```

```

[assignments, unassignedTracks, unassignedDetections] = ...
    detectionToTrackAssignment();

updateAssignedTracks();
updateUnassignedTracks();
deleteLostTracks();
createNewTracks();
displayTrackingResults();

end

```

Create System Objects

Create System objects used for reading the video frames, detecting foreground objects, and displaying results.

```

function obj = setupSystemObjects()
    % Initialize Video I/O
    % Create objects for reading a video from a file, drawing the
    tracked
    % objects in each frame, and playing the video.
    % Create a video file reader.
    file = uigetfile('*.mp4', 'Video files');
    obj.reader = vision.VideoFileReader(file);

    % Create two video player, one to display the video, and one to
    display the foreground mask.
    obj.maskPlayer = vision.VideoPlayer('Position', [0, 800, 400, 800]);
    obj.videoPlayer = vision.VideoPlayer('Position', [400, 800, 400,
    800]);

    % Create System objects for foreground detection and blob
    analysis

    % The foreground detector is used to segment moving objects from the
    background. It outputs a binary mask, where the pixel value of 1
    corresponds to the foreground and the value of 0 corresponds to the
    background.

    obj.detector = vision.ForegroundDetector('NumGaussians', 3, ...
    'NumTrainingFrames', 20, 'LearningRate', 0.003,
    'MinimumBackgroundRatio', 0.75);

    % Connected groups of foreground pixels are likely to correspond to
    moving objects. The blob analysis System object is used to find such
    groups (called 'blobs' or 'connected components'), and compute their
    characteristics, such as area, centroid, and the bounding box.

```

```

obj.blobAnalyser = vision.BlobAnalysis('BoundingBoxOutputPort', true, ...
'AreaOutputPort', true, 'LabelMatrixOutputPort', true,
'CentroidOutputPort', true, ...
'MinimumBlobArea', 30);

```

```
end
```

Initialize Tracks

The `initializeTracks` function creates an array of tracks, where each track is a structure representing a moving object in the video. The purpose of the structure is to maintain the state of a tracked object. The state consists of information used for detection to track assignment, track termination, and display.

The structure contains the following fields:

- `id` : the integer ID of the track
- `bbox` : the current bounding box of the object; used for display
- `kalmanFilter` : a Kalman filter object used for motion-based tracking
- `age` : the number of frames since the track was first detected
- `totalVisibleCount` : the total number of frames in which the track was detected (visible)
- `consecutiveInvisibleCount` : the number of consecutive frames for which the track was not detected (invisible).

Noisy detections tend to result in short-lived tracks. For this reason, the algorithm only displays an object after it was tracked for some number of frames. This happens when `totalVisibleCount` exceeds a specified threshold.

When no detections are associated with a track for several consecutive frames, the algorithm assumes that the object has left the field of view and deletes the track. This happens when `consecutiveInvisibleCount` exceeds a specified threshold. A track may also get deleted as noise if it was tracked for a short time, and marked invisible for most of the frames.

```

function tracks = initializeTracks()
    % create an empty array of tracks
    tracks = struct(...
        'id', {}, ...
        'bbox', {}, ...
        'kalmanFilter', {}, ...
        'age', {}, ...
        'totalVisibleCount', {}, ...
        'consecutiveInvisibleCount', {}, ...
        'meanRGB', {}, ...
        'areas', {});
end

```

Read a Video Frame

Read the next video frame from the video file.

```
function frame = readFrame()
    frame = obj.reader.step();
end
```

Detect Objects

The `detectObjects` function returns the centroids and the bounding boxes of the detected objects. It also returns the binary mask, which has the same size as the input frame. Pixels with a value of 1 correspond to the foreground, and pixels with a value of 0 correspond to the background.

The function performs motion segmentation using the foreground detector. It then performs morphological operations on the resulting binary mask to remove noisy pixels and to fill the holes in the remaining blobs.

```
function [centroids, bboxes, mask, meanRGB, areas] =
detectObjects(frame)

    % Detect foreground.
    mask = obj.detector.step(frame);

    % Apply morphological operations to remove noise and fill in
    holes.

    mask = imopen(mask, strel('disk', 3));
    %mask = imclose(mask, strel('disk', 5));
    mask = imfill(mask, 'holes');

    % Perform blob analysis to find connected components.
    [~, centroids, bboxes, label] = obj.blobAnalyser.step(mask);

    % Get mean RGB value and area in pixels of detected blobs.
    [meanRGB, areas, ~] = MeasureBlobs(label, Redframe,
    Greenframe, Blueframe); % Label each blob so we can make
    measurements of it

end
```

Predict New Locations of Existing Tracks

Use the Kalman filter to predict the centroid of each track in the current frame, and update its bounding box accordingly.

```
function predictNewLocationsOfTracks()
    for i = 1:length(tracks)
        bbox = tracks(i).bbox;

        % Predict the current location of the track.
        predictedCentroid = predict(tracks(i).kalmanFilter);

        % Shift the bounding box so that its center is at the predicted
        location.

        predictedCentroid = int32(predictedCentroid) - bbox(3:4) / 2;
        tracks(i).bbox = [predictedCentroid, bbox(3:4)];

    end
end
```

Assign Detections to Tracks

Assigning object detections in the current frame to existing tracks is done by minimizing cost. The cost is defined as the negative log-likelihood of a detection corresponding to a track. The lower the cost, the more likely that a detection gets assigned to a track. If there is no likelihood of an assignment between a detection and a track, the cost will be infinity.

The algorithm involves two steps:

Step 1: Compute the cost of assigning every detection to each track using the `distance` method of the `vision.KalmanFilter` algorithm, which is designed for object tracking. The cost takes into account the Euclidean distance between the predicted centroid of the track and the centroid of the detection. It also includes the confidence of the prediction, which is maintained by the Kalman filter. The results are stored in an $M \times N$ matrix, where M is the number of tracks, and N is the number of detections.

Step 2: Solve the assignment problem represented by the cost matrix using the `assignDetectionsToTracks` function. The function takes the cost matrix and the cost of not assigning any detections to a track.

The value for the cost of not assigning a detection to a track depends on the range of values returned by the `distance` method of the `vision.KalmanFilter`. This value must be tuned experimentally. Setting it too low increases the likelihood of creating a new track, and may result in track fragmentation. Setting it too high may result in a single track corresponding to a series of separate moving objects.

The `assignDetectionsToTracks` function uses the Munkres' version of the Hungarian algorithm to compute an assignment which minimizes the total cost. It returns an $M \times 2$ matrix containing the corresponding indices of assigned tracks and detections in its two columns. It also returns the indices of tracks and detections that remained unassigned.

```
function [assignments, unassignedTracks, unassignedDetections]= ...
    detectionToTrackAssignment()

    nTracks = length(tracks);
    nDetections = size(centroids, 1);

    % Compute the cost of assigning each detection to each track.
    cost = zeros(nTracks, nDetections);
    for i = 1:nTracks
        cost(i, :) = distance(tracks(i).kalmanFilter, centroids);
    end

    % Solve the assignment problem.
    costOfNonAssignment = 10;
    [assignments, unassignedTracks, unassignedDetections] = ...
        assignDetectionsToTracks(cost, costOfNonAssignment);
end
```

Update Assigned Tracks

The `updateAssignedTracks` function updates each assigned track with the corresponding detection. It calls the `correct` method of `vision.KalmanFilter` to correct the location estimate. Next, it stores the new bounding box, and increases the age of the track and the total visible count by 1. Finally, the function sets the invisible count to 0.

```
function updateAssignedTracks()
    numAssignedTracks = size(assignments, 1);
    for i = 1:numAssignedTracks
        trackIdx = assignments(i, 1);
        detectionIdx = assignments(i, 2);
        centroid = centroids(detectionIdx, :);
        bbox = bboxes(detectionIdx, :);
        RGB = meanRGB(detectionIdx, :);
        area = areas(detectionIdx, :);

        % Correct the estimate of the object's location
        % using the new detection.
        correct(tracks(trackIdx).kalmanFilter, centroid);

        % Replace predicted bounding box with detected
        % bounding box.
        tracks(trackIdx).bbox = bbox;
    end
end
```

```

tracks(trackIdx).meanRGB = RGB;
tracks(trackIdx).areas = area;
% Update track's age.
tracks(trackIdx).age = tracks(trackIdx).age + 1;

% Update visibility.
tracks(trackIdx).totalVisibleCount = ...
tracks(trackIdx).totalVisibleCount + 1;
tracks(trackIdx).consecutiveInvisibleCount = 0;
end
end

```

Update Unassigned Tracks

Mark each unassigned track as invisible, and increase its age by 1.

```

function updateUnassignedTracks()
    for i = 1:length(unassignedTracks)
        ind = unassignedTracks(i);
        tracks(ind).age = tracks(ind).age + 1;
        tracks(ind).consecutiveInvisibleCount = ...
            tracks(ind).consecutiveInvisibleCount + 1;
    end
end

```

Delete Lost Tracks

The `deleteLostTracks` function deletes tracks that have been invisible for too many consecutive frames. It also deletes recently created tracks that have been invisible for too many frames overall.

```

function deleteLostTracks()
    if isempty(tracks)
        return;
    end

    invisibleForTooLong = 8;
    ageThreshold = 5;

    % Compute the fraction of the track's age for which it was visible.
    ages = [tracks(:).age];
    totalVisibleCounts = [tracks(:).totalVisibleCount];
    visibility = totalVisibleCounts ./ ages;

```

```

% Find the indices of 'lost' tracks.
lostInds = (ages < ageThreshold & visibility < 0.6) | ...
    [tracks(:).consecutiveInvisibleCount] >=
invisibleForTooLong;

% Delete lost tracks. tracks = tracks(~lostInds);
end

```

Create New Tracks

Create new tracks from unassigned detections. Assume that any unassigned detection is a start of a new track. In practice, you can use other cues to eliminate noisy detections, such as size, location, or appearance.

```

function createNewTracks()
    centroids = centroids(unassignedDetections, :);
    bboxes = bboxes(unassignedDetections, :);
    meanRGB = meanRGB(unassignedDetections, :);

    for i = 1:size(centroids, 1)

        centroid = centroids(i,:);
        bbox = bboxes(i, :);
        RGB = meanRGB(i,:);
        area = areas(i,:);

        % Create a Kalman filter object.
        kalmanFilter = configureKalmanFilter('ConstantVelocity',
            ...
            centroid, [200, 25], [100, 50], 100);

        % Create a new track.
        newTrack = struct(...
            'id', nextId, ...
            'bbox', bbox, ...
            'kalmanFilter', kalmanFilter, ...
            'age', 1, ...
            'totalVisibleCount', 1, ...
            'consecutiveInvisibleCount', 0, ...
            'meanRGB', RGB, ...
            'areas', area);

        % Add it to the array of tracks.
        tracks(end + 1) = newTrack;

        % Increment the next id.
        nextId = nextId + 1;
    end
end

```

```
end
end
```

Display Tracking Results

The `displayTrackingResults` function draws a bounding box and label ID for each track on the video frame and the foreground mask. It then displays the frame and the mask in their respective video players.

```
function displayTrackingResults()
    % Convert the frame and the mask to uint8 RGB.
    frame = im2uint8(frame);
    mask = uint8(repmat(mask, [1, 1, 3])) .* 255;

    minVisibleCount = 8;
    if ~isempty(tracks)

        % Noisy detections tend to result in short-lived tracks.
        % Only display tracks that have been visible for more than
        % a minimum number of frames.
        reliableTrackInds = ...
            [tracks(:).totalVisibleCount] > minVisibleCount;
        reliableTracks = tracks(reliableTrackInds);

        % Display the objects. If an object has not been detected
        % in this frame, display its predicted bounding box.
        if ~isempty(reliableTracks)
            % Get bounding boxes.
            bboxes = cat(1, reliableTracks.bbox); % Concatenate
            matrices vertically.
            RGB = cat(1, reliableTracks.meanRGB);
            area = cat(1, reliableTracks.areas)

            % Get ids.
            ids = int32([reliableTracks(:).id]);
            numberOfTracks = length(ids);

            % Export MeanRGB of each track
            if numberOfTracks > 0

                fileID = fopen(savedfile, 'a');

                for blobNumber = 1: numberOfTracks
                    fprintf(fileID, '%9d, %9d, %14d, %6.2f, %6.2f, %6.2f
```

```

        \n', j, ids(blobNumber), area(blobNumber), ...
        RGB(blobNumber, 1), RGB(blobNumber, 2),
        RGB(blobNumber, 3));
    end

    fclose(fileID);

end

% Create labels for objects indicating the ones for which
we display the predicted rather than the actual location.
labels = cellstr(int2str(ids'));
predictedTrackInds = ...
[reliableTracks(:).consecutiveInvisibleCount] > 0;
isPredicted = cell(size(labels));
isPredicted(predictedTrackInds) = {' predicted'};
labels = strcat(labels, isPredicted);

% Draw the objects on the frame.
frame = insertObjectAnnotation(frame, 'rectangle', ...
    bboxes, labels);

% Draw the objects on the mask.
mask = insertObjectAnnotation(mask, 'rectangle', ...
    bboxes, labels);
end

end

% Display the mask and the frame.
obj.maskPlayer.step(mask);
obj.videoPlayer.step(frame);
end

```

Get pixel intensity of detected object.

```

function [meanRGB, areas, numberOfBlobs] = MeasureBlobs(label,
Redframe, Greenframe, Blueframe)

[~, numberOfBlobs] = bwlabel(label, 8);    % Label each blob so
we can make measurements of it

% Convert the frame to uint8 RGB, 8-bit unsigned integer arrays
(0-255).
Redframe = im2uint8(Redframe);

```

```

Greenframe = im2uint8(Greenframe);
Blueframe = im2uint8(Blueframe);

% Get all the blob properties. blobMeasurementsR =
regionprops(label, Redframe, 'area', 'Centroid', 'MeanIntensity');
blobMeasurementsG = regionprops(label, Greenframe, 'area', 'Centroid',
'MeanIntensity'); blobMeasurementsB = regionprops(label,
Blueframe, 'area', 'Centroid', 'MeanIntensity');

meanRGB = zeros(numberOfBlobs, 3); % One row for each blob. One
column for each color.
meanRGB(:,1) = [blobMeasurementsR.MeanIntensity]';
meanRGB(:,2) = [blobMeasurementsG.MeanIntensity]';
meanRGB(:,3) = [blobMeasurementsB.MeanIntensity]';

% Now assign the areas.
areas = zeros(numberOfBlobs, 3); % One row for each blob. One
column for each color.
areas(:,1) = [blobMeasurementsR.Area]';
areas(:,2) = [blobMeasurementsG.Area]';
areas(:,3) = [blobMeasurementsB.Area]';

end % from MeasureBlobs()

```

Summary

This algorithm created a motion-based system for detecting and tracking multiple moving objects. The tracking in this example was solely based on motion with the assumption that all objects move in a straight line with constant speed. When the motion of an object significantly deviates from this model, the example may produce tracking errors.

The likelihood of tracking errors can be reduced by using a more complex motion model, such as constant acceleration, or by using multiple Kalman filters for every object. Also, you can incorporate other cues for associating detections over time, such as size, shape, and color.

end

A.4.2 Cell counts after area-based correction

```
% Read data table obtained by CellcountingRGB.m.
opts = detectImportOptions('Filename.csv');
RGBlist = readtable('Filename.csv',opts);

% Sorts rows in ascending order based on the elements in the first
column.
RGBlist = table2array(sortrows(RGBlist));
FrameNumber = RGBlist(:,1);
TrackIdlist = RGBlist(:, 2);
Area = RGBlist(:, 3);
R = RGBlist(:, 4);
G = RGBlist(:, 5);
B = RGBlist(:, 6);

% Return the same data as in TrackIdlist, but with no repetitions.
Then get mean area and RGB value of each track.
TrackId = unique(TrackIdlist);
meanArea = arrayfun(@(a)mean(Area(TrackIdlist ==a)),TrackId);
meanR = arrayfun(@(a)mean(R(TrackIdlist==a)),TrackId);
meanG = arrayfun(@(a)mean(G(TrackIdlist==a)),TrackId);
meanB = arrayfun(@(a)mean(B(TrackIdlist==a)),TrackId);

RtoBratio = meanR ./ meanB;
GtoBratio = meanG ./ meanB;

% Write processed table in a new xls file.
meanRGB = table(TrackId, meanArea, meanR, meanG, meanB, RtoBratio,
GtoBratio);
writetable(meanRGB, 'Filename.xls');

figure;
scatter(RtoBratio, GtoBratio, '.'); % Obtain scatter plot of RtoB ratio
vs GtoBratio

% Set threshold and get rid of any noise, then get the final counts.
RtoBThreshold = 1;
RedAreaThreshold = 102;
GreenAreaThreshold = 102;
BlueAreaThreshold = 102; % Area of single cells
RedAreaRatio = round(meanArea ./ RedAreaThreshold); % Number of cells
in each blob based on area. Round up numbers.
BlueAreaRatio = round(meanArea ./ BlueAreaThreshold);
GreenAreaRatio = round(meanArea ./ GreenAreaThreshold);
RObjects = find(meanR>meanG & RtoBratio>RtoBThreshold & meanR>10 &
```

```
    RedAreaRatio<5); % Exclude any blobs have area bigger than 510
Rcounts = sum(RedAreaRatio(RObjects,1));
GObjects = find (meanG>meanR & meanG>meanB & meanG>10);
Gcounts = sum(GreenAreaRatio(GObjects,1));
BObjects = find(meanB > meanG & RtoBratio<=RtoBThreshold & meanB>10 &
    BlueAreaRatio<5);
Bcounts = sum(BlueAreaRatio(BObjects,1));

totalcounts = Rcounts+Gcounts+Bcounts;

% Get final results

fprintf('Total object counts: %6d\n', totalcounts);
fprintf('Red object counts: %6d\n', Rcounts);
fprintf('Green object counts: %6d\n', Gcounts);
fprintf('Blue object counts: %6d\n', Bcounts);
```

A.4.3 Classification of different cell lines with Linear SVM model

```
% Load Linear SVM model from the folder to workspace
load LinearSVM_mymodel

% Read data table obtained by CellcountingRGB.m.
opts = detectImportOptions('Filename.xls');
testData = readtable ('Filename.xls');

group = LinearSVM_mymodel.predictFcn(testData);

% Get separating hyperplane info and plot classification results

d=0.02;
[x1Grid,x2Grid] =
    meshgrid(min(testData.RtoBratio):d:max(testData.RtoBratio),...
min(testData.GtoBratio):d:max(testData.GtoBratio));xGrid =
[x1Grid(:),x2Grid(:)];
T = array2table(xGrid,...
    'VariableNames',{'RtoBratio','GtoBratio'});
[~,scores] = LinearSVM_mymodel.predictFcn(T);

testData = table2array(testData);
figure;
test = [testData(:,6), testData(:,7)];
gscatter(testData(:,6), testData(:,7),
group, 'gmr','... ',5,'on','meanR/meanB','meanG/meanB')
axis([0 4 0 4]);
xlabel ('MeanR/MeanB ratio', 'FontSize', 16);
ylabel ('MeanG/MeanB ratio', 'FontSize', 16);
ax = gca;
ax.FontSize = 14;
ax.TickDir = 'out';
hold on
contour(x1Grid,x2Grid,reshape(scores(:,2),size(x1Grid)), [0 0],'k');
legend ('Green','Non-categorzied','Red','Seperating hyperplane');
hold off

classification = table(test, group);
[counts,centers] = hist(group, unique(group));
G = string(centers);
A = [G;counts];
fprintf('Data number in the group %s is : %s\n', A);
writetable(classification, 'Filename.xls');
```

Appendix B NTA characterization

NTA was used for size analysis of the $\text{SiO}_2@QD$ self-assemblies of different colours. **Figures B.1-B.5** shows the average sizes (\pm standard deviation) of $\text{SiO}_2@QD$ and $\text{SiO}_2@(QD\text{-Dex})$ or $\text{SiO}_2@(QD\text{-CM-Dex})$. Dextran coatings can increase the colloidal stability of the $\text{SiO}_2@QD$ assemblies,¹⁴³ such that the average size of the $\text{SiO}_2@(QD\text{-Dex})$ and $\text{SiO}_2@(QD\text{-CM-Dex})$ was smaller than the average size of $\text{SiO}_2@QD$.

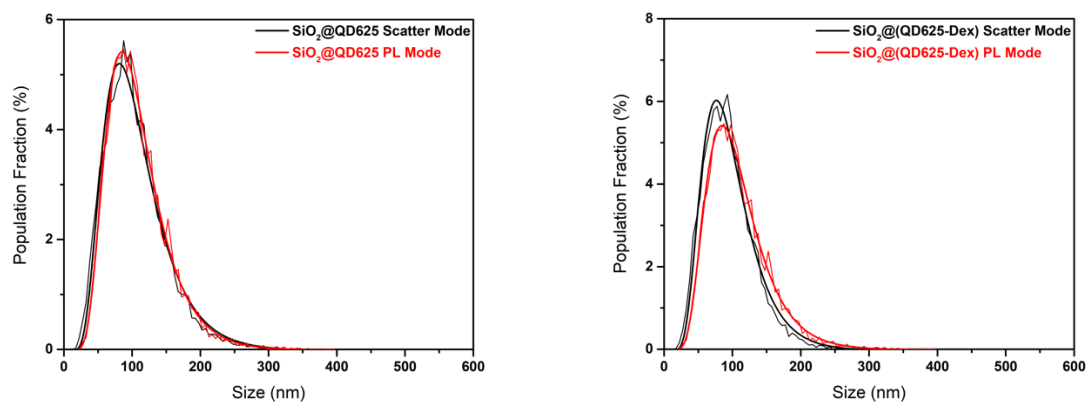


Figure B. 1 $\text{SiO}_2@QD625$ (left, scatter mode: $97 \pm 48\text{nm}$, PL mode: $98 \pm 43\text{nm}$) and $\text{SiO}_2@(QD625\text{-Dex})$ (right, scatter mode: $92 \pm 39\text{nm}$, PL mode: $97 \pm 41 \text{ nm}$) size distributions obtained by NTA.

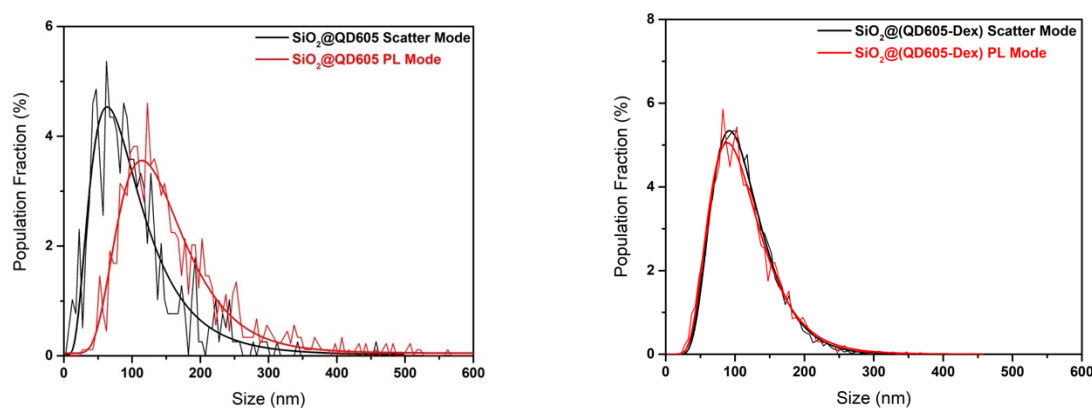


Figure B. 2 $\text{SiO}_2@QD605$ (left, scatter mode: $93 \pm 68\text{nm}$, PL mode: $135 \pm 123\text{nm}$) and $\text{SiO}_2@(QD605\text{-Dex})$ (right, scatter mode: $117 \pm 44\text{nm}$, PL mode: $104 \pm 52\text{nm}$) size distributions obtained by NTA.

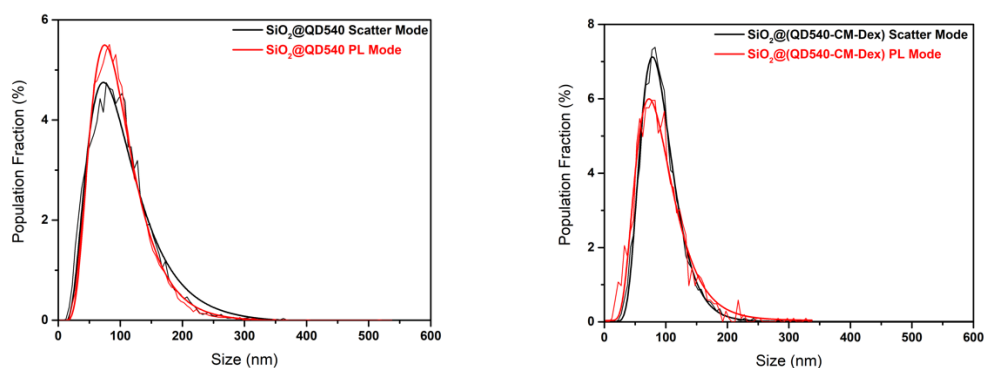


Figure B. 3 SiO₂@QD540 (left, scatter mode: 112 ± 49 nm, PL mode: 92 ± 48 nm) and SiO₂@(QD540-CM-Dex) (right, scatter mode: 83 ± 34 nm, PL mode: 77 ± 30 nm) size distributions obtained by NTA.

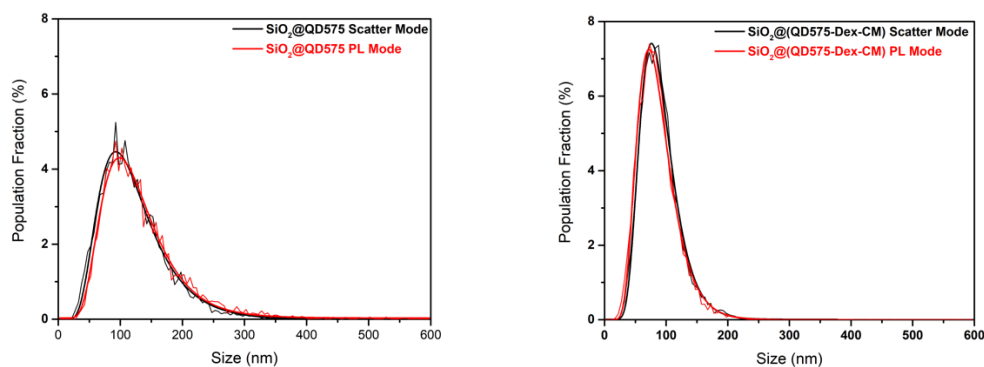


Figure B. 4 SiO₂@QD575 (left, scatter mode: 103 ± 68 nm, PL mode: 113 ± 85 nm) and SiO₂@(QD575-Dex) (right, scatter mode: 85 ± 31 nm, PL mode: 83 ± 35 nm) size distributions obtained by NTA.

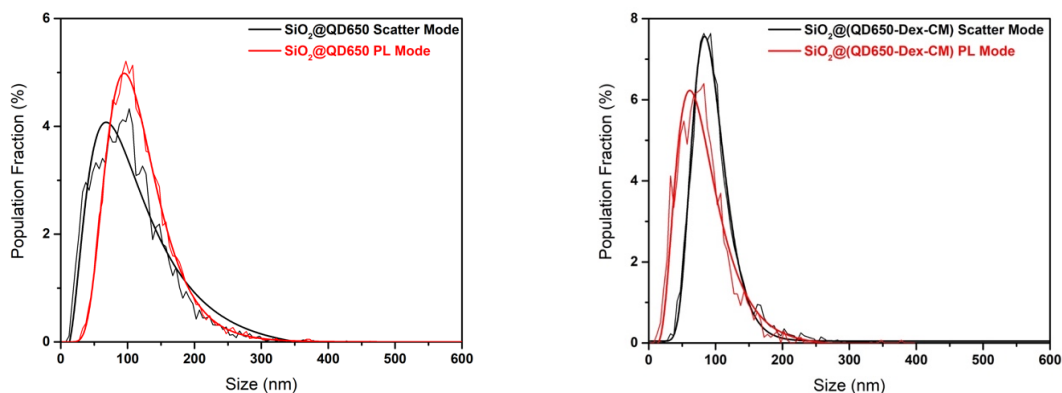


Figure B. 5 SiO₂@QD605 (left, scatter mode: 103 ± 64 nm, PL mode: 122 ± 54 nm) and SiO₂@(QD605-Dex) (right, scatter mode: 88 ± 42 nm, PL mode: 76 ± 41 nm) size distributions obtained by NTA.